University of Alberta

Synthesis and Interfacial Characterization of Metal-Semiconductor Contacts by Galvanic Displacement

by

Sayed Youssef Sayed Nagy

A thesis submitted to the Faculty of Graduate Studies and Research
in partial fulfillment of the requirements for the degree of

Doctor of Philosophy

Department of Chemistry

Spring 2011
Edmonton, Alberta

For Science,

My Mother Naema,

My Wife Noha,

and

my Son Abd-ElRahman

Abstract

Interfacing metals with semiconductor surfaces at the nanometer scale has received much attention, as a result of the critical importance of these interfaces for applications such as integrated circuits, optoelectronics, and others. An efficient and versatile approach for the synthesis of metallic nanostructures on a variety of semiconductor surfaces, including GaAs, InP, silicon [Si(111), Si(100) and Si nanowires], and germanium, is galvanic displacement – a spontaneous electrochemical reaction that is a member of the electroless deposition family. These hybrid nanostructures have intriguing properties but have not been elucidated and therefore not understood. To better illuminate the nature of these systems we use a number of different analyses such as X-ray diffraction (XRD), nanobeam (~5 nm) selected area electron diffraction (SAED), X-ray photoelectron spectroscopy (XPS), and Auger electron spectroscopy (AES), as well as high resolution transmission electron microscopy (TEM) imaging. In spite of the fact the reaction is carried out in water, the growth of gold on silicon and germanium surfaces is heteroepitaxial. This high degree of alignment (heteroepitaxy) was directly observed by high resolution TEM imaging the interface between gold and single crystal germanium and silicon substrates, revealing a coincident site lattice (CSL) of four gold lattices to three of the semiconductor substrate (low lattice mismatch). In the case of Au/Ge, we were able to tune the texture nature of the gold epilayer by changing the composition of the deposition bath.[5]

Galvanic displacement of Au nanoparticles (NPs) on Si nanowires (NWs) showed very interesting phenomenon – Au NPs exhibit preferential deposition on the Si(110) faces of Si nanowires, grown along <112> growth direction, than on the Si(111) faces. The direction of elemental diffusion across the metal-semiconductor contacts was investigated. Spectroscopic (AES) investigations suggest little diffusion of the metals into the semiconductor lattice. Finally, the intermetallic nature of metal-semiconductor interfaces was substantiated by depth profile X-ray photoelectron spectroscopy (XPS) and nanobeam diffraction analyses. Hence, galvanic displacement offers a very attractive method for wiring in nanostructures to semiconductor chips, allowing for its use in modern technological applications.

Acknowledgments

First and foremost, I would like to thank God “ALLAH”, the all knowing, for bestowing me with the grace of science and knowledge. Oh God increase my knowledge.

I would like to express my deepest gratitude for my supervisor Prof. Dr. Jillian M. Buriak from whom I have learned a lot not only what I needed for my PhD studies, but also for my career and my end over. I would like to write Jillian’s rule in my thesis to remember it all over my life. Jillian’s rule: everything has to be done in its best form to achieve the best of the best. I will never forget her discussion, interpretation, encouragement, and suggestions, which provided me with the ideal environment for completing my PhD studies. Finally, thank you very much Jillian.

I would like to thank my committee members who provide me with valuable comments and insightful questions: Prof. Dr. Martin Cowie (Chemistry, University of Alberta), Prof. Dr. Mark T. McDermott (Chemistry, University of Alberta), Prof. Dr. Jonathan G. C. Veinot (Chemistry, University of Alberta), Prof. Dr. Walied Moussa (Mechanical Engineering, University of Alberta), and Prof. Dr. Dan Bizzotto (Chemistry, University of British Columbia).

I was fortunate to work with the Buriak group. I was surrounded by many excellent colleagues who established an excellent friendship and scientific environment helped me to pursue my studies through over five years. Many thanks to my colleagues Jennifer Bruce, Dr. Kenneth Harris, and Dr Usama El-Attar, who revised the grammar of most of my thesis. I would like to acknowledge the support and friendship from the current and past members of the Buriak group: Dr. Sean McClure, Dr. David Rider, and Dr. Steven Chai, Anne Cooper, Dr. Brian Daly (who helped me with the supply of the Si nanowires used in the study shown in chapter 3), Nicole Dehm, Prof. Dr. Anastasia Elias, Yuan Gao, Dr. Yunhui Li, Greg Nilsson, Dr. Yinghong Qiao, Xiao Xing, Dr. Lina Xu, Dr. Dong Wang (the man who I really respect and from whom I have learned a lot), Brian Worfolk, Dr. Vincent Wright, Nathaniel Wu, Dr. Hidenori Mizuno, and Xiaojiang Zhang. I also would like to thank the ACSES center and especially Dr. Dimitre Karpuzov (ACSES), and Mr. Shihong Xu for their helpful discussion for the XPS analyses. I also would to thank Mr. Daniel Salamon (NINT) for his help with surface analysis techniques and teaching me the preparation of cross-sectional samples for TEM analyses shown in chapter 3. Many thanks have to be given to Mr. Jon Giencke from of Bruker AXS for assistance with X-ray diffraction and pole figure measurements.

It is pleasures to thank my entire friends who I have met at the University of Alberta and the Egyptian Student Association. They made my life easier in Canada. I will never forget the wonderful time spent with them.

It is an honor to thank the Cairo University, Egypt, for giving me the opportunity to do my PhD studies at the University of Alberta.

I would like to thank my parents for their sacrifices for educating me, although nothing can satisfy the deserved appreciation. My mother Naema, she did a lot for me, I will never forget her encouragements and guidance. My wife Noha, I really appreciate her encouragement and patience during my PhD studies. To my son, thanks a lot for not playing with your car during my preparation for my PhD defense and your announcement “no noise, my father is studying”. I am looking forward to your defense day.

Table of Contents

List of Figures

List of Tables

List of Abbreviations

IC	Integrated circuits
NEMS	Nanoelectromechanical systems
MEMS	Microelectromechanical systems
HF	Hydrofluoric acid
UHV	Ultra high vacuum chamber
AED	Autocatalytic electroless deposition
SEM	Scanning electron microscopy
XRD	X-ray diffraction
SPR	Surface Plasmon resonance
SERS	Surface enhanced Raman scattering
Sub	Substrate
s	Solid
g	Gas
HF	Hydrofluoric acid
aq	Aqueous
HCl	Hydrochloric acid
H_2SO_4	Sulfuric acid
TEM	Transmission electron microscopy
XPS	X-ray photoelectron spectroscopy
AFM	Atomic force microscopy
SERS	Surface enhanced Raman scattering

NWs	Nanowires
SOI	Silicon-on-insulator
VLS	Vapor liquid solid technique
AAO	Anodic aluminum oxide
ECE	Electroless chemical etching
PEC	Photoelectrochemical
NPs	Nanoparticles
3D	Three dimensional
VW	Volmer Weber growth mode
NHE	Normal hydrogen electrode
CTAB	cetyltrimethylammonium bromide
GD	Galvanic displacement
SAM	Scanning Auger electron microscopy
ET	Electron tomography
FIB	Focus ion beam
χ	Chi
Φ	Phi
θ	Theta
ω	Omega
STM	Scanning tunneling microscopy
CAFM	Conductive atomic force microscopy
PS-*b*-P4VP	Polystyrene-*block*-poly (4-vinylpyridine)
ECE	Electroless chemical etching

Chapter 1

General Introduction

1.1. Introduction and Background

During the last 50 years, the semiconductor industry has shown great progress in the manufacture of high performance products. This progress is largely a result of decreasing the size of synthesized features, allowing for more features per device.[1] Semiconductor technology involves a variety of semiconductors whose properties dictate their applications.[2, 3] Silicon is known for its abundance,[4, 5] low price, low cost of processing,[5] and the highly insulating properties of its oxide. These properties have allowed silicon to be extensively used in IC systems and modern electronics, and to serve as the foundation for the multibillion-dollar electronics industry.[6-10] Looking at the silicon's cousin, germanium, it is also clear that the very high mobility of both electrons and holes, and the low band gap make this material ideally suited for the production of high-speed circuits.[10, 11] Compound semiconductors such as GaAs and InP, also have distinct advantages, such as their direct band gaps, high electron mobility, low turn-on voltages, and high breakdown voltages. [9, 12] As a result, all of these semiconductors have been used in the realization of new commercial markets in areas such as next generation mobile phones, satellite communication, and photovoltaics.[9, 12]

Metal-semiconductor contacts are one of the main components of computer chips and integrated circuits. Moreover, they have been involved in the synthesis of optoelectronic,[13, 14] sensor,[15-21] photovoltaic,[22] biological,[23] and photocatalytic devices.[24] Due to the high demand of metal-semiconductor contacts, these contacts continue to provoke the interests of researchers who have focused on building nanoscale metallic features interfaced directly to materials such as silicon (Si), germanium (Ge), and compound semiconductors such as gallium arsenide (GaAs) and indium phosphide (InP). A great deal of attention has been paid to the control of the metal film surface morphology, structure (texture and crystallinity), interfacial composition, and substrate adhesion, without sacrificing throughput or cost effectiveness. Hence, it is imperative that we realize the importance of proper selection of the method to be used in coating the semiconductor surfaces with metals.

Metallic coating can be produced by physical or wet-chemical procedures.[25-27] Among the conventional physical vacuum-deposition methods are thermal and electron-beam evaporation as well as sputtering techniques.[25] The high capital cost of equipment, lengthy time to achieve the required level of vacuum, equipment maintenance, and wastage of metal are considered the main drawbacks of physical deposition methods. Moreover, in the case of applications that require direct metal-semiconductor contacts with an oxide-free-interface, physical techniques depend upon rapid transferring of clean substrate to an ultra high vacuum (UHV) chamber.

Interfacing semiconductor surfaces with metallic layers by wet-chemical methods involves using either electro- or electroless-deposition pathways, as shown in Scheme 1.1. In the case of electrodeposition, the metal ions are reduced on the semiconductor surface by electrons supplied from an external electrical source.[28]

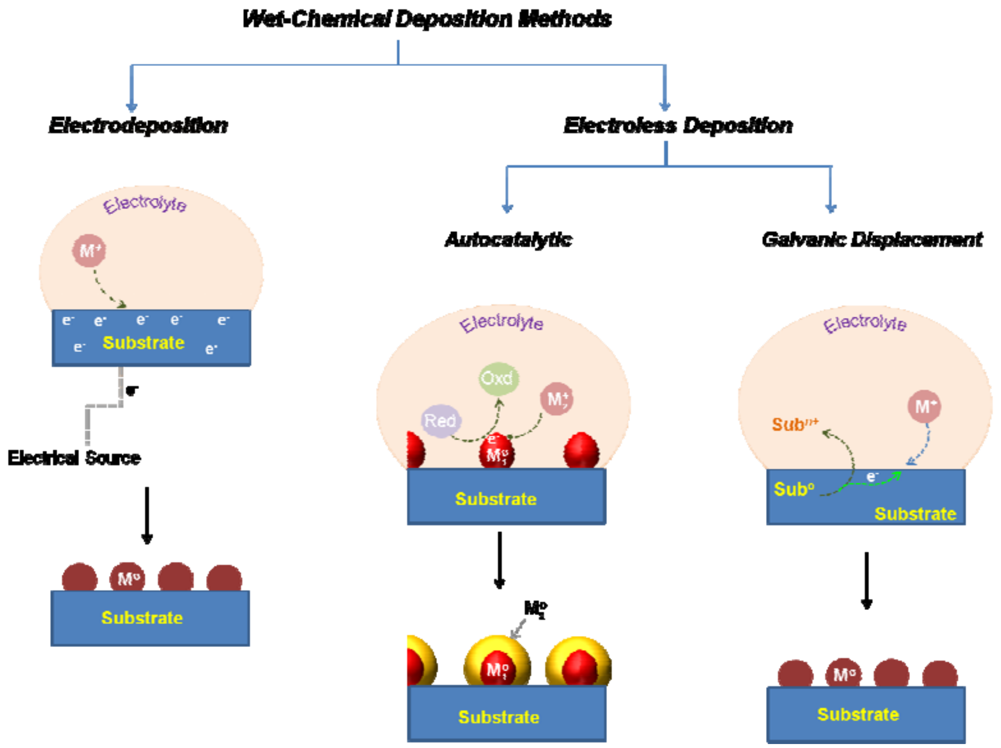

Scheme 1.1. *Metallization of semiconductor surfaces by a wet-chemical deposition mechanism can take place either by electro- or electroless deposition pathways.*[26, 27, 29]

Electroless deposition involves chemical reactions taking place at the substrate surface without using an external electrical supply. The reduction of aqueous metal ions on a substrate surface occurs *via* electrons being supplied from a reducing agent. Depending on the identity of the reducing species, there are two types of deposition mechanisms commonly used for the electroless deposition on semiconductor surfaces: autocatalytic and galvanic displacement.[26, 29] Electroless deposition is applicable to a wide range of metal/substrate combinations including metal-on-metal,[30, 31] metal-on-semiconductor,[26, 27] and metal-on-insulator.[32, 33]

In this chapter, electroless deposition methods and in particular the galvanic displacement process will be discussed in detail. Recent advances in metallization of semiconductor surfaces by the galvanic displacement method and their distinctive applications will be reviewed. Recent reports dedicated to interfacial characterization of metal-semiconductor contacts prepared by galvanic displacement will also be described.

1.2. Autocatalytic Electroless Deposition

In the autocatalytic electroless deposition (AED) method, the reduction of aqueous metal ions on semiconductor surfaces occurs *via* electrons donated from the oxidation of a reducing agent present in solution. Deposition occurs on surface-localized-catalytic sites (metallic nuclei existing on the semiconductor surface) without the involvement of the substrate in charge transfer processes, as shown in Figure 1.1.[26] AED requires an activation step that involves the deposition of noble-metal atoms, such as Pd, over the surface to catalyze the oxidation of a reducing agent on its surface. This process liberates electrons responsible for the subsequent reduction of metal ions.[27] The process is autocatalytic and can result in thick films. It requires, however, a large number or high density of surface-nucleation sites to allow for the formation of continuous films.[26] Examples of chemical reducing agents, include hydrazine, sodium hypophosphite, sodium borohydride, amine boranes, titanium chloride, and formaldehyde.[34] AED can be controlled through judicious choice of the nature of the reducing agent (i.e., the interaction of the metal ions with the oxidized form of the reducing agent), temperature, pH, and concentrations of the reagents.[35]

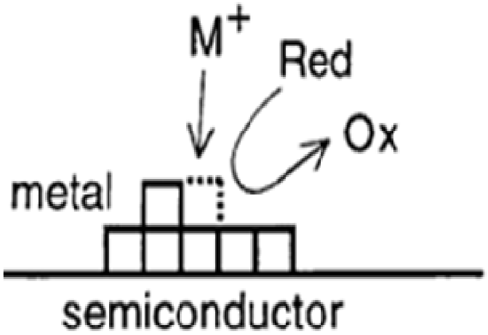

Figure 1.1. *Schematic mechanistic illustration for the metallization of semiconductor surface by an autocatalytic pathway – the reduced metal nuclei act as a catalyst for the reduction of metal ions by the electron supplied from a reducing agent in solution.[26] Copyright © 1998 Institute of Physics (IOP) Science. Reproduced with permission from ref. 26.*

In AED, the substrate does not contribute mechanistically to the charge transfer and deposition processes. As a result, the AED method can be used to construct structures without changing the surface or morphology of the substrate of interest. Yae *et al.* used this advantage to fill Si nanopores with cobalt *via* reduction of aqueous cobalt sulfate with electrons supplied from the oxidation of dimethylamineborane (DMAB), Figure 1.2.[36]

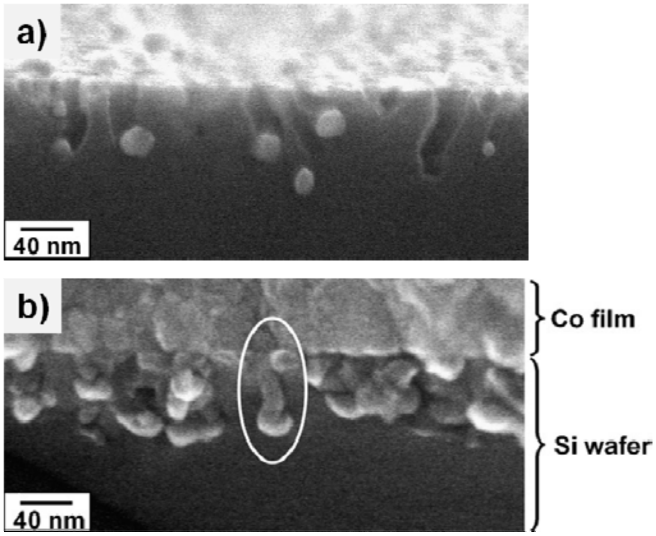

Figure 1.2. *(a) Cross-section scanning electron microscopic (SEM) image (secondary electron) showing Si nanopores formed through Ag-particle-enhanced etching procedures, and (b) Cross-sectional SEM image of Si nanopores filled by metallic cobalt deposited by an autocatalytic electroless deposition method.*[36] *Copyright © 2009 Elsevier. Reproduced with permission from ref. 36.*

One remarkable aspect of the AED method is the effect of surface oxides of the metallic catalytic sites on the structure of the subsequent grown metallic layers. Studies by Li *et al.* addressed the effect of copper oxide layers, formed on electron-beam evaporated copper seeds on Si(111), on the texture of the grown AED copper layer.[37] Rinsing with a solution of (7:3) orthophosphoric:nitric acids followed by dilute sulphuric acid to etch the copper oxide film was essential to induce epitaxial growth of subsequent copper layers via the AED method, as shown in Figure 1.3.[37] In the presence of surface copper oxides, diffraction peaks were observed from Cu planes with (*hkl*) identity other than that of the underlying substrate. For instance, the observation of Cu(111) peak in the XRD plot shown in Figure 1.3a and the Cu(200) peak in Figure 1.3b. Etching the surface oxides, however, resulted in the growth of Cu(100) on Si(100) and Cu(111) on Si(111), as shown in Figures 1.3c and 1.3d, respectively, indicating the epitaxial nature of the grown Cu layer.

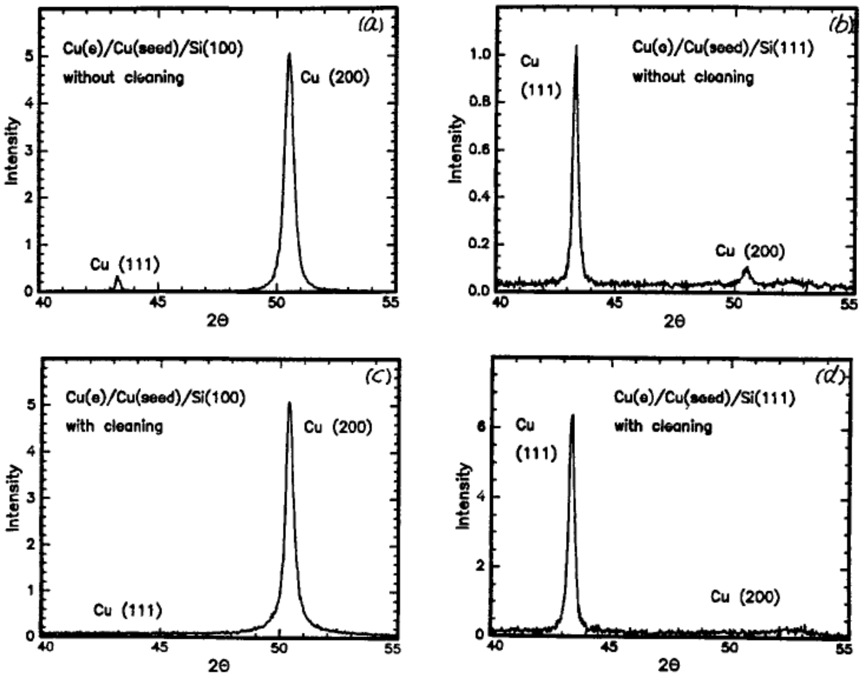

Figure 1.3. *X-ray diffraction patterns for copper layers grown by AED on electron evaporated copper seeds. (a, b), and (c, d) are XRD patterns observed without and with cleaning the seed oxide layer, respectively.*[37] *Copyright © 1992 Electrochemical Society. Reproduced with permission from ref. 37.*

1.3. Galvanic Displacement

An efficient and versatile approach for the synthesis of metallic nanostructures on the surfaces of semiconductor substrates is galvanic displacement (also called displacement plating, immersion plating, or cementation). The reaction is a spontaneous chemical process and is a member of the electroless deposition family.[12, 26, 27, 29, 38-77] Deposition of metals occurs *via* the immersion of a semiconductor substrate in a metal salt solution (Figure 1.4, and scheme 1.1).

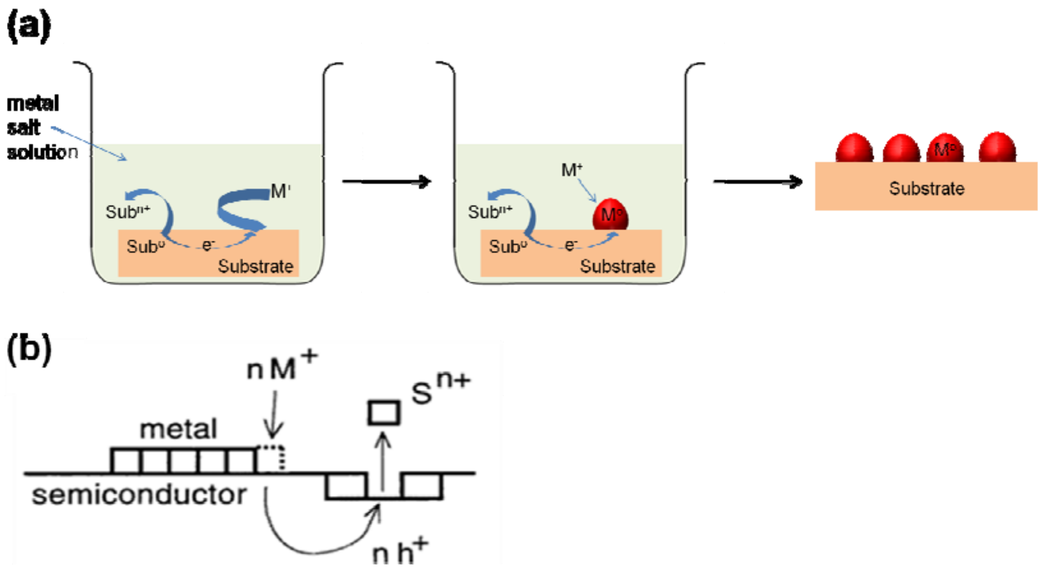

Figure 1.4*. Schematic diagrams, illustrating the metallization of semiconductor surface via the immersion of a substrate in a metal salt solution (a), and the galvanic displacement mechanism (b).*[26] *Copyright © 1998 Institute of Physics (IOP) Science. Reproduced with permission from ref. 26.*

Spontaneous oxidation and reduction reactions take place simultaneously on semiconductor surfaces according to equations (1) and (2):

anodic reaction: $\mathrm{Sub\ (s)} \rightarrow \mathrm{Sub^{n+}\ (aq) + ne^-}$ (1)

cathodic reaction: $\mathrm{M^{n+}\ (aq) + ne^-} \rightarrow \mathrm{M^o\ (s)}$ (2)

where Sub, M, aq, and s indicate the substrate, metal, aqueous, and solid phases, respectively. For these reactions to occur spontaneously, the acceptor states of the metal/metal ion couple (noble metals with positive equilibrium potential, for example) must overlap with the semiconductor valence band (Scheme 1.2).[12, 26, 27, 29] Under this condition, holes can be injected from the metal ion into the semiconductor valence band. In this context, hole consumption takes place *via* the oxidation of semiconductor surfaces liberating bonding electrons derived from the substrate lattice valence band, and resulting in reduction of metal ions and metal deposition. The displacement process occurs in the absence of an external source of electric current or chemical reducing agents (Figure 1.4b).[26, 27] The substrate, which acts as the reducing agent and the source of electrons, reduces the metal ions from the solution. The result is metallic nanoparticles (NPs) and films interfaced with the substrate surface (Figure 1.5).[78] Deposition can continue as long as ions can permit and electrons can transfer through the metallic film.

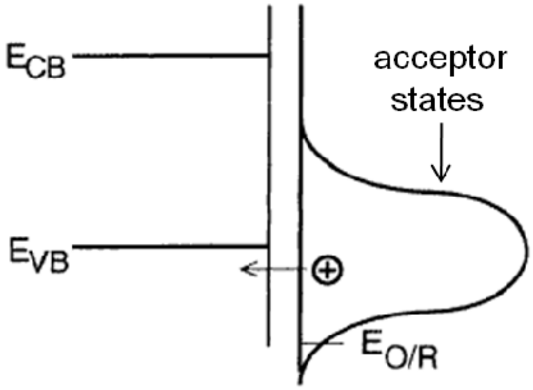

Scheme 1.2. *Energy band diagram illustrating how the injection of holes from metal/metal ion couple of positive equilibrium potential into the semiconductor valence band is feasible.*[26] *Copyright © 1998 Institute of Physics (IOP) Science. Reproduced with permission from ref. 26.*

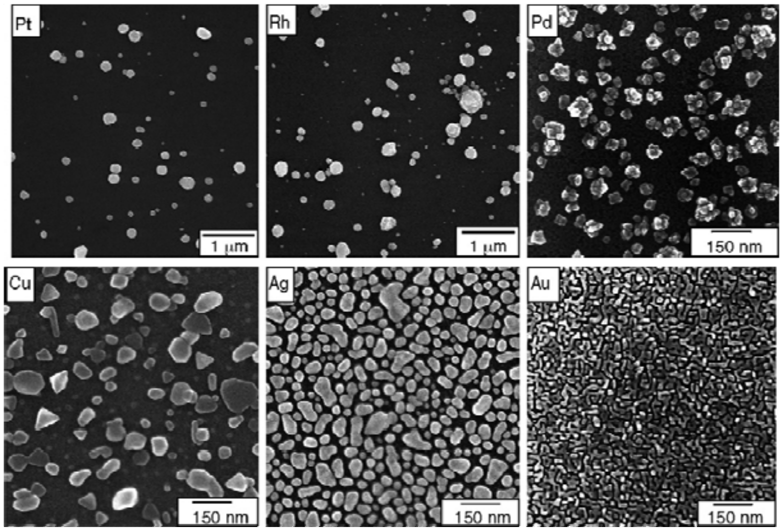

Figure 1.5. *Scanning electron micrographs of different metallic deposits grown on silicon surfaces via galvanic displacement.*[78] *Copyright © 2007 Elsevier. Reproduced with permission from ref. 78.*

Because the reaction is carried out at room temperature with the simplest of chemical apparatus (i.e., water, metal ion, substrate in a beaker), it is straightforward to carry out, less expensive, and faster than commonly used metal evaporation[79] and sputtering techniques.[13, 80] Furthermore, the galvanic displacement process allows control over the size and the shape of metal nanoparticles on semiconductors surfaces, which are considered to be the key for tuning their electrical properties, and for surface plasmon resonance (SPR) and surface enhanced Raman scattering (SERS).[12, 47, 81] One of the drawbacks of galvanic displacement is that the oxidized location can occur near the metallic layer or on any exposed surface, and hence metal-semiconductor contacts may be formed with rough semiconductor interfaces.[12, 69]

1.3.1. Parameters Controlling the Galvanic Displacement Process

There are multiple factors that affect the rate of galvanic displacement. Among these factors are solution composition [the existence of an oxide etching agent such as hydrofluoric acid (HF) and the existence of additives for improved metallic adhesion], metal ions and etching agent concentrations, immersion times, temperatures, pH, and doping of the semiconductor substrate.

Etching Agent

Galvanic displacement involves oxidation of the semiconductor surface, liberating reducing electrons. If the oxidized species is insoluble, a passive layer will be formed, which will inhibit further deposition. For example in the case of silicon, aqueous hydrofluoric acid must be added to the reaction mixture to allow for subsequent dissolution of the oxidized silicon in the form of soluble SiF_6^{2-} species according to equation (3):[57, 69]

anodic reaction: $Si\ (s) + 6F^-\ (aq) \rightarrow SiF_6^{2-}\ (aq) + 4e^-$

$$E^o_{SiF_6^{2-}/Si} = -1.2\ V\ vs.\ NHE \quad (3)$$

In the absence of HF, galvanic displacement can take place on clean hydride-terminated silicon (H-Si). Metallization of silicon surfaces occurs spontaneously. The localized anodic areas, however, are expected to be covered with a silicon oxide layer as a result of the oxidation of silicon surface. Osaka *et al.* used detailed interfacial cross-sectional transmission electron microscopy (TEM) analyses to investigate the effect of HF on the nickel metallization of H-Si, Figure 1.6.[82] Galvanic displacement reactions in the absence of HF in the solution can be represented by equations (4) and (5):[42, 83]

$$Si\ (s) + 2H_2O\ (aq) \rightarrow SiO_2\ (s) + 4H^+\ (aq) + 4e^- \qquad E^o = -0.84\ V_{NHE} \quad (4)$$

$$Ni^{2+}\ (aq) + 2e^- \rightarrow Ni\ (s) \qquad E^o = -0.23\ V_{NHE} \quad (5)$$

Silicon dioxide (SiO_2) is the product of oxidation of the silicon surface in the absence of HF (aq) in the reaction mixture, and was observed in the TEM analyses for the nickel-silicon interface, Figure 1.6. As a result of the formation of this layer, there is no direct contact between the metal layer and the semiconductor surface. This result highlights the importance of an oxide-etching agent in the reaction mixture.

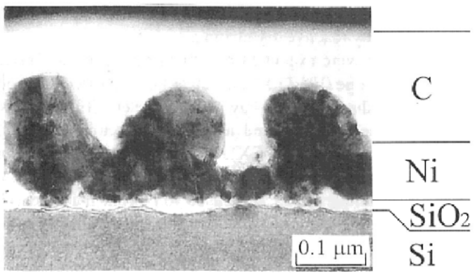

Figure 1.6. *Cross sectional bright filed TEM image of nickel nanostructures grown from an aqueous nickel sulfate solution on a silicon substrate.*[82] *Copyright © 1998 Chemical Society of Japan. Reproduced with permission from ref. 82.*

The effect of HF (aq) concentrations on the rate of metal deposition by galvanic displacement on silicon surfaces has been studied using atomic force microscopy (AFM) analyses.[84] For noble metals such as Au, Cu, and Pd, a direct relationship was observed between the rate of metal deposition and HF concentration, and was explained using equation (3). The supply of reducing electrons is dependent on the fluorine ion concentration and their ability to oxidize the silicon atoms.[84] Recently, Carraro and coworkers explored the effect of HF and copper ion concentrations on the rate of metal deposition (Figure 1.7).[41] At lower HF concentrations (0.05 M), increasing the concentration of copper ions (> 0.01 M) resulted in almost constant deposition rates. The deposition rate, however, increased with HF concentration at a constant concentration of copper ions, indicating that the dissolution of silicon is controlling the deposition process.

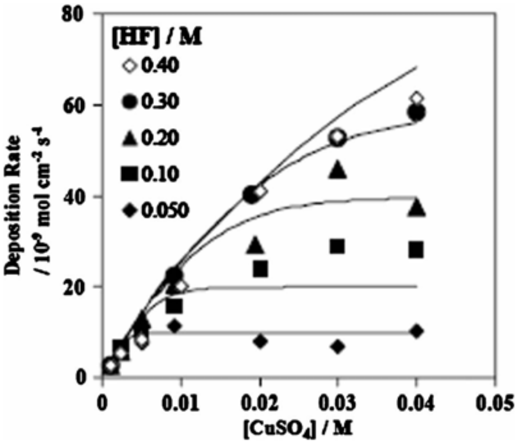

Figure 1.7. *Effect of solution composition on the Cu deposition rate.*[41] *Copyright © 2008 Electrochemical Society. Reproduced with permission from ref. 41.*

Solution Composition and the Identity of Etching Agents

The dependence of metallization of semiconductors surfaces by galvanic displacement on the solution composition and the identity of the etching agent was found to contribute significantly to the deposition of nickel on hydrogen-terminated silicon. X-ray diffraction (XRD) of nickel films prepared on hydrogen-terminated porous silicon from nickel salt solutions containing 5 M aqueous fluoride species (HF, pH 2 or NH_4F, pH 8) (Figure 1.8), were performed by Ogata and coworkers.[85] Consider equations (3), (5) and (6):[85, 86]

$2H^+ (aq) + 2e^- \rightarrow H_2 (g)$ $E_{eq} = -0.48\ V_{NHE}$ (in 5M NH_4F(aq)) (6)

$E_{eq} = -0.12\ V_{NHE}$ (in 5M HF (aq))

where E_{eq} indicates the equilibrium potential. Hydrogen evolution reaction is thermodynamically favored over the nickel reduction in HF solutions.

Consequently, no evidence for crystalline nickel was observed as revealed from X-ray diffraction analyses (Figure 1.8). More nickel deposition occurred in the presence of ammonium fluoride (pH 8) containing solutions, because of the thermodynamically favored nickel deposition.[85] Similar behavior was observed for copper deposition from solutions containing HF or NH_4F.[86] These results highlight the importance of solution composition and pH as well as the identity of the etching agent to the galvanic displacement process.

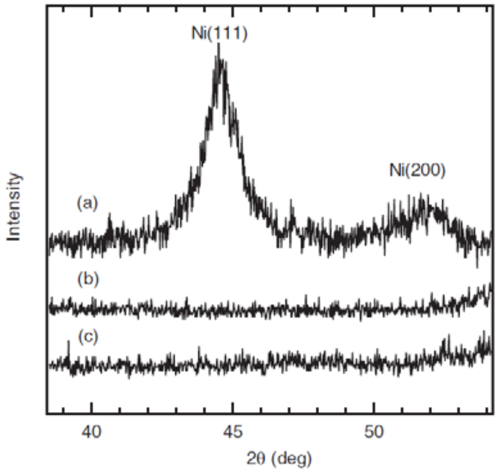

Figure 1.8. *XRD patterns observed from porous silicon after immersion in 50 mM* $NiSO_4$ *solutions containing 5 M* NH_4F *(aq) (pH 8) (a), 5 M HF (pH 2) (b), and a blank porous silicon sample (c).*[85] *Copyright © 2003 Wiley-VCH Verlag GmbH. Reproduced with permission from ref. 85.*

Metal-Semiconductor Adhesion

Galvanic displacement is considered a promising route for interfacing semiconductor surfaces with metallic structures. Unfortunately as a consequence of the simultaneous dissolution and deposition processes, poor metallic film adhesion on semiconductor surfaces has been reported in the literature, without much supporting evidence.[27] The "Scotch tape" test has often been used as a qualitative test of this property.[27] This method lacks reliability and reproducibility as most of the time thicker structures grown from substrate edges fail the test. Nagahara and co-workers demonstrated e method employing contact mode atomic force microscopy (AFM) to investigate the adhesion of palladium (Pd) NPs grown on Si(100), Figure 1.9.[84] The results showed the removal of one of the Pd NPs marked by a black arrow in Figure 1.9. The removal of the Pd NP after successive AFM scans (Figure 1.9b) indicates poor adhesion of the Pd NPs. It is worth noting that when galvanic displacement is used, due to as-yet unknown reasons, the platinum (Pt) group elements including Pt, Rh, and Pd show lower particle density on silicon surfaces, while copper group elements, including Cu, Ag, and Au, show higher particle densities and film formation on silicon surfaces.[78]

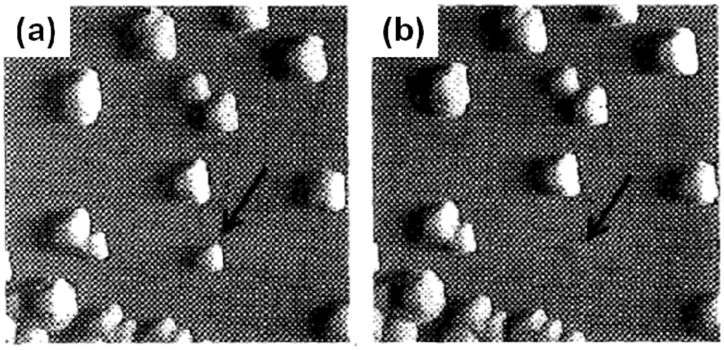

Figure 1.9. *Contact mode AFM images for Pd NPs grown by galvanic displacement on Si(100). Image (b) is observed after several AFM scans of the same area shown in (a).*[84] *Copyright © 1993 American Vacuum Society. Reproduced with permission from ref. 84.*

One explanation for the observed metal dependence of adhesion may lie in the high HF concentration in the reaction mixture. Lombardi *et al*. observed predominant growth of Pt nuclei to form larger clusters rather than further nucleation in the presence of highly concentrated HF in the platinum salt solution.[87] The authors suggest favored dissolution of the exposed silicon area adjacent to NPs, due to the high fluorine content, supplying electrons for the growth of Pt nuclei.[87] Therefore, one can imagine a small contact area between the particles and the underlying substrate or even dissolution of the silicon area surrounding the metallic nuclei, which may explain the weak adhesion of the Pd NPs shown in Figure 1.9.

One of the challenges impeding the application of galvanic displacement in the integrated circuit industry is the poor adhesion of copper on silicon surfaces.[27] However, the most commonly used deposition bath contains copper sulphate and hydrofluoric acid.[88-92] Carraro and coworkers were able to deposit continuous and smooth copper films with highly improved adhesion on different silicon surfaces (p- or n-type single- and polycrystalline silicon) from ammonium fluoride and ascorbic acid ($C_6H_8O_6$) containing solutions (Figure 1.10).[77] The deposition rate was ca. 100 nm/h and the root mean square roughness was in the range of 10-20 nm after 2 hours of plating. Copper films grown in the absence of ascorbic acid failed the “Scotch tape” test. The key idea in this novel method was related to the fact that ascorbic acid prevents hydrogen evolution at the copper-silicon interface as a result of scavenging hydrogen, hence enhancing the film adhesion.[77]

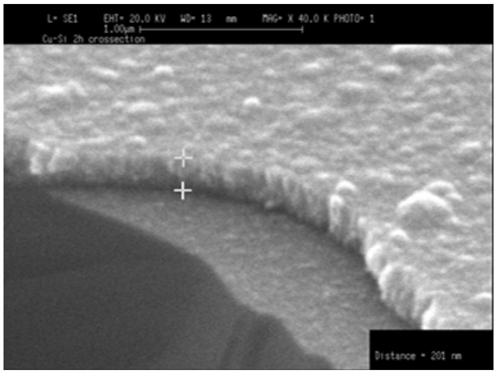

Figure 1.10. *Cross-sectional SEM image of ca. 200 nm copper film on Si(100) after 2 h of plating.*[77] *Copyright © 2001 Electrochemical Society. Reproduced with permission from ref. 77.*

Effect of Immersion Time and Temperature on the Deposition Rate

The application of galvanic displacement in metallization of smaller feature sizes regimes requires controlling the deposition rate, thickness and grain size of the grown metallic structures. These characteristics can be controlled by modulating plating parameters such as temperature, and immersion time. The effect of the immersion time on the grain size and thickness of gold films, grown by galvanic displacement on germanium substrate, was explored by Porter *et al.*[29] Galvanic displacement of gold on germanium was carried out in a gold chloride solution according to equations (7) and (8):[29]

$AuCl_4^-(aq) + 3e^- \rightarrow Au(s) + 4Cl^-(aq)$ $E_{eq} = +1.002\ V_{NHE}$ (7)

$Ge(s) \rightarrow Ge^{4+}(aq) + 4e^-$ $E^o = +0.12\ V_{NHE}$ (8)

The process is thermodynamically favorable. Through detailed AFM analyses, it was found that a smooth gold film comprised of ~ 31 nm grain size is formed after immersion of germanium for 30 s (Figure 1.11a and b). However, immersion for 120 min resulted in thick and rough gold films of ~ 160 nm grain size, due to a prolonged reduction of metal ions and deposition of metal atoms. Moreover, the solution temperature was found to influence the grain size and the deposition rate (Figure 1.11c).[29] For instance, increasing the temperature from 4 to 70 ^{o}C resulted in an increase of the grain size of gold films from 20 to 120 nm and the deposition rate from 1 to 20 nm/min, respectively, after 10 min immersion in 1 mM $AuCl_4^-$ (aq). Therefore, metallic films of varying thicknesses and morphologies can be prepared *via* galvanic displacement through alteration of deposition conditions such as the solution temperature and immersion time.

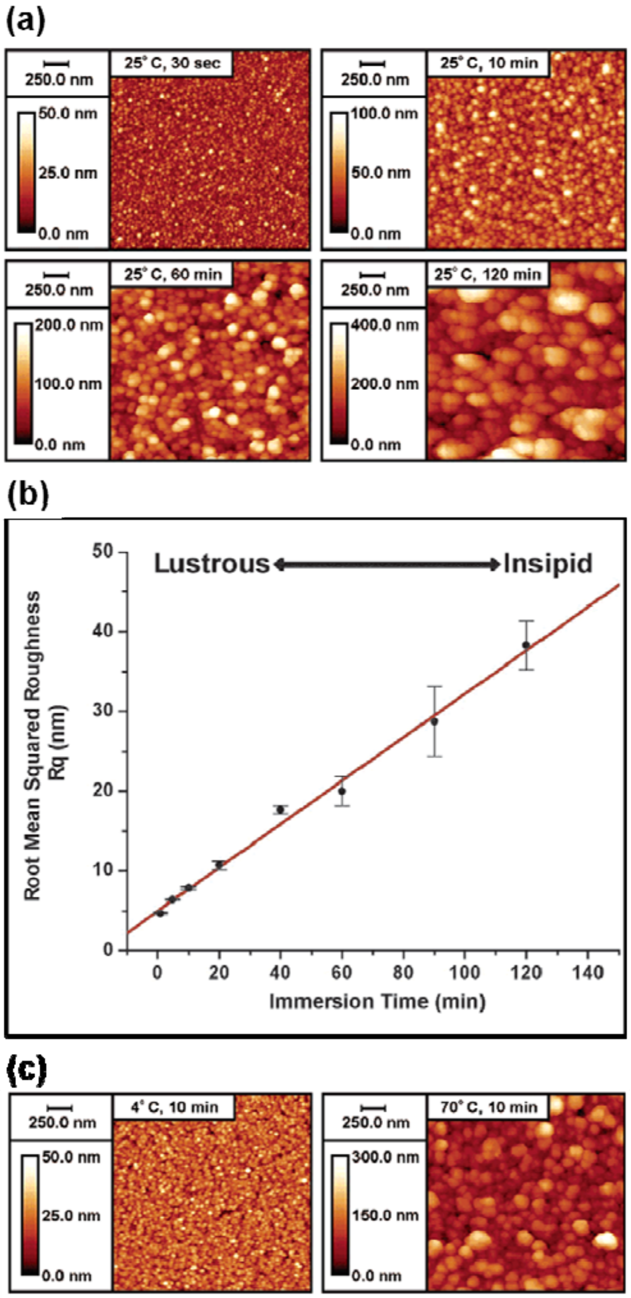

Figure 1.11. *(a) Tapping mode AFM images for gold films grown on Ge(100) for increasing immersion times. (b) The effect of immersion times on the film roughness. (c) Tapping mode AFM images for gold films on Ge(100) grown at different solution temperatures.*[29] *Copyright © 2002 American Chemical Society. Reproduced with permission from ref. 29.*

Effect of Doping Type on the Rate of Deposition

The reduction of metal ions and deposition of metals on semiconductor surfaces by galvanic displacement is dependent mechanistically on the injection of holes by the metal ion in solution to the semiconductor valence band. As a result, oxidation of semiconductor surface atoms takes place to consume the injected holes.[26, 27, 29, 42, 46, 49] Hence, the identity of the semiconductor majority carriers (holes and electrons for p- and n-type, respectively) may play a role in the rate of metal deposition. Sanz and coworkers investigated the difference in the deposition behavior of platinum from HF containing solutions on p- and n-type silicon surfaces (Figure 1.12).[93] The evolution of metallization with the immersion time can be seen from the SEM images (Figure 1.12a-c). By comparing the SEM images in Figure 1.12b (for p-type Si) and Figure 1.12e (for n-type Si), a faster deposition rate of platinum on p-type as compared to n-type silicon can be revealed. For instance, after 30 min of deposition (Figure 1.12b, and e), Pt nuclei spread over the n-type silicon surface, while the p-type silicon is covered with larger clusters. Slower deposition rates on n-type silicon were related to the minor populations of holes which participate mechanistically in the galvanic displacement process.[93]

1.3.2. Applications of Galvanic Displacement in Modern Technology

Galvanic displacement is a chemical method based on chemical reactions occurring on semiconductor surfaces. As a result of its chemical nature, the process shows selectivity to allow patterning of semiconductor surfaces. In this section, we will highlight on the manipulation of the advantages and chemical nature of the galvanic displacement process in sophisticated synthesis which cannot be realized by sputtering and evaporation methods.

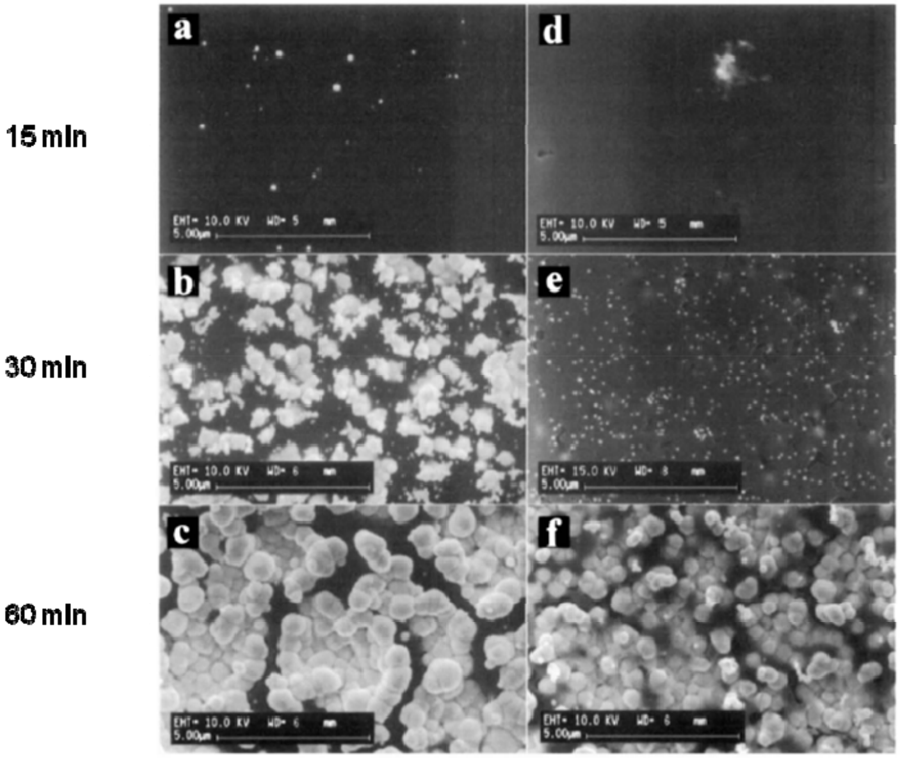

Figure 1.12. *SEM images of Pt nanostructures grown by galvanic displacement on p- (a, b, c) and n- type (d ,e, f) silicon substrates.*[93] *Copyright © 1997 Electrochemical Society. Reproduced with permission from ref. 93.*

Employment of Galvanic Displacement in Integrated Circuits Metallization

The development of faster integrated devices has increased the demand for smaller devices with lower resistivities.[94] Due to the high electromigration resistance of copper and its low resistivity (1.7 μΩ cm) as compared to 2.7 μΩ cm for aluminum, copper has been considered an alternative to aluminum.[94] One of the methods used to deposit copper on semiconductor surfaces is galvanic displacement. The advantage of the method lies in the mechanistic selectivity (for a metal ion-semiconductor system) of exposed semiconductor areas, source of reducing electrons, to the deposition of metals. This advantage has been used by Carraro and coworkers in plating silicon areas on silicon nitride substrates, embedded within microelectromechanical systems (MEMS) (Figure 1.13), with copper. In image (a), the dark areas are the silicon nitride substrate, and the bright areas are the copper plated polysilicon interconnects for an interdigitated comb drive. The selectivity in deposition localization is demonstrated from the placement of the copper signals observed from the polysilicon areas in the SEM/EDX image (b).

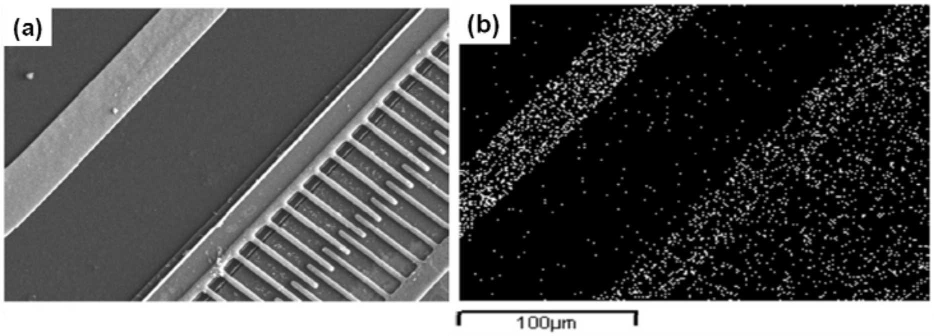

Figure 1.13. *SEM image (a) and SEM/EDX image (b) for copper plated on polysilicon MEMS structures on a silicon nitride substrate.*[77] *Copyright © 2001 Electrochemical Society. Reproduced with permission from ref. 77.*

Preparations of Efficient Surface Enhanced Raman Scattering (SERS) Substrates

The SERS phenomenon, an efficient method for trace molecular detection, arises from the local enhancement of an incident electromagnetic field as a result of surface plasmon excitation of the metallic substrate.[95-99] This local electric field enhancement experienced by surface adsorbed molecules results in high Raman intensity.[95] Since the first reports of the SERS effect,[96-99] there still exists much research directed towards the preparation of SERS active substrates that show both high enhancement factor and reproducibility. During the last decade, SERS substrates made up of adjacent gold or silver nanoparticles have been shown to provide about two orders of magnitude enhancement for analyte detection as compared to detection of the same analyte from isolated NPs.[100-104] These kind of substrates were ascribed as being rich in "hot spots" – areas or regions of a strong electromagnetic field enhancement resulting from metal surface Plasmon excitation localized at the metal surfaces in the gap[105] between the adjacent (nearly touching) particles.[100, 106, 107]

Over the past three years, several reports have come out pointing to the usage of galvanic displacement in the production of gold or silver nanostructures on semiconductor surfaces such as Si,[108, 109] Ge,[110] and GaAs[52] that have been demonstrated to be excellent substrates for SERS applications. Recently, Steinhart and coworkers were able to utilize the galvanic displacement method and block copolymer lithography to synthesize gold-silicon substrates promising for SERS applications (Figure 1.14).[106] Based on the galvanic displacement method, the nanoporous areas of polystyrene-*block*-poly(2-vinylpyridine) (PS-*b*-P2VP) were filled with metallic gold *via* the immersion in a solution of gold salt and HF (aq) for different immersion times as shown in Figure 1.14b. After 30 s immersion in the gold salt solution, mushroom or capped-nanopillar gold-like structures were formed. A high density of capped-gold-structures, slightly touching each other, represents an ideal SERS substrate due to the large number of hot spots. The existence of hot spots, formed on the substrates surfaces after gold deposition for 30 s, caused a high local field enhancement and hence resulted in a high intensity Raman signal and a 1.7 x 10^6 enhancement factor (Figure 1.14c). In a comparison study, 20 nm sputtered gold film resulted in a weak Raman spectra as seen in Figure1.14c. The results highlight the advantages of using and tuning the galvanic displacement process towards the production of an efficient SERS substrate which could not be obtained by sputtering techniques.

Synthesis of Silicon Nanowires via Gold Catalysts Interfaced to Semiconductor Surfaces by Galvanic Displacement

The interesting and exciting properties of semiconductor nanowire arrays, as compared to those of bulk semiconductors, induce more demands on the synthesis of nanowire arrays of controlled size, shape, and length and perhaps of controlled location, enabling their implementation in integrated electronic and electromechanical systems.[40, 111-117] A study was carried out by San Paulo and coworkers for the synthesis of mechanical beam like structures consisting of arrays of microspacers connected to each other by horizontally suspended silicon nanowires (NWs) of controlled size (Figure 1.15).[40] The study was dedicated to the investigation of the elasticity of Si NWs arrays by atomic force microscopy.

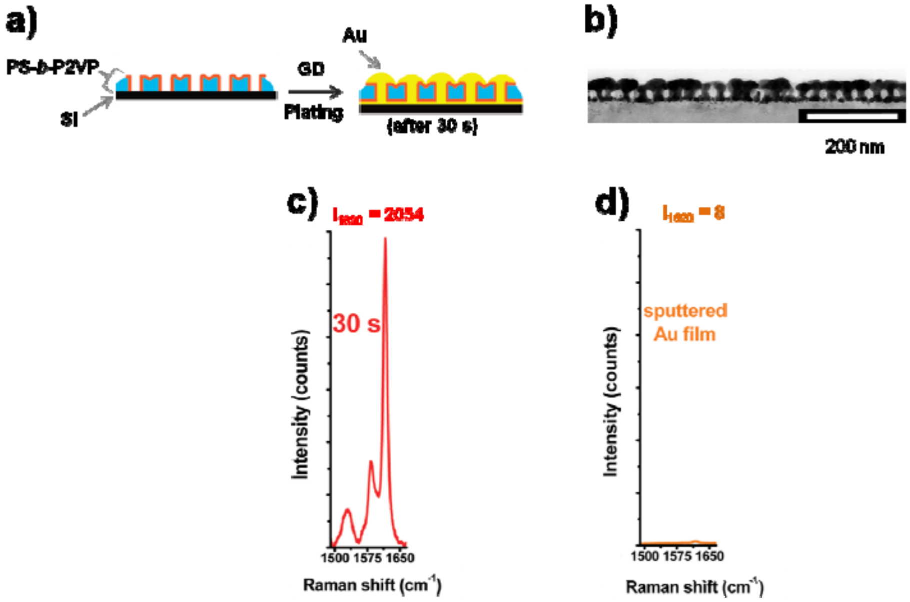

Figure 1.14. *(a) Schematic diagram showing the synthesis of gold-silicon substrates by block copolymer (BCP) lithography and galvanic displacement. Polystyrene (PS): blue, poly (2-vinylpyridine) (P2VP): red, Si: black, and gold: yellow. (b) Cross sectional TEM image for an Au-Si substrate after immersion in 0.02 M* $NaAuCl_4$*/40% HF (aq) for 30 s. Scale bar corresponds to 200 nm. SERS plots of Au-Si substrates, formed by galvanic displacement (c) and by sputtering of 20 nm gold film (d), after exposure to* 10^{-5} *M crystal violet for 10 min.*[106] *Copyright © 2009 American Chemical Society. Reproduced with permission from ref. 106.*

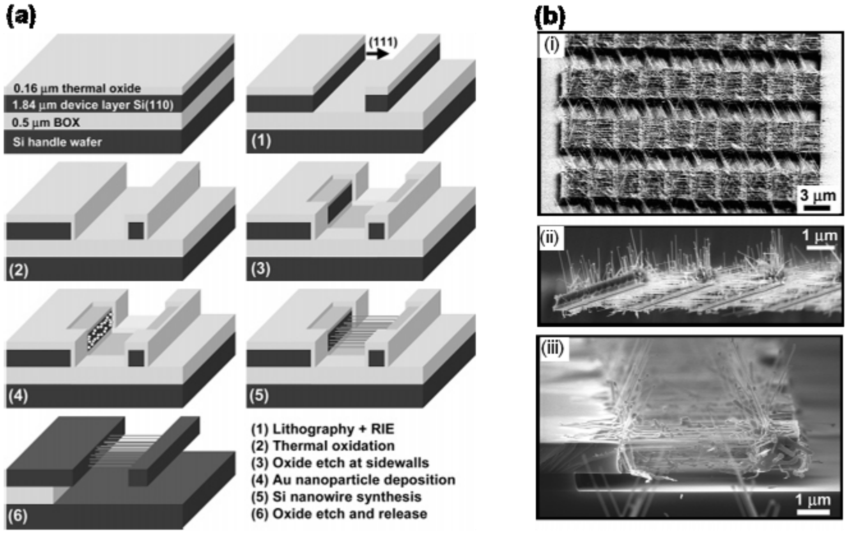

Figure 1.15. *(a) Schematic diagram showing the procedures for the fabrication of horizontally suspended silicon nanowires. (b) SEM images showing the mechanical beam-like structures consisting of multiple arrays of silicon nanowires linked by transversal microspacers.*[40] *Copyright © 2007 American Chemical Society. Reproduced with permission from ref. 40.*

Figure 1.15a shows the synthetic process, involving trench formation with Si(111) side walls *via* optical lithography and reactive ion etching of silicon-on-insulator (SOI) samples. The key point lies in coating the H-terminated trench side walls with gold catalysts for subsequent growth of silicon nanowires by vapor-liquid-solid technique (VLS) – a mechanism involves the growth of one dimensional (D) structures.. The galvanic displacement method involving a gold salt and an aqueous HF solution can result in gold deposition over the entire surface. However, controlled and selective gold deposition on the (111) side walls was achieved *via* substrate immersion in a reversed micelle microemuslion consisting of a water-based plating solution [0.01 M $KAuCl_4$ (aq) + 0.2 M HF (aq)] with n-heptane and a surfactant [sodium bis(2-ethylhexyl) sulfosuccinate (AOT, $C_{20}H_{37}O_7SNa$)].[40]

The advantage of the method is the dependence of the size of the gold catalyst on the radius of the micelle according to equation (9):[27]

$$R_{\text{micelle}} = 0.175R + 1.5 \qquad (9)$$

where R = [water]/[surfactant]. Since the micelle contains the gold salt and HF within its core, galvanic displacement can occur once the micelle core makes contact with the semiconductor substrate. Metallic deposition takes place as a result of oxidizing the semiconductor surface and reducing the gold cations, with controlled cluster size due to the controlled volume of the droplet containing the plating mixture. Hence, gold catalysts of controllable size can be grown on the H-Si(111) side walls of the Si trenches (Figure 1.15a). As shown in the SEM images in Figure 1.15b, horizontally suspended silicon nanowires were grown *via* VLS method. The selectivity towards silicon surfaces for the reduction of gold ions allows selective deposition on the exposed Si(111) side walls and, hence, controls the location of the grown silicon nanowires. On the other hand, evaporating or sputtering gold NPs results in wide-spread coverage of gold particles with no control on the location of the nanowires. Furthermore, the advantage of the chemical nature of the galvanic displacement allows for the involvement or the addition of other chemical steps for achieving the desired objectives and applications as seen in the above example.

The growth of epitaxial silicon nanowires on silicon substrates was reported to show three preferred growth directions: <111>, <112>, and <110>,[118] while the <100> growth direction is only a minor fraction seen only in non epitaxial experiments for growing Si nanowires.[119] Gösele and coworkers studied the growth of Si NWs along the <100> growth direction on Si(100) substrates by growing Si NWs in anodic aluminum oxide (AAO) porous films/Si(100) using the VLS technique.[119-121] The gold catalysts used in the NW growth were prepared by sputtering[119] and by galvanic displacement.[120]

According to detailed TEM investigations, gold NPs, prepared *via* galvanic displacement on silicon surfaces, resulted in the growth of a high quantity of epitaxial Si nanowires with neat and sharp crystallographic interfaces whereas evaporated gold films led to low amounts of epitaxial nanowires, with defects at the silicon nanowire-bulk silicon interface, as shown in Figure 1.16.[119, 120] The sharp nanowire-bulk silicon interface, observed in the case of galvanically displaced gold catalysts, was ascribed to direct gold catalyst-bulk silicon contact as a result of simultaneous etching of the silicon oxide layer during galvanic displacement. In the case of the sputtered gold catalyst, the existence of a thin oxide layer at the gold silicon interface could inhibit or affect the eutectic formation and hence explain the interfacial defects located at the nanowires-bulk silicon interface.[119, 120]

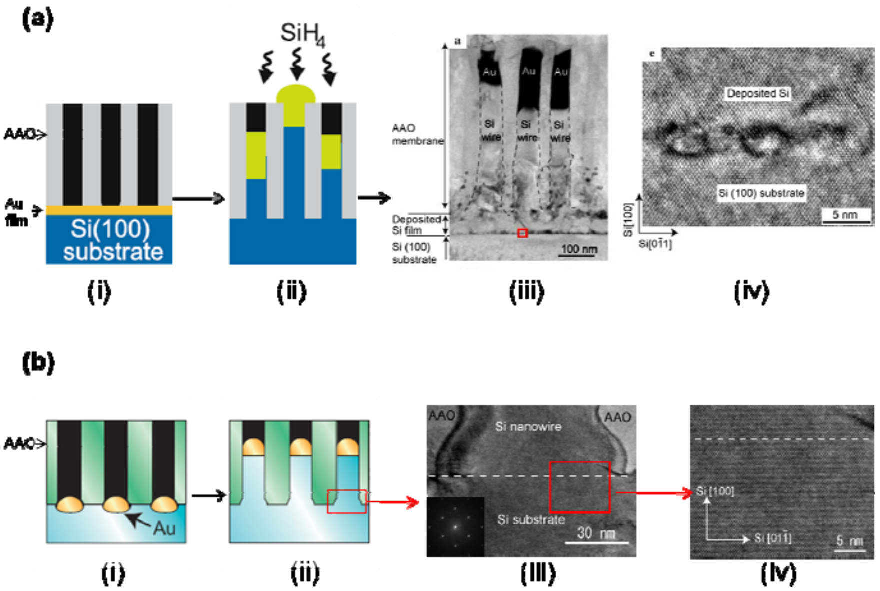

Figure 1.16. *Comparative study for the growth of silicon nanowires using gold catalysts deposited by sputtering (a)*[119] *and by galvanic displacement (b)*[120]*. (i), and (ii) are schematic diagrams showing the synthetic process, while (iii) and (iv) are cross sectional TEM images for a silicon nanowire-bulk silicon interface. Copyright © 2007, Springer Berlin / Heidelberg. Reproduced with permission from ref. 119. Copyright © 2007 Wiley-VCH Verlag GmbH. Reproduced with permission from ref. 120.*

Presently, there is great interest in extending the nanowire 1D structure into a more branched complex one, for electronic circuit applications.[116, 117] Difficulties lie in the fabrication of nanowire structures of reproducible and controllable branch location and structure. Noticeably, the key point lies in controlling the placement of a metal catalyst on the NW, reproducibly, for growing extended branches. Recently, Jacobson used galvanic displacement along with focused ion beam (FIB) for directing the growth of nanowire branches at the desired locations. As shown in Figure 1.17a, FIB was used to draw a rectangular pattern to remove the surface oxide layer and expose the silicon surface for further gold deposition *via* the immersion in a gold salt solution (galvanic displacement), Figure 1.17b. The gold deposit serves as a catalyst for the growth of Si nanowires *via* VLS (Figure 1.17c). For the growth of a nanowire branch, further patterning was performed on the nanowire *via* FIB (Figure 1.17d) followed with gold cluster deposition (Figure 1.17e), allowing for the growth of a branched Si nanowire as shown in Figure 1.17f. These procedures can be repeated as before for the growth of further branched structures as shown in Figure 1.17g and 1.17h. The selectivity of galvanic displacement for the silicon surface played a significant role in the synthesis of a branched nanowire structure of controllable structure. On the other hand, evaporation and sputtering of gold clusters would have resulted in the formation of random branched structures.

- *Top-Down Synthesis of NWs: Electroless Chemical Etching*

One of the challenges encountered upon using bottom-up techniques, such as VLS, is the doping of the fabricated semiconductor nanowires. Controlling the doping level and type over the grown nanowires is very challenging.[122, 123] Moreover, there is a restriction on the orientation of the grown NWs as some orientations are preferred over others.[118] For example, the <111>, <110>, and <112> directions are the only growth directions observed *via* VLS.[124] The growth of <100> Si NWs on Si(100), however, requires a structure directing material such an anodic aluminum oxide membrane.[119, 120] Another challenging point is the metal catalyst required for the NW growth. Metal catalyst atoms can act as defect points,[124] and NWs of random diameter and length are formed.[124]

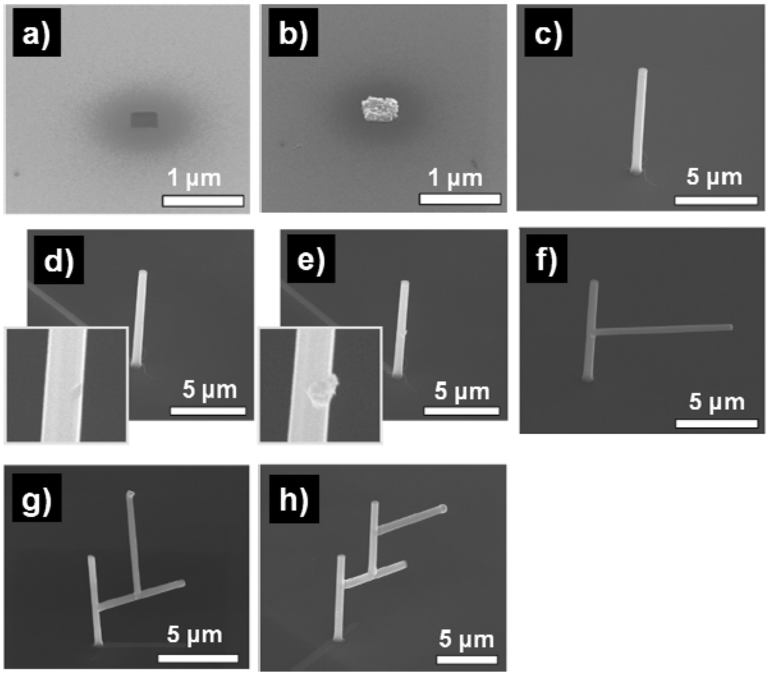

Figure 1.17. *Scanning electron micrographs of (a) a Si substrate with a rectangular pattern drawn by FIB, (b) gold deposits grown by galvanic displacement inside the drawn pattern, (c) a Si NW grown by VLS procedures, (d) a Si NW with a pattern drawn by FIB, (e) gold clusters grown in the NW hole for image d, (f) branched NW grown by the gold catalyst shown in image e, and (g, h) complex branched structures.[117] Copyright © 2010 American Chemical Society. Reproduced with permission from ref. 117.*

Another route for the synthesis of semiconductor nanowires is termed top-down – this method starts with large scale substrates, which can be reduced to nanoscale sizes, *via* additional etching and lithographic procedures.[124-126] Hence, top-down methods can offer a simple solution to problems encountered by bottom-up methods. One can start, for example, with Si(100) substrates to produce <100> Si NWs of close diameters, exact doping level, and controllable length. Electroless chemical etching (ECE), a type of the top-down synthesis pathways, involves the employment of galvanic displacement with wet chemical etching procedures for the synthesis of semiconductor NWs.[125, 126] The method involves the deposition of an electronegative metal such as silver on a silicon substrate by galvanic displacement,[125, 126] followed by immersion of the Ag-Si substrate in an etching solution containing $HF/Fe(NO_3)_3$, as shown in (Figure 1.18). The key point is that once a silver nanoparticle is deposited on the surface, it withdraws electrons from the silicon surface and hence facilitates the silicon oxidation in the form of soluble species. Hence, localized corrosion occurs leading the silver particles to sink into the silicon substrate. In $HF/Fe(NO_3)_3$ (aq) solution, silver particles enhance the oxidation of silicon underneath and act as a surface rich then by electrons, reducing Fe^{3+} to Fe^{2+} ions. Consequently, vertical etching occurs (Figure 1.18b), resulting in highly oriented 1D silicon nanostructure arrays with the required axial crystallographic orientation. Yang and coworkers were able to use the electroless chemical etching method to prepare wafer-scale Si NWs arrays of 20-300 nm in diameter. These NWs are of Seebeck coefficient and electrical resistivity values, which are identical to that of the bulk silicon substrate that is known as a poor thermoelectric material.[127] The prepared NWs, however, exhibit high thermoelectric performance.[127]

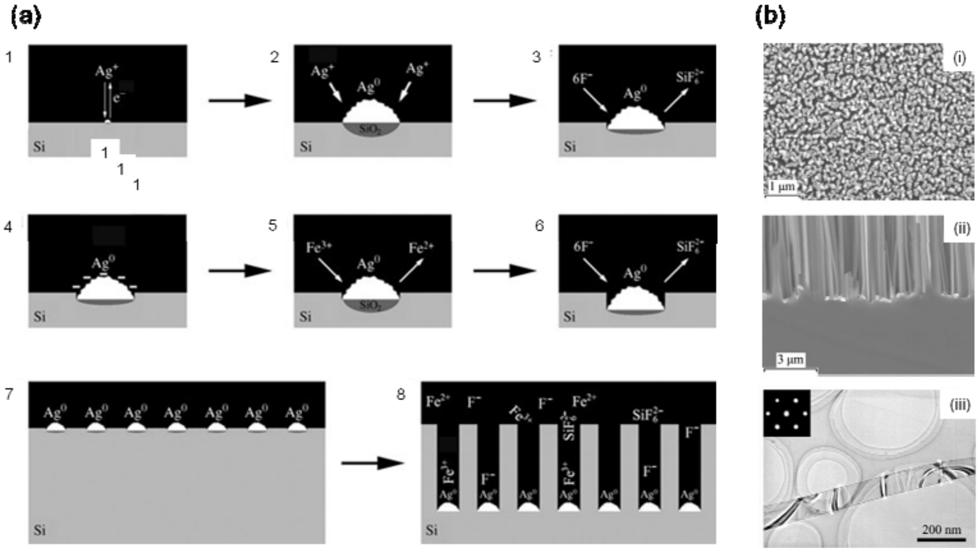

Figure 1.18. *Growth of silicon nanowires using silver catalysts deposited by galvanic displacement on a silicon substrate. (a) Schematic diagram showing the etching mechanism.*[125] *(b) SEM plan view image of the silicon substrate covered with silver particles prior to the etching step (i), cross sectional SEM image for Si NWs formed by chemical etching of bulk silicon substrate, and TEM image for a single crystalline silicon nanoribbon (iii).*[126] *Copyright © 2005 & 2006 Wiley-VCH Verlag GmbH. Reproduced from refs. 125 and 126 with permissions.*

1.3.3. Growth Modes of Metal-Semiconductor Contacts Prepared by Galvanic Displacement

During the initial metallization stages, the semiconductor substrate plays an important role in determining the growth modes of metallic epilayers. This influence arises from a variety of factors, including the chemical interaction between the substrate and the epilayer, the lattice mismatch (i.e., disregistry between the epilayer lattice and that of the underlying substrate), surface roughness, and surface defects.[128] The most commonly encountered growth modes for metal-semiconductor contacts prepared by galvanic displacement are the Stranski-Krastanov (SK) mode,[75, 129, 130] and the Volmer-Weber (VW) mode,[64, 65, 73, 74] see Scheme 1.3.

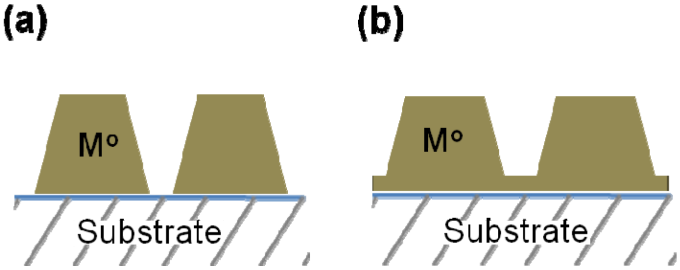

Scheme 1.3. *Schematic diagram illustrating two of the possible heteroepitaxial growth modes of metals on semiconductor substrates. (a) VW growth mode. (b) SK growth mode.*

In the case of SK or layer plus island growth mode, a two dimensional intermediate layer (1-6 monolayers thick) forms and acts as the base for subsequent island growth.[128] In the SK growth mode, island formation relieves the strain induced from the lattice mismatch between the substrate and epilayer.[128] In the VW mode, also known as three dimensional (3D) or island growth mode, small clusters nucleate on the substrate surface followed by their growth into islands. The driving force for this mechanism is the strong interaction or binding between the epilayer atoms than between the epilayer atoms and those of the substrate.[128]

Although the literature is full of postulation about the growth mode of metals on semiconductor surfaces by galvanic displacement, whether it is SK[129, 130] or VW mode,[38, 46] electrochemical evidence was found to substantiate the 3D growth mode.[46] Aizawa *et al.* studied the progress in metallization of germanium surfaces with silver nanostructures through monitoring the open circuit potentials (OCP) as a function of time.[46] Mixed potential theory was used to interpret the open circuit potential values according to equation (10):[50]

$$\Delta E(OPC) = kT/e\Delta j_c/j_a \tag{10}$$

where j_c and j_a are the cathodic and anodic current densities, respectively. As shown in Figure 1.19, the sharp positive potential shift observed after adding silver ions to the solution at 100 s indicates a rapid increase in the cathodic current as a result of the reduction of silver ions and the formation of surface nuclei. The plateau observed after 60 s of silver addition suggests that the deposition process of silver changed from a nucleation to a growth stage. This electrochemical evidence for the 3D growth mode was further substantiated with detailed cross sectional microscopic analyses indicating the 3D or VW growth mode as the initial growth mode.[69]

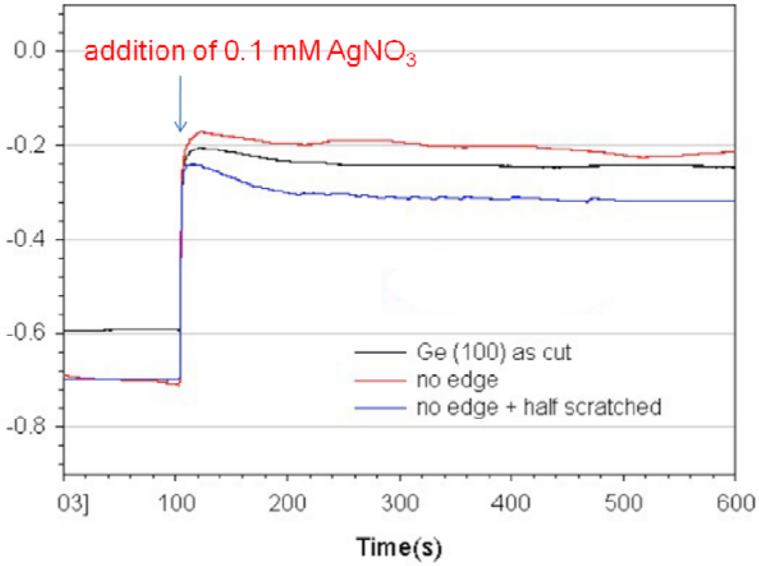

Figure 1.19. *OCP profiles for Ge(100) surfaces as a function of time. 0.1 mM AgNO$_3$ (aq) was added at 100 s. The "no edge" sample means covering all of the edges with epoxy. The "no edge + half scratched" sample means no exposed edges and scratching half of the surface to mimic the high surface area rough edges.*[46] *Copyright © 2005 American Chemical Society. Reproduced with permission from ref. 46.*

1.3.4. Interfacial Metal Silicides and Heteroepitaxy

In many cases, metal silicide formation involves evaporating or sputtering pure metal on silicon surfaces followed by heating up to higher temperatures.[131] Once the device is heated, intermixing can occur.[132-136] The silicide composition was found to be temperature dependant – different phases are formed at different eutectic temperatures, as seen from the phase diagram for chromium-silicon binary system (Figure 1.20).[132] Metal silicides are more conductive (intermetallics) as a result of their narrow band gaps (0.5-0.95 eV), as compared to silicon (1.12 eV band gap).[131, 137] Consequently, Schottky contacts to silicon devices can be fabricated with controlled and defined barrier heights, a great advantage to the device engineer.[131]

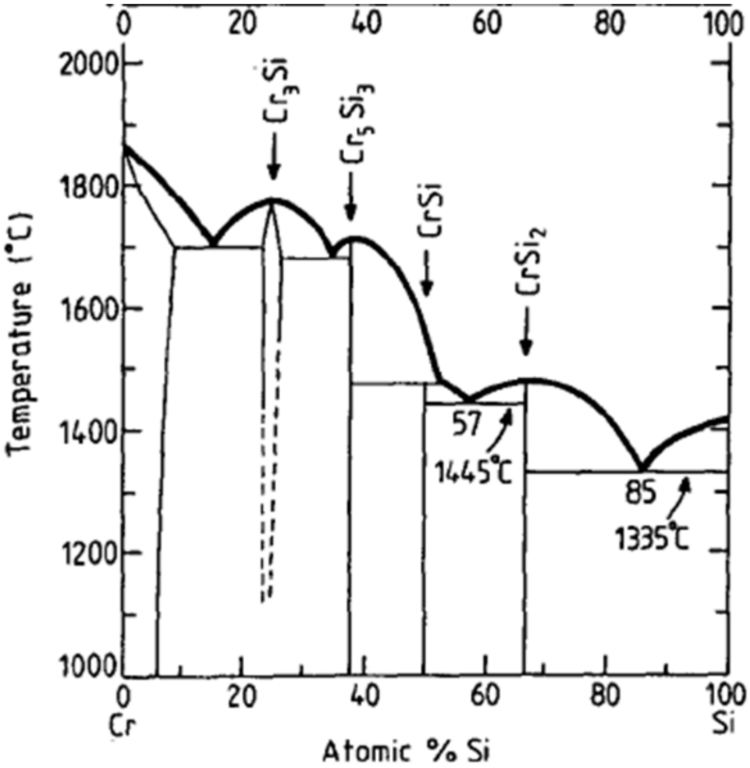

Figure 1.20. *Phase diagram for Cr-Si binary system.*[132] *Copyright © 1990 Elsevier. Reproduced with permission from ref. 132.*

Galvanic displacement is particularly advantageous given its amenity to high throughput processing. In contrast to standard evaporation techniques, galvanic displacement requires only simple apparatus compatible with existing semiconductor processing, and involves low waste generation. The potential for chemical bonding between metallic nanostructures formed *via* this method and technologically important semiconductors such as Ge, GaAs, InP and perhaps Si is particularly attractive for applications such as nanoelectronics and catalysis.[87, 138-140] Recently, Leung and coworkers were able to characterize and analyze the interface between the Si substrate and gold NPs prepared by galvanic displacement on H-Si substrates immersed for 600 s in a solution of 0.05 mM $AuCl_3$ and 0.1 M $NaClO_4$.[39] Interfacial characterization was performed using X-ray photoelectron spectroscopy (XPS) depth profile analyses, as shown in Figure 1.21. This technique gives compositional information along the thickness of the metallic structure through Ar^+ ion etching followed by subsequent XPS compositional analysis for the exposed surface based on the material characteristic binding energy (BE) according to equation (11):

$$\mathrm{BE} = h\nu - \mathrm{KE} - \phi \qquad (11)$$

where BE is the binding energy of the electron in an atom, $h\nu$ is the energy of the X-ray source, KE is the kinetic energy of the emitted electron measured in the XPS spectrometer, and ϕ in the work function (minimum energy required for electron ejection from the highest occupied level to vacuum).[141]

Based on the 0.9 eV shift in Au 4*f* BE (Figure 1.21) towards higher values after longer sputtering times, approaching the Au-Si interface, the authors suggest the existence of gold silicides at the interface.[39] Gold silicides are polar covalent compounds due to the difference (ca. 0.6) in their electronegativity values.[142] With regards to nature of Au-Si bond, the literature is full of postulations about the identity of the overlapping orbital involved in bond formation. Iwami *et al*.[143] and Mönch[144] suggested an interaction between Au *6s* and Si sp^3 electrons. Through detailed XPS studies, Lu *et al.* showed positive shift in the binding energies of both Si 2*p* and Au 4*f* for gold silicides.[145] The observed high BE for Si 2*p* was related to higher electronegativity of gold as compared to silicon (i.e., gold withdraw electrons from silicon). The positive shift of Au 4*f* was interpreted based on the charge compensation model – gold gains an *s* electron from silicon and loses an *d* electron forming *sd* hybrid orbital to bind to Si.[145]

Characterization of gold-silicon samples, prepared by galvanic displacement, based on their crystal structures using glancing angle XRD analyses did not show any evidence for gold-silicides. These observations suggest that gold silicides are amorphous or are present in low quantities to produce an XRD signal.[39]

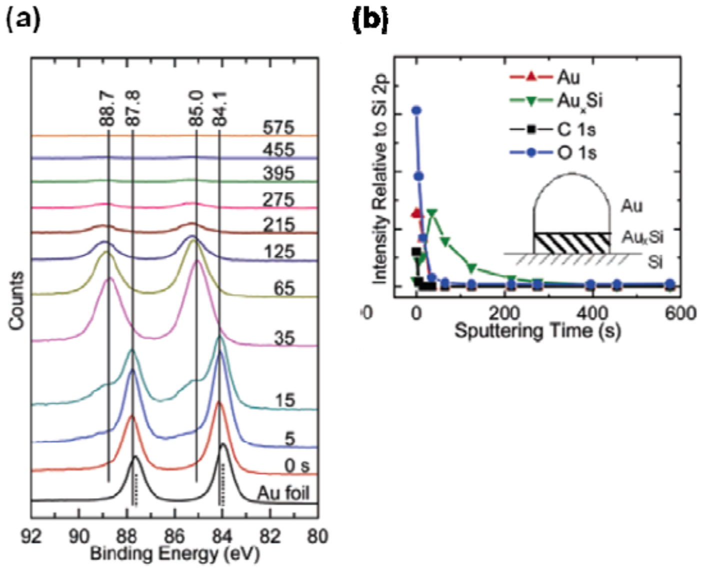

Figure 1.21. *Au 4f XPS depth profile spectra for gold NPs grown on H-Si by galvanic displacement method (a). The XPS peak intensities as functions of the sputtering time (b).*[39] *Copyright © 2007 American Chemical Society. Reproduced with permission from ref. 39.*

In the case of gold-silicon samples prepared by gold evaporation, interfacial gold-silicides have been observed for samples annealed in the temperature range of 100-650 °C.[133-136] Although the phase diagram of Au-Si binary system shows only one eutectic temperature (Figure 1.22),[146] the composition of the gold-silicides (Au_xSi_y) was found to be temperature dependent, i.e., the formation of different silicides at different temperatures.[135, 147] Investigations for as-deposited (room temperature) gold-silicon samples, however, have shown evidence for interfacial gold-silicides with a thickness dependence. In this context, Molodtsov and coworkers have shown, throughout their detailed core-level photoemission analyses for silicon surfaces covered with increasing gold thicknesses, the existence of ca. 0.2 nm critical gold coverage at which metal-semiconductor chemical interactions (formation of silicides) start.[148] Based on their analyses, Au_3Si was found for samples of gold with thicknesses in the range of 0.2 - 2.5 nm above which metallic gold resides on the top of gold-silicide area.[148]

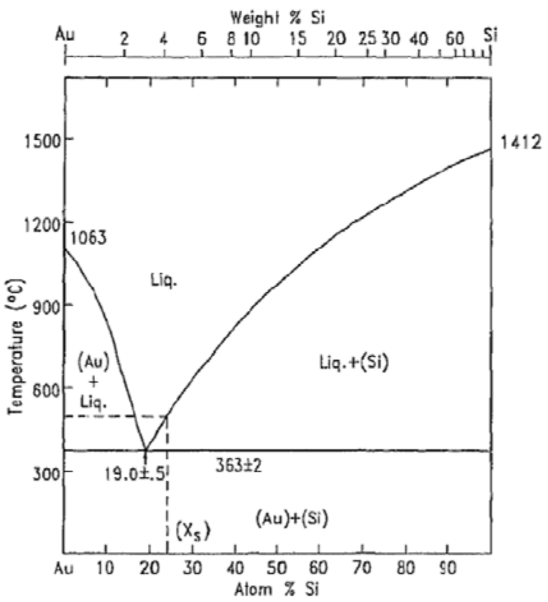

Figure 1.22. *Phase diagram for Au-Si binary system.*[146] *Copyright © 1997 Elsevier. Reproduced with permission from ref. 146.*

The electrical properties of gold-H-terminated silicon interfaces were investigated by Gheber *et al.* using scanning tunneling microscopic (STM) analyses.[149] It was found that covering silicon surfaces with a gold monolayer, ca. 0.2 nm, at room temperature resulted in metallic *I-V* tunneling curves (Figure 1.23). The observed metallic electrical behavior was attributed to the strong bonding between gold and Si surface atoms (formation of silicides).[149] The formed surface compounds (silicides) introduce surface states in the Si band gap, consequently causing the surface to exhibit metallic electrical properties.[149] Similar results were observed for gold monolayers on GaAs.[150] The existence of ca. 3 nm silicon oxide layer at the interface between a gold monolayer and a silicon substrate resulted in a Schottky contact as indicated from the rectifying behavior shown by the *I-V* curves in Figure 1.23b.[149] The rectifying behavior indicates that the interfacial oxide layer prevents the formation of Au-Si bonds (silicides).[149] These reports run contrary to the argument for annealing-dependence of interfacial silicides formation. Moreover, these reports explain the observation of interfacial gold-silicides for gold-silicon samples prepared by galvanic displacement (Figure 1.21).

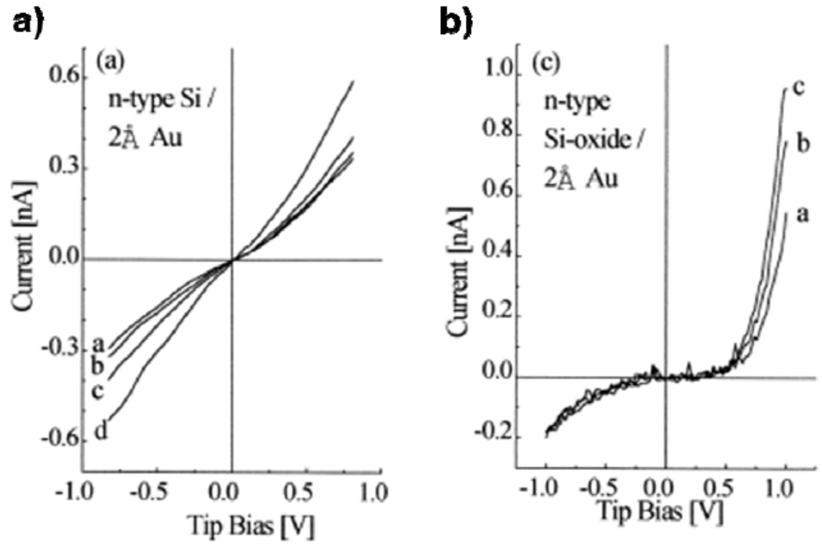

Figure 1.23. *I-V tunneling curves of (ca. 0.2 nm) gold film on n-type H-Si (a) and on n-type oxidized Si (b). The spectra labeled a–d are observed from -15, 0, 10, 25 Å tip displacements (tip-sample distance), respectively.*[149] *Copyright © 1998 Elsevier. Reproduced with permission from ref. 149.*

The Au-Si interfaces, prepared by galvanic displacement, have been studied in great depth but the nature of these interfaces is not well understood. Consequently the nature of these interfaces has become a key research interest.[27] For instance, in the case of gold on silicon, XPS depth profiling clearly indicates evidence for the existence of undefined interfacial gold-silicon intermetallics,[39] whereas surface X-ray diffraction studies point to heteroepitaxial growth of gold on silicon.[73] The relationship or connection between the presence of intermetallics and heteroepitaxy is difficult to envisage.

The epitaxial growth (parallel alignment of the epilayer planes to those of the underlying substrate),[128] of gold on H-terminated silicon prepared by galvanic displacement was related to the high mobility of gold atoms on hydride terminated sites, allowing the occupation of the most favorable sites.[73] Figure 1.24 shows a theoretical model illustrating the adsorption of a gold monolayer on H-terminated silicon surface.[151] In the case of an electrodeposited gold layer on H-terminated silicon, epitaxial growth of gold was related to the desorption of the H-layer and the formation of silicon dangling bonds, resulting in bonding the gold atoms to those of silicon (silicide formation).[152] In chapter 3, we will show evidence for the existence of regions of heteroepitaxial gold-on-silicon, and separate domains containing an intermetallic sandwiched between gold and silicon layers.

Interfacial intermetallic formation has been observed for other systems prepared by galvanic displacement such as platinum-silicon and gold-germanium samples.[42, 153] Based on top-down investigations such as XPS depth profile analyses, the existence of interfacial platinum-silicides was proven.[153] Magagnin *et al*. were able to analyze the gold layers formed at increasing deposition time (from 5 to 600 s) on germanium substrates, and by analyzing the X-ray photoemission spectra of gold valence band region, gold-germanium intermetallic formation was postulated and accounted for the strong adhesion of the gold film to germanium substrates.[42]

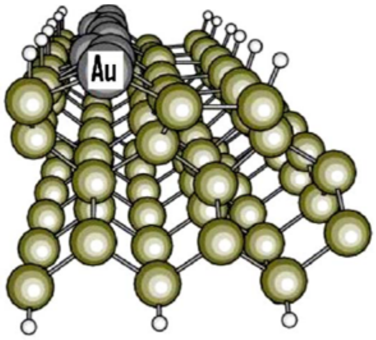

Figure 1.24. *Schematic model illustrating the adsorption of a 4/9 gold monolayer on H-terminated silicon.[151] Copyright © 2009 Elsevier. Reproduced with permission from ref. 151.*

1.4. X-Ray Diffraction (XRD)

X-ray diffraction analyses involve the usage of X-rays of known wavelength (λ) in order to identify the structure of crystalline materials. Crystalline materials are known by the arrangement of their atoms or ions with interplanar spacings (d) specified for each material.[154] As a result, X-ray diffractograms are used as fingerprints for qualitative and structure analyses of materials. When X-rays of wavelength λ hits a sample, the incident rays scatter by the atoms in the system and undergo constructive interference in accordance with Bragg's law:[154]

$$2d\sin\theta = n\lambda \qquad (12)$$

where θ is the angle between incident X-rays and atomic planes and n is an integral. X-ray diffractograms are obtained as a function of the diffraction intensity and 2θ, the angle between the transmitted and diffracted X-rays as seen in Figure 1.25a.[154] X-ray (θ-2θ) diffractograms show Bragg diffractions from only surface planes oriented parallel to the substrate surface, Figure 1.25b.[154]

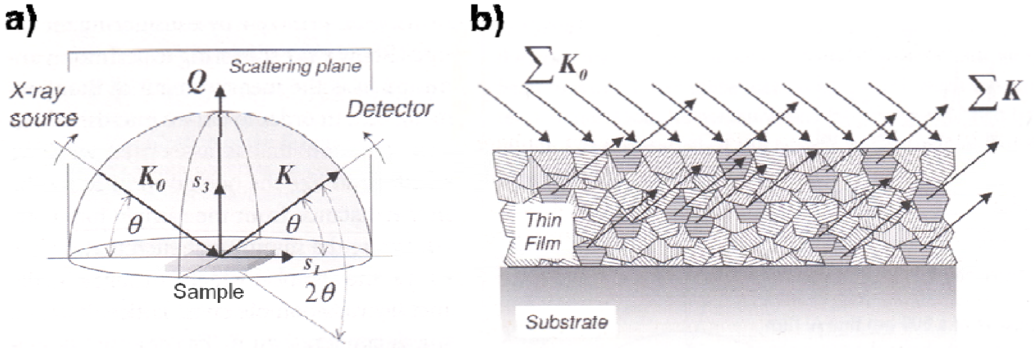

Figure 1.25. *Schematic representation of the X-ray diffraction θ-2θ analysis (a), and the acquisition of Bragg diffractions from surface-parallel planes (b).[154] Copyright © 2006 Wiley-VCH Verlag GmbH. Reproduced with permission from ref. 154.*

Pole Figures

In conventional *θ-2θ* diffractograms, crystal out-of-plane orientations, preferred growth directions, and identity of surface-parallel planes are provided.[154] Crystal grains of seemingly similar out-of-plane orientation may differ in their in-plane orientations.[155] Pole figure analysis investigates the random in-plane orientation of crystalline grains. For instance, fiber texture materials characterized by random in-plane orientation resulted in diffraction ring in pole figures, Figure 1.26a.[156, 157] Single crystal and epitaxial films, however, results in pole figures of clear and sharp diffraction spots, as a result of their uniform orientation along all of the crystallographic axes, see Figure 1.26b.[156, 157]

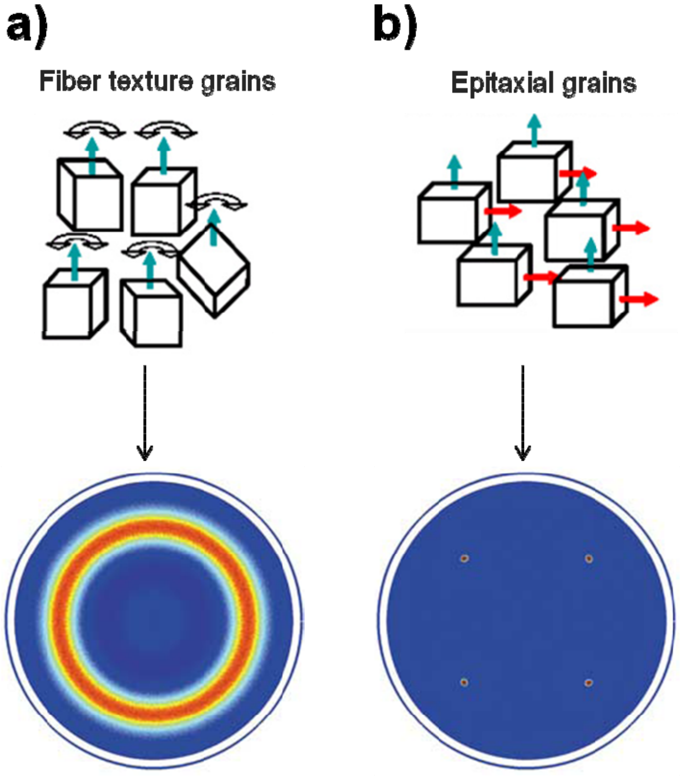

Figure 1.26. *Comparison with standard thin-film pole figures. Example of pole figures for 'standard' fiber texture (a), and epitaxial films (b).*[156, 157] *Copyright © 2003 Nature Publishing Group. Copyright © 2007 Institute of Physics (IOP) Science. Reproduced with permission from refs. 156 and 157.*

1.5. Scope of the Thesis

Metal-semiconductor contacts are integral parts of electronic devices.[143] They have been used as ohmic contacts and Schottky barrier as well as gate electrode.[143, 158] Moreover, interfacial silicides were used to control the barrier height of the synthesized Schottky contacts.[131] In 2009, the International Technology Roadmap for Semiconductor (ITRS) predicted that in 2010, in the 45 nm generation devices, the gate length and thickness of silicide at the contact would be 27 nm and 19.5 nm, respectively.[1] The later values are expected to decrease to 17 nm and 12 nm, respectively, in the 25 nm generation devices in 2015.[1] As a result of increasing the integration level (increasing the number of transistors on a chip, Moore's law), and the tendency for the synthesis of smaller features with time a great attention has to be paid to the interfacial properties of these contacts and the synthesis of defect free interfaces.

This thesis focuses on the synthesis and interfacial characterization of metallic nanostructures interfaced directly on surfaces of technologically important semiconductors such as Si, Ge and compound semiconductors such as GaAs and InP using galvanic displacement. For the employment of galvanic displacement in current metal-semiconductor technological applications, it is critical to understand the growth of the metallic films with regards to the crystallinity of the metallic products (are they amorphous, or poly- and single crystalline?). Other important points that need to be addressed related to the interfacial characteristics of metal semiconductor contacts are the film texture, crystal orientation, interface composition, direction of elemental diffusion across the interface, and conditions controlling the structure of the grown metallic layer. Defining these characteristics for galvanically displaced metallic films is important not only from a fundamental perspective, but also for technological applications based upon current semiconductor technologies. In this work, we describe the use of a number of surface analysis techniques such as X-ray photoelectron spectroscopy (XPS), Auger electron spectroscopy (AES), conductive atomic force microscopy (C-AFM), X-ray diffraction (XRD), transmission electron microscopy (TEM) and nanobeam (probe size < 20 nm) selected area electron diffraction (SAED) to better illuminate the nature of these films and their interfaces.

In chapter 2, we addressed two points: (1) the nature and interfacial composition of metal (gold and silver)-semiconductor (GaAs and InP) contacts prepared by room temperature galvanic displacement process, and (2) the direction of elemental diffusion across metal-semiconductor interface. Investigations involved interfacial characterization using XPS depth profile analyses, which indicated the presence of sandwiched intermetallic layers in the case of gold on GaAs and InP, but little evidence of corresponding intermetallics with silver. Cross-sectional scanning Auger-electron line profile spectra provided evidence for only minor diffusion of metals into the semiconductor lattices. This chapter was reproduced with permission from: Sayed, S. Y.; Daly, B.; Buriak, J. M. *J. Phys. Chem. C.* **2008**, *112,* 12291. Copyright © 2008 American Chemical Society.

In Chapter 3, we focused on the synthesis and interfacial characterization of gold nanostructures on silicon surfaces, including Si(111), Si(100), and Si nanowires. The synthetic approach uses galvanic displacement under aqueous, and room temperature conditions. Through detailed high resolution transmission electron microscopy (TEM), combined with selected area electron diffraction (SAED) and nanobeam diffraction (NBD), heteroepitaxial gold that is grown by galvanic displacement was investigated on both Si(100) and Si(111), as well as silicon nanowires. Moreover, evidence for interfacial silicides and the growth mode of gold on Si will be presented. Finally, we used the precision of TEM to investigate the preferential gold deposition on Si(110) faces of <112> Si NWs. This chapter was reproduced with permission from: Sayed, S.Y., Wang, F., Malac, M., Egerton, R., Meldrum, A., and Buriak, J.M. *ACS Nano* **2009**, 3, 2809. Copyright © 2009 American Chemical Society.

In Chapter 4, we employed galvanic displacement for interfacing germanium surfaces with gold films of tuned texture based on the composition of the deposition solution. In the presence of highly concentrated aqueous HF along with the gold salt solution in the deposition bath, heteroepitaxial gold films were produced as revealed from X-ray in- and out-of-plane studies , and cross sectional TEM diffraction analyses. However, in the absence of HF and the presence of only gold salt solution, fiber textured gold films are produced. The results highlight the importance of HF in the metallization of germanium surfaces by galvanic displacement method. This chapter was reproduced with permission from: Sayed, S. Y.; Buriak, J. M. *ACS Appl. Mater. and Interfaces* **2010**, 2(12) 3515–3524. Copyright © 2010 American Chemical Society.

Finally, Chapter 5 describes the summary of thesis, followed by the potential research direction/perspectives of this thesis work.

1.6. References

(1) In *International Technology Roadmap for Semiconductors, 2009 Edition; Semiconductor Industry Association: San Jose, CA, 2009.*

(2) Sze, S. M.; Ng, K. K. *Physics of Semiconductor Devices*; Jon Wiley & Sons: New Jersey, 2007.

(3) Ventra, M. D.; Evoy, S.; James R. Heflin, J. *Introduction to Nanoscale Science and Technology*; Springer: New York, USA, 2004.

(4) http://en.wikipedia.org/wiki/Silicon.

(5) http://en.wikipedia.org/wiki/Gallium_arsenide.

(6) Bahar, R. I.; Hammerstrom, D.; Harlow, J.; Joyner, W. H.; Lau, C.; Marculescu, D.; Orailoglu, A.; Pedram, M. *Computer* **2007**, *40*, 25.

(7) Allan, A.; Edenfeld, D.; Joyner, W. H.; Kahng, A. B.; Rodgers, M.; Zorian, Y. *Computer* **2002**, *35*, 42-53.

(8) Wolfe, C. M.; Holonyak, J., N. ; Stillman, G. E. *Physical Properties of Semiconductors*; Prentice Hall: Englewood Cliff, NJ, 1989.

(9) Sze, S. M. *Semiconductor Devices, Physics, and Technology*; Wiley: New York, 2002.

(10) Adachi, S. *Handbook on Physical Properties of Semiconductors*; Kluwer Academic: Norwell, 2004.

(11) Chao, Y. L.; Scholz, R.; Reiche, M.; Gosele, U.; Woo, J. C. S. *Japanese Journal of Applied Physics Part 1-Regular Papers Brief Communications & Review Papers* **2006**, *45*, 8565-8570.

(12) Sayed, S. Y.; Daly, B.; Buriak, J. M. *Journal of Physical Chemistry C* **2008**, *112*, 12291-12298.

(13) Ootsuka, T.; Liu, Z. X.; Osamura, M.; Fukuzawa, Y.; Otogawa, N.; Nakayama, Y.; Tanoue, H.; Makita, Y. *Materials Science and Engineering B-Solid State Materials for Advanced Technology* **2005**, *124*, 449-452.

(14) Giziewicz, W. P.; Fonstad, C. G. *Journal of Vacuum Science & Technology A-Vacuum Surfaces and Films* **2002**, *20*, 1052-1056.

(15) Lin, K. W.; Chen, H. I.; Lu, C. T.; Tsai, Y. Y.; Chuang, H. M.; Chen, C. Y.; Liu, W. C. *Semiconductor Science and Technology* **2003**, *18*, 615-619.

(16) Krix, D.; Nunthel, R.; Nienhaus, H. *Journal of Vacuum Science & Technology A* **2007**, *25*, 1156-1160.

(17) Glass, S.; McFarland, E. W.; Nienhaus, H. *Surface Science* **2002**, *518*, 133-140.

(18) Gergen, B.; Nienhaus, H.; Weinberg, W. H.; McFarland, E. W. *Science* **2001**, *294*, 2521-2523.

(19) Gergen, B.; Weyers, S. J.; Nienhaus, H.; Weinberg, W. H.; McFarland, E. W. *Surface Science* **2001**, *488*, 123-132.

(20) Nienhaus, H.; Bergh, H. S.; Gergen, B.; Majumdar, A.; Weinberg, W. H.; McFarland, E. W. *Applied Physics Letters* **1999**, *74*, 4046-4048.

(21) Gutes, A.; Laboriante, I.; Carraro, C.; Maboudian, R. *Sensors and Actuators B-Chemical* **2010**, *147*, 681-686.

(22) Mokari, T.; Rothenberg, E.; Popov, I.; Costi, R.; Banin, U. *Science* **2004**, *304*, 1787-1790.

(23) Liu, L.; Miao, P.; Xu, Y.; Tian, Z.; Zou, Z.; Li, G. *Journal of Photochemistry and Photobiology B: Biology* **2010**, *98*, 207-210.

(24) Elmalem, E.; Saunders, A. E.; Costi, R.; Salant, A.; Banin, U. *Advanced Materials* **2008**, *20*, 4312-4317.

(25) http://www.ece.utep.edu/research/cdte/Fabrication/index.htm.

(26) Oskam, G.; Long, J. G.; Natarajan, A.; Searson, P. C. *Journal of Physics D-Applied Physics* **1998**, *31*, 1927-1949.

(27) Carraro, C.; Maboudian, R.; Magagnin, L. *Surface Science Reports* **2007**, *62*, 499-525.

(28) Liu, R.; Kulp, E. A.; Oba, F.; Bohannan, E. W.; Ernst, F.; Switzer, J. A. *Chemistry of Materials* **2005**, *17*, 725-729.

(29) Porter, L. A.; Choi, H. C.; Ribbe, A. E.; Buriak, J. M. *Nano Letters* **2002**, *2*, 1067-1071.

(30) Padmos, J. D.; Duchesne, P.; Dunbar, M.; Zhang, P. *Journal of Biomedical Materials Research Part A*, *95A*, 146-155.

(31) Steinhauser, E. *Circuit World*, *36*, 4-8.

(32) Li, L. B.; Wang, L.; Wang, H.; Liu, B. *Rare Metal Materials and Engineering*, *39*, 20-23.

(33) Balaraju, J. N.; Kalavati; Rajam, K. S. *Surface & Coatings Technology*, *205*, 575-581.

(34) Mallory, G. O.; Hajdu, J. B. *Electroless Plating: Fundamentals and Applications*; William Andrew Publishing/Noyes Orlando, FL, 1990.

(35) Okinaka, Y.; Osaka, T. *Advances in Electrochemical Science and Engineering* **1994**, *3*, 55-116.

(36) Yae, S.; Hirano, T.; Matsuda, T.; Fukumuro, N.; Matsuda, H. *Applied Surface Science* **2009**, *255*, 4670-4672.

(37) Li, J.; Shachamdiamand, Y. *Journal of the Electrochemical Society* **1992**, *139*, L37-L39.

(38) Brenner, A.; Riddell, G. E. *Journal of Research of the National Bureau of Standards* **1946**, *37*, 31-34.

(39) Zhao, L. Y.; Siu, A. C. L.; Petrus, J. A.; He, Z. H.; Leung, K. T. *Journal of the American Chemical Society* **2007**, *129*, 5730-5734.

(40) San Paulo, A.; Arellano, N.; Plaza, J. A.; He, R. R.; Carraro, C.; Maboudian, R.; Howe, R. T.; Bokor, J.; Yang, P. D. *Nano Letters* **2007**, *7*, 1100-1104.

(41) daRosa, C. P.; Maboudian, R.; Iglesia, E. *Journal of the Electrochemical Society* **2008**, *155*, E70-E78.

(42) Magagnin, L.; Maboudian, R.; Carraro, C. *Journal of Physical Chemistry B* **2002**, *106*, 401-407.

(43) Aizawa, M.; Buriak, J. M. *Chemistry of Materials* **2007**, *19*, 5090-5101.

(44) Aizawa, M.; Buriak, J. M. *Journal of the American Chemical Society* **2006**, *128*, 5877-5886.

(45) Aizawa, M.; Buriak, J. M. *Journal of the American Chemical Society* **2005**, *127*, 8932-8933.

(46) Aizawa, M.; Cooper, A. M.; Malac, M.; Buriak, J. M. *Nano Letters* **2005**, *5*, 815-819.

(47) Nezhad, M. R. H.; Aizawa, M.; Porter, L. A.; Ribbe, A. E.; Buriak, J. M. *Small* **2005**, *1*, 1076-1081.

(48) Porter Jr, L. A.; Ribbe, A. E.; Buriak, J. M. *Nano Letters* **2003**, *3*, 1043-1047.

(49) Porter, L. A.; Choi, H. C.; Schmeltzer, J. M.; Ribbe, A. E.; Elliott, L. C. C.; Buriak, J. M. *Nano Letters* **2002**, *2*, 1369-1372.

(50) Niwa, D.; Homma, T.; Osaka, T. *Journal of Physical Chemistry B* **2004**, *108*, 9900-9904.

(51) Gorostiza, P.; Allongue, P.; Diaz, R.; Morante, J. R.; Sanz, F. *Journal of Physical Chemistry B* **2003**, *107*, 6454-6461.

(52) Sun, Y. G.; Wiederrecht, G. P. *Small* **2007**, *3*, 1964-1975.

(53) Sun, X. H.; Wong, N. B.; Li, C. P.; Lee, S. T.; Kim, P. S. G.; Sham, T. K. *Chemistry of Materials* **2004**, *16*, 1143-1152.

(54) Bhuvana; Kulkarni, G. U. *Bulletin of Materials Science* **2006**, *29*, 505-511.

(55) Jing, F.; Tong, H.; Kong, L.; Wang, C. *Applied Physics A-Materials Science & Processing* **2005**, *80*, 597-600.

(56) Ye, X. R.; Wai, C. M.; Zhang, D. Q.; Kranov, Y.; McIlroy, D. N.; Lin, Y. H.; Engelhard, M. *Chemistry of Materials* **2003**, *15*, 83-91.

(57) Miyake, H.; Ye, S.; Osawa, M. *Electrochemistry Communications* **2002**, *4*, 973-977.

(58) Lv, S.; Suo, H.; Zhou, T. L.; Wang, C. X.; Jing, S. Y.; Fu, Q. B.; Xu, Y. A.; Zhao, C. *Solid State Communications* **2009**, *149*, 227-230.

(59) Darosa, C. P.; Iglesia, E.; Maboudian, R. *Journal of the Electrochemical Society* **2008**, *155*, D244-D250.

(60) Gao, D.; He, R. R.; Carraro, C.; Howe, R. T.; Yang, P. D.; Maboudian, R. *Journal of the American Chemical Society* **2005**, *127*, 4574-4575.

(61) Niwa, D.; Homma, T.; Osaka, T. *Journal of the Electrochemical Society* **2005**, *152*, C54-C59.

(62) Lin, H. H.; Mock, J.; Smith, D.; Gao, T.; Sailor, M. J. *Journal of Physical Chemistry B* **2004**, *108*, 11654-11659.

(63) Kim, C.; Oikawa, Y.; Shin, J.; Ozaki, H. *Microelectronics Journal* **2003**, *34*, 607-609.

(64) Srinivasan, R.; Suni, II *Surface Science* **1998**, *408*, L698-L702.

(65) Srinivasan, R.; Suni, II *Journal of the Electrochemical Society* **1999**, *146*, 570-573.

(66) Peng, K. Q.; Zhu, J. *Journal of Electroanalytical Chemistry* **2003**, *558*, 35-39.

(67) Weller, R. A.; Ryle, W. T.; Newton, A. T.; McMahon, M. D.; Miller, T. M.; Magruder, R. H. *IEEE Transactions on Nanotechnology* **2003**, *2*, 154-157.

(68) Sugimura, H.; Nakagiri, N. *Journal of Vacuum Science & Technology B* **1995**, *13*, 1933-1937.

(69) Sayed, S. Y.; Wang, F.; Mallac, M.; Meldrum, A.; Egerton, R. F.; Buriak, J. M. *ACS Nano* **2009**, *3*, 2809-2817.

(70) Doerk, G. S.; Ferralis, N.; Carraro, C.; Maboudian, R. *Journal of Materials Chemistry* **2008**, *18*, 5376-5381.

(71) Yasseri, A. A.; Sharma, S.; Jung, G. Y.; Kamins, T. I. *Electrochemical and Solid State Letters* **2006**, *9*, C185-C188.

(72) Yasseri, A. A.; Sharma, S.; Kamins, T. I.; Li, Z.; Williams, R. S. *Applied Physics A-Materials Science & Processing* **2006**, *82*, 659-664.

(73) Warren, S.; Reitzle, A.; Kazimirov, A.; Ziegler, J. C.; Bunk, O.; Cao, L. X.; Renner, F. U.; Kolb, D. M.; Bedzyk, M. J.; Zegenhagen, J. *Surface Science* **2002**, *496*, 287-298.

(74) Rossiter, C.; Suni, II *Surface Science* **1999**, *430*, L553-L557.

(75) Ferralis, N.; Maboudian, R.; Carraro, C. *Journal of Physical Chemistry C* **2007**, *111*, 7508-7513.

(76) Zhang, J. G.; Gao, Y.; Hanrath, T.; Korgel, B. A.; Buriak, J. M. *Chemical Communications* **2007**, 1438-1440.

(77) Magagnin, L.; Maboudian, R.; Carraro, C. *Electrochemical and Solid State Letters* **2001**, *4*, C5-C7.

(78) Yae, S.; Nasu, N.; Matsumoto, K.; Hagihara, T.; Fukumuro, N.; Matsuda, H. *Electrochimica Acta* **2007**, *53*, 35-41.

(79) Piscopiello, E.; Tapfer, L.; Antisari, M. V.; Paiano, P.; Prete, P.; Lovergine, N. *Physical Review B* **2008**, *78*, 0353051 - 0353057.

(80) Arakaki, H.; Ohashi, K.; Sudou, T. *Semiconductor Science and Technology* **2004**, *19*, 127-132.

(81) Bravo-Vasquez, J.-P.; Fenniri, H. *J. Phys. Chem. C* **2009**, *113*, 12897-12900.

(82) Osaka, T.; Takano, N.; Komaba, S. *Chemistry Letters* **1998**, 657-658.

(83) Morinaga, H.; Suyama, M.; Ohmi, T. *Journal of the Electrochemical Society* **1994**, *141*, 2834-2841.

(84) Nagahara, L. A.; Ohmori, T.; Hashimoto, K.; Fujishima, A. *Journal of Vacuum Science & Technology A-Vacuum Surfaces and Films* **1993**, *11*, 763-767.

(85) Harraz, F. A.; Sakka, T.; Ogata, Y. H. *Physica Status Solidi (A) Applied Research* **2003**, *197*, 51-56.

(86) Ye, S.; Ichihara, T.; Uosaki, K. *Journal of the Electrochemical Society* **2001**, *148*, C421-C426.

(87) Lombardi, I.; Marchionna, S.; Zangari, G.; Pizzini, S. *Langmuir* **2007**, *23*, 12413-12420.

(88) Ogata, Y. H.; Sasano, J.; Itoh, T.; Sakka, T.; RayoÌ n, E.; Pastor, E.; Parkhutik, V. *Journal of the Electrochemical Society* **2005**, *152*, C537-C541.

(89) Cheng, X.; Li, G.; Kneer, E. A.; Vermeire, B.; Parks, H. G.; Raghavan, S.; Jeon, J. S. *Journal of the Electrochemical Society* **1998**, *145*, 352-357.

(90) Li, G.; Kneer, E. A.; Vermeire, B.; Parks, H. G.; Raghavan, S.; Jeon, J. S. *Journal of the Electrochemical Society* **1998**, *145*, 241-246.

(91) Lee, M. K.; Wang, J. J.; Wang, H. D. *Journal of the Electrochemical Society* **1997**, *144*, 1777-1780.

(92) Martins, L. F. O.; Seligman, L.; Santos Filho, S. G.; D'Ajello, P. C. T.; Hasenack, C. M.; Pasa, A. A. *Journal of the Electrochemical Society* **1997**, *144*, L106-L108.

(93) Gorostiza, P.; Diaz, R.; Sanz, F.; Morante, J. R. *Journal of the Electrochemical Society* **1997**, *144*, 4119-4122.

(94) Rickerby, J.; Steinke, J. H. G. *Chemical Reviews* **2002**, *102*, 1525-1549.

(95) Campion, A.; Kambhampati, P. *Chemical Society Reviews* **1998**, *27*, 241-250.

(96) Fleischm.M; Hendra, P. J.; McQuilla.Aj *Chemical Physics Letters* **1974**, *26*, 163-166.

(97) Jeanmaire, D. L.; Vanduyne, R. P. *Journal of Electroanalytical Chemistry* **1977**, *84*, 1-20.

(98) Creighton, J. A.; Blatchford, C. G.; Albrecht, M. G. *Journal of the Chemical Society-Faraday Transactions 2: Molecular and Chemical Physics* **1979**, *75*, 790-798.

(99) Albrecht, M. G.; Creighton, J. A. *Journal of the American Chemical Society* **1977**, *99*, 5215-5217.

(100) Li, W. Y.; Camargo, P. H. C.; Lu, X. M.; Xia, Y. N. *Nano Letters* **2009**, *9*, 485-490.

(101) Alexander, K. D.; Hampton, M. J.; Zhang, S. P.; Dhawan, A.; Xu, H. X.; Lopez, R. *Journal of Raman Spectroscopy* **2009**, *40*, 2171-2175.

(102) Camargo, P. H. C.; Cobley, C. M.; Rycenga, M.; Xia, Y. N. *Nanotechnology* **2009**, *20*.

(103) Camargo, P. H. C.; Rycenga, M.; Au, L.; Xia, Y. N. *Angewandte Chemie-International Edition* **2009**, *48*, 2180-2184.

(104) Guerrini, L.; Garcia-Ramos, J. V.; Domingo, C.; Sanchez-Cortes, S. *Journal of Physical Chemistry C* **2008**, *112*, 7527-7530.

(105) Brus, L. *Accounts of Chemical Research* **2008**, *41*, 1742-1749.

(106) Wang, Y.; Becker, M.; Wang, L.; Liu, J. Q.; Scholz, R.; Peng, J.; Gosele, U.; Christiansen, S.; Kim, D. H.; Steinhart, M. *Nano Letters* **2009**, *9*, 2384-2389.

(107) Stranahan, S. M.; Willets, K. A. *Nano Letters* **2010**, *10*, 3777-3784.

(108) Gutes, A.; Carraro, C.; Maboudian, R. *ACS Applied Materials & Interfaces* **2009**, *1*, 2551-2555.

(109) Gutes, A.; Laboriante, I.; Carraro, C.; Maboudian, R. *Journal of Physical Chemistry C* **2009**, *113*, 16939-16944.

(110) Brejna, P. R.; Griffiths, P. R.; Yang, J. *Applied Spectroscopy* **2009**, *63*, 396-400.

(111) Wu, Y. Y.; Yang, P. D. *Journal of the American Chemical Society* **2001**, *123*, 3165-3166.

(112) Wu, Y. Y.; Fan, R.; Yang, P. D. *Nano Letters* **2002**, *2*, 83-86.

(113) Goldberger, J.; Hochbaum, A. I.; Fan, R.; Yang, P. D. *Nano Letters* **2006**, *6*, 973-977.

(114) Law, M.; Greene, L. E.; Johnson, J. C.; Saykally, R.; Yang, P. D. *Nature Materials* **2005**, *4*, 455-459.

(115) Lexholm, M.; Hessman, D.; Samuelson, L. *Nano Letters* **2006**, *6*, 862-865.

(116) Lieber, C. M.; Wang, Z. L. *MRS Bulletin* **2007**, *32*, 99-108.

(117) Jun, K.; Jacobson, J. M. *Nano Letters* **2010**, *10*, 2777-2782.

(118) Schmidt, V.; Senz, S.; Gosele, U. *Nano Letters* **2005**, *5*, 931-935.

(119) Shimizu, T.; Senz, S.; Shingubara, S.; Gosele, U. *Applied Physics A-Materials Science & Processing* **2007**, *87*, 607-610.

(120) Shimizu, T.; Xie, T.; Nishikawa, J.; Shingubara, S.; Senz, S.; Gosele, U. *Advanced Materials* **2007**, *19*, 917-920.

(121) Zhang, Z.; Shimizu, T.; Senz, S.; Gosele, U. *Advanced Materials* **2009**, *21*, 2824-2824.

(122) Celle, C.; Mouchet, C.; Rouviere, E.; Simonato, J. P.; Mariolle, D.; Chevalier, N.; Brioude, A. *Journal of Physical Chemistry C* **2010**, *114*, 760-765.

(123) Fukata, N.; Sato, K.; Mitome, M.; Bando, Y.; Sekiguchi, T.; Kirkham, M.; Hong, J. I.; Wang, Z. L.; Snyder, R. L. *ACS Nano* **2010**, *4*, 3807-3816.

(124) Wolfsteller, A.; Geyer, N.; Nguyen-Duc, T. K.; Das Anungo, P.; Zakharov, N. D.; Reiche, M.; Erfurth, W.; Blumtritt, H.; Werner, P.; Gosele, U. *Thin Solid Films* **2010**, *518*, 2555-2561.

(125) Peng, K.; Wu, Y.; Fang, H.; Zhong, X.; Xu, Y.; Zhu, J. *Angewandte Chemie - International Edition* **2005**, *44*, 2737-2742.

(126) Peng, K.; Hu, J.; Yan, Y.; Wu, Y.; Fang, H.; Xu, Y.; Lee, S.; Zhu, J. *Advanced Functional Materials* **2006**, *16*, 387-394.

(127) Hochbaum, A. I.; Chen, R. K.; Delgado, R. D.; Liang, W. J.; Garnett, E. C.; Najarian, M.; Majumdar, A.; Yang, P. D. *Nature* **2008**, *451*, 163-U165.

(128) Herman, M. A., Richter, W. & Sitter, H. *Epitaxy; Physical Principles and Technical Implementation*; Springer 2004.

(129) Rota, A.; Martinez-Gil, A.; Agnus, G.; Moyen, E.; Maroutian, T.; Bartenlian, B.; Megy, R.; Hanbucken, M.; Beauvillain, P. *Surface Science* **2006**, *600*, 1207-1212.

(130) Kirakosian, A.; Lin, J. L.; Petrovykh, D. Y.; Crain, J. N.; Himpsel, F. J. *Journal of Applied Physics* **2001**, *90*, 3286-3290.

(131) Cantor, B.; Grovenor, C. R. M. *Graduate Student Series in Materials Science and Engineering -Microelectronic Materials*; Institute of Physics Publishing: London, 1989.

(132) Pretorius, R. *Vacuum* **1990**, *41*, 1038-1042.

(133) Oura, K.; Hanawa, T. *Surface Science* **1979**, *82*, 202-214.

(134) Green, A. K.; Bauer, E. *Journal of Applied Physics* **1976**, *47*, 1284-1291.

(135) Sundaravel, B.; Sekar, K.; Kuri, G.; Satyam, P. V.; Dev, B. N.; Bera, S.; Narasimhan, S. V.; Chakraborty, P.; Caccavale, F. *Applied Surface Science* **1999**, *137*, 103-112.

(136) Sohn, Y.; Pradhan, D.; Radi, A.; Leung, K. T. *Langmuir* **2009**, *25*, 9557-9563.

(137) Collings, P. J. *American Journal of Physics* **1980**, *48*, 197-199.

(138) Song, Y. Y.; Jia, W. Z.; Li, Y.; Xia, X. H.; Wang, Q. J.; Zhao, J. W.; Yan, Y. D. *Advanced Functional Materials* **2007**, *17*, 2808-2814.

(139) Zhang, C. X.; Chen, P.; Liu, J.; Zhang, Y. H.; Shen, W.; Xu, H. L.; Tang, Y. *Chemical Communications* **2008**, 3290-3292.

(140) Peng, K. Q.; Wang, X.; Lee, S. T. *Applied Physics Letters* **2009**, *95*.

(141) Vickerman, J. C.; Gilmore, I. S. *Surface Analysis - The Principal Techniques (2nd Edition)*; Wiley, 2009.

(142) Silberberg, M. *Chemistry: The Molecular Nature of Matter and Change*; McGraw-Hill.

(143) Iwami, M.; Terada, T.; Tochihara, H.; Kubota, M.; Murata, Y. *Surface Science* **1988**, *194*, 115-126.

(144) Monch, W. *Europhysics Letters* **1988**, *7*, 275-279.

(145) Lu, Z. H.; Sham, T. K.; Norton, P. R. *Solid State Communications* **1993**, *85*, 957-959.

(146) Wolffenbuttel, R. F. *Sensors and Actuators a-Physical* **1997**, *62*, 680-686.

(147) Ananthar.Tr; Luo, H. L.; Klement, W. *Nature* **1966**, *210*, 1040-&.

(148) Molodtsov, S. L.; Laubschat, C.; Kaindl, G.; Shikin, A. M.; Adamchuk, V. K. *Physical Review B* **1991**, *44*, 8850.

(149) Gheber, L. A.; Hershfinkel, M.; Gorodetsky, G.; Volterra, V. *Thin Solid Films* **1998**, *320*, 228-235.

(150) Feenstra, R. M. *Physical Review Letters* **1989**, *63*, 1412-1415.

(151) Gupta, B. C.; Konar, S.; Bose, R. P. *Applied Surface Science* **2009**, *256*, 495-498.

(152) Warren, S.; Prod'homme, P.; Maroun, F.; Allongue, P.; Cortes, R.; Ferrero, C.; Lee, T. L.; Cowie, B. C. C.; Walker, C. J.; Ferrer, S.; Zegenhagen, J. *Surface Science* **2009**, *603*, 1212-1220.

(153) Gorostiza, P.; Servat, J.; Morante, J. R.; Sanz, F. *Thin Solid Films* **1996**, *275*, 12-17.

(154) Birkholz, M. *Thin Film Analysis by X-Ray Scattering*; WILEY-VCH Verlag Gmbh & Co. KGaA, Weinheim, 2006.

(155) Sayed, S. Y.; Buriak, J. M. *ACS Applied Materials & Interfaces* **2010**, *2 (12)*, 3515–3524.

(156) Detavernier, C.; Ozcan, A. S.; Jordan-Sweet, J.; Stach, E. A.; Tersoff, J.; Ross, F. M.; Lavoie, C. *Nature* **2003**, *426*, 641-645.

(157) Tang, F.; Parker, T.; Wang, G. C.; Lu, T. M. *Journal of Physics D-Applied Physics* **2007**, *40*, R427-R439.

(158) Suguro, K. *IEEE* **2006**, *1-4244-0047-3*, 139-142.

Chapter 2

Characterization of the Interface of Gold and Silver Nanostructures on InP and GaAs, Synthesized via Galvanic Displacement

2.1. Introduction

The use of III-V compound semiconductors has emerged as a multi-billion dollar industry since these materials meet system performance requirements not attainable with silicon and germanium.[1, 2] The primary advantages of GaAs and InP, both direct band gap (III-V) semiconductors, over silicon arise from their electrical properties, including higher electron mobility, lower turn-on voltages, and higher breakdown voltages.[2-6] These are fundamental properties that enable higher frequencies of operation and faster switching speeds. The superior properties of GaAs and InP are integral to the materialization of new commercial markets, in areas such as next generation mobile phones, satellite communications, and photovoltaics.

Galvanic displacement of noble metals on gallium arsenide to produce metal-GaAs junctions has been studied intermittently, starting with two reports of gold on GaAs by Gol'derberg in 1971,[7] and Donzelli in 1978.[8] The group of Sun, and our group, have investigated the silver on GaAs, and gold on GaAs and InP, respectively, but the focus in both cases was on the resulting metallic nanostructures, and not the nature of the interface.[9-11] Substantial early research was undertaken on Au-InP[12-17] and Au-GaAs[18-21] systems prepared at high temperatures (>300ºC) *via* metal evaporation, and in many cases, formation of a layered semiconductor-intermetallic-metal structure was suggested. One room temperature study of gold on a variety of semiconductors, prepared *via* e-beam evaporation in vacuum, also points to formation of such a layered structure, although the composition of the interface was not characterized.[22] The interfacial composition that would have a direct effect on the resulting electrical nature of these junctions remains poorly understood. In this chapter, we focus upon the characterization of the interface between metals (gold and silver) and semiconductors (GaAs and InP) formed at room temperature by galvanic displacement through a variety of methods, including Auger electron spectroscopy (AES) and X-ray photoelectron spectroscopy (XPS) depth profiling methods.

2.2. Results and Discussion

2.2.1. Au on GaAs and InP

Galvanic displacement occurs spontaneously when a semiconductor is immersed in a solution of sufficiently oxidizing metal ions (see Figure 1.4). When a shard of cleaned GaAs(100) is immersed in 1 mM $KAuCl_4$ (aq), a gold film forms on the surface (Figure 2.1) as a result of reducing gold ions on the oxidized GaAs surface according to equation (1):[10]

$$4\ \mathrm{KAuCl_4\,(aq)} + 2\ \mathrm{GaAs\,(s)} + 6\ \mathrm{H_2O\,(aq)} \rightarrow$$

$$4\ \mathrm{Au^o\,(s)} + 4\ \mathrm{KCl\,(s)} + \mathrm{Ga_2O_3\,(s)} + \mathrm{As_2O_3\,(s)} + 12\ \mathrm{HCl\,(s)} \qquad (1)$$

This spontaneous reaction occurred because of the more positive reduction potential of the Au^{3+}/Au couple (1.42 V vs NHE) compared to those of the Ga^{3+}/Ga (-0.56 V versus NHE) and the As^{3+}/As (0.234 V versus NHE) couples.[10, 23]

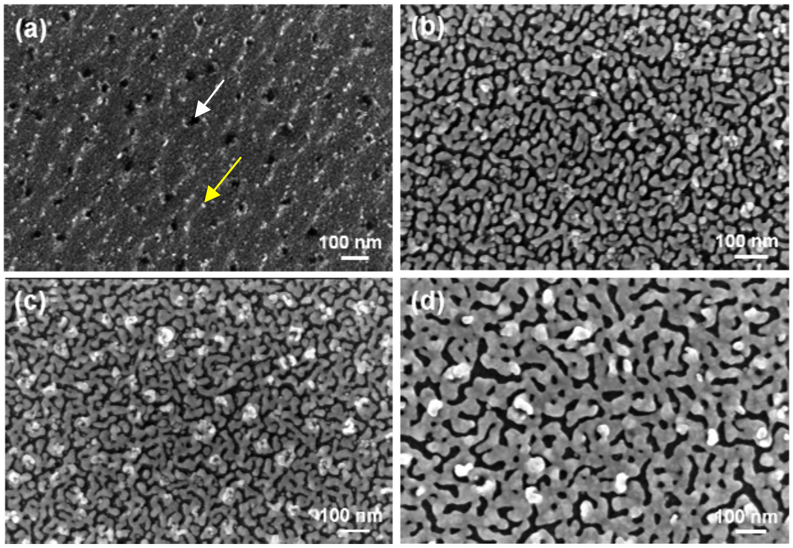

Figure 2.1. *Scanning electron micrographs for Au films on GaAs(100) produced after immersion in 1 mM $KAuCl_4$ (aq) for 1 min (a), 3 min (b), 5 min (c), and 10 min (d), respectively. White and yellow arrows (image a) refer to a formed pit and a gold particle on a GaAs surface, respectively.*[24]

At the early stages of deposition, after immersion of GaAs in the gold salt solution for 1 min, corrosion of GaAs occurs as revealed from the pit formation marked by the white arrow in Figure 2.1a. Consequently, deposition and formation of gold nuclei, marked by the yellow arrow in Figure 2.1a, occur. Prolonged immersion of GaAs shards in the gold salt solutions results in a higher degree of coverage and film formation as a result of the subsequent gold deposition and coalescence of gold islands (Figure 2.1b-d). The evolution of the gold deposit morphology starting from nuclei to grains and finally film formation with increasing immersion time is seen in Figure 2.1. This points to a three dimensional (3D), island or Volmer Weber (VW) growth mode of gold on GaAs by GD process.[25] A VW growth mode has also been reported for the deposition of gold on silicon[25-28] and germanium[29] surfaces by galvanic displacement. Glancing incidence X-ray diffraction (GIXRD) pattern (Figure 2.2) reveals crystalline gold on GaAs. It is worth noting that deposition of gold on scratched GaAs areas (exposed GaAs substrate – no surface oxides) from the gold salt solution and in the absence of an acid source was reported by Nezhad and co-workers.[11] The presence of an acid is not necessary since Ga_2O_3 and As_2O_3 are somewhat water soluble*[30]* (solubility of $As_2O_3 > Ga_2O_3$).[31, 32]

Galvanic displacement on InP(100) does, however, require the presence of an acid such as H_2SO_4 (aq) to dissolve the insulating oxide, which forms during the process, prevents electron transfer, and stops the reaction.[11] Immersion of InP(100) in 1 mM $KAuCl_4$ (aq) + 2% H_2SO_4 (aq) and in the absence of any obvious directing agent resulted in the formation of crystalline nanoparticles of various shapes such as icosahedra, triangular and hexagonal plates and others as shown in Figure 2.3(a, b).[11, 24] The average size of gold nanoparticles under these conditions is approximately 60 nm in diameter.

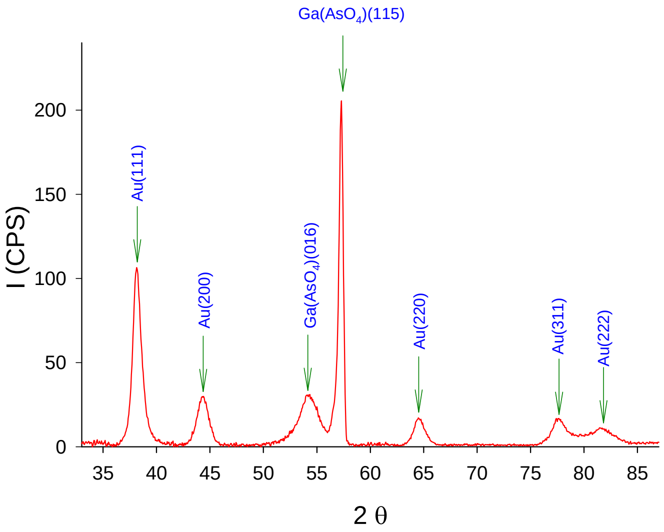

***Figure 2.2**. Glancing incident X-ray diffraction (GIXRD) pattern, collected with an incident angle $\omega = 3^o$, of a Au film on GaAs(100) grown after immersion in 1 mM $KAuCl_4$ (aq) for 3 min. The crystallographic identifications of all the Au and $Ga(AsO_4)$ peaks are labeled according to JCPDS reference tables, (Au-JCPDS 65-2870) and ($Ga(AsO_4)$-JCPDS 89-1365).[24]*

GIXRD pattern (Figure 2.4) reveals crystalline gold nanoparticles on InP. The reason for the formation of gold nanoparticles of different shapes in the absence of structure directing agent is not clear.[11] However, considering the composition of the reaction mixture (sulphate, gold, and chloride ions) and the product of the galvanic displacement process such as oxides of phosphorous and indium, it is probable that one or more of the solution-species may direct the growth of each of the formed shapes.[11]

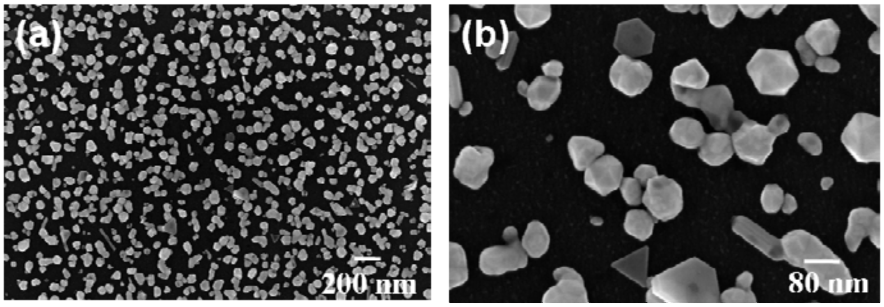

Figure 2.3. *(a-b) SEM images of gold nanostructures on InP(100) produced after immersion for 30 min in a 10 ml solution of 1 mM* $KAuCl_4$ *and 2%* H_2SO_4 *(aq).*[24]

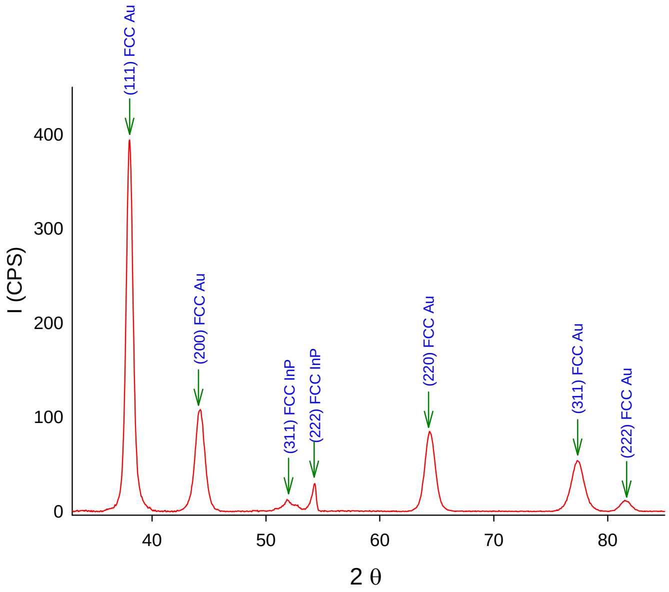

Figure 2.4. *GIXRD pattern, collected with an incident angle* $\omega = 3^o$, *of gold nanostructures on InP(100). The deposition was carried out via immersion of InP(100), for 30 min in a 10 ml solution of 1 mM* $KAuCl_4$ *and 2%* H_2SO_4 *(aq). The crystallographic identifications of all the Au and InP peaks are labeled according to JCPDS reference tables, (Au-JCPDS 65-2870) and (InP-JCPDS 65-233).*[24]

In order to characterize the interface between gold and GaAs and InP, XPS depth profiling was carried out. Two samples were analyzed for their interfacial composition: Au on GaAs(100), prepared by immersion of GaAs shards in 1 mM $KAuCl_4$ (aq) for 3 min, and Au on InP(100), prepared by immersion in a mixture of 1 mM $KAuCl_4$ (aq) + 2% H_2SO_4 (aq) for 30 min. Elemental analyses from survey scans have shown the expected series of photoemission peaks arising from Au $4f_{7/2}$ (83.9 eV), O 1s (531.2 eV), and C 1s (284.8 eV), as well as Ga 3d, As 2p in the case of GaAs (Figure 2.5) and In $3d_{5/2}$ (443.9 eV), P $2p_{3/2}$ (129.5 eV) for InP (Figure 2.6). Depth profiling shows the change in the atomic concentration with sputtering time – the peak for Au^0 decreased linearly over time and concurrently, the peaks for the underlying semiconductor increase as the gold film was removed with the sputtering (Figure 2.7).

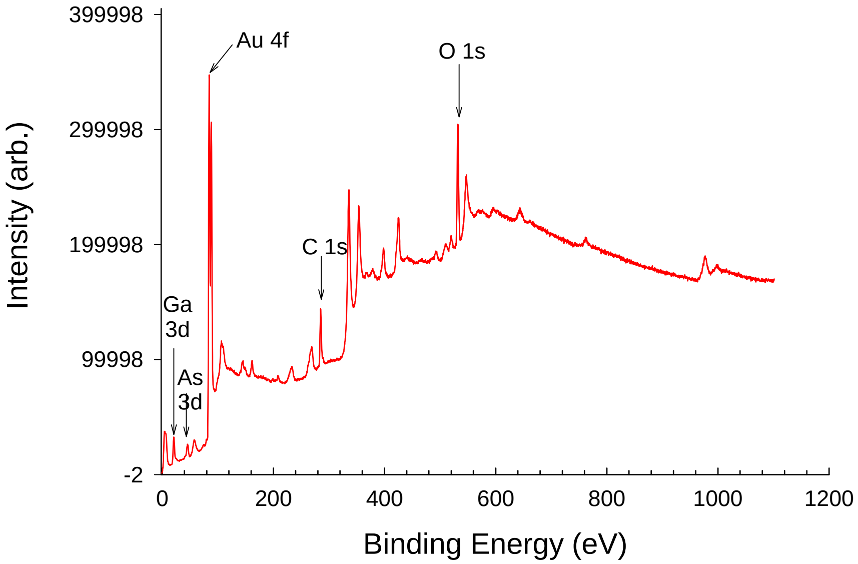

Figure 2.5. *Survey scan of Au on GaAs(100) from 1 to 1200 eV. The Au 4f, Ga 3d, As 3d, C 1s and O 1s peaks are labeled.*[24]

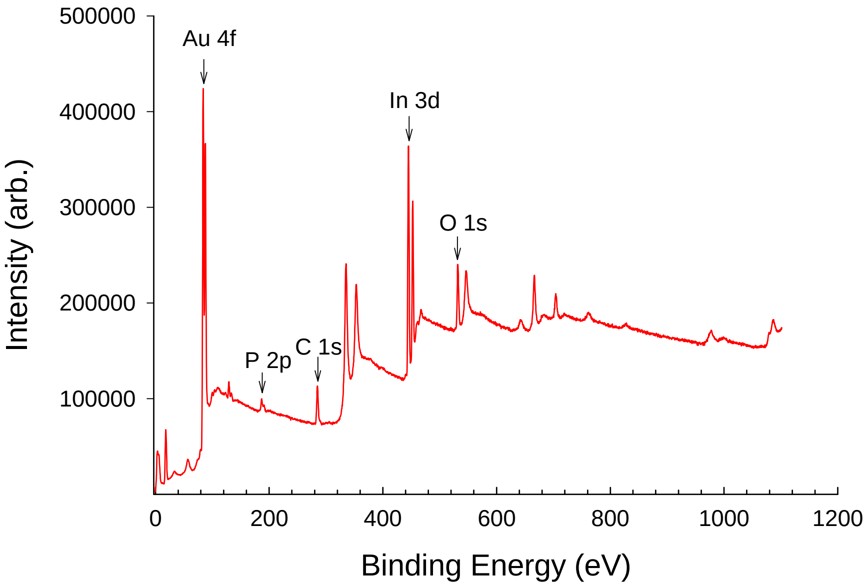

Figure 2.6. *Survey scan of Au on InP(100) from 1 to 1200 eV. The Au 4f, In 3d, P 2p, C 1s and O 1s peaks are labeled.*[24]

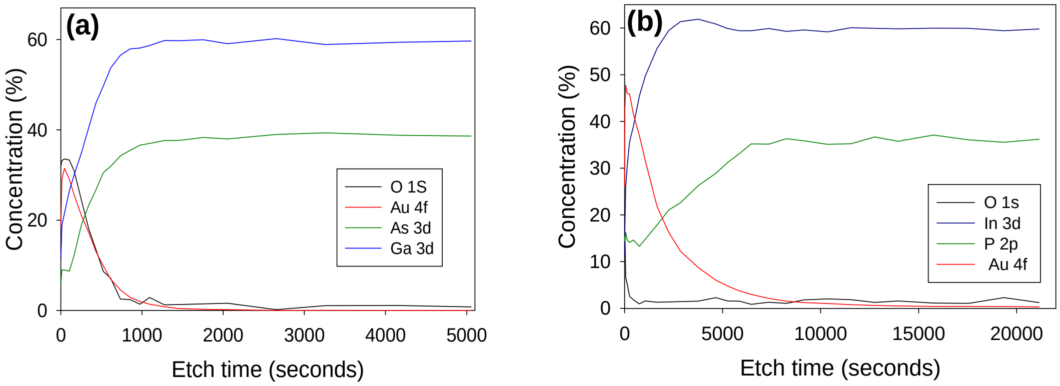

Figure 2.7. *XPS depth profiles for Au on GaAs(100) (a), and InP(100) (b).*[24]

High resolution Au 4f spectra for Au on GaAs (Figure 2.8a) and InP (Figure 2.8b) show that the only feature visible for gold before sputtering is the Au^{o} peak at 83.95 eV.[33] For GaAs at early stages in the sputtering process (7.5 min), a broad peak becomes visible at 84.89 eV, as shown in Figure 2.8a. Further sputtering leads to the appearance of a second new peak at 85.29 eV, at which point the peak for Au^{o} has almost completely vanished; the 85.29 eV feature is clearly observed at the bottom of the Au-GaAs interface and is the last gold feature to be removed during sputtering. Similar results are observed for InP (Figure 2.8b): two intermediate peaks are again visible with the first broad peak appearing at 84.75 eV and the second sharp peak at 85.10 eV. Concurrently, the peak at 83.95 eV (pure gold) disappears throughout the course of sputtering.

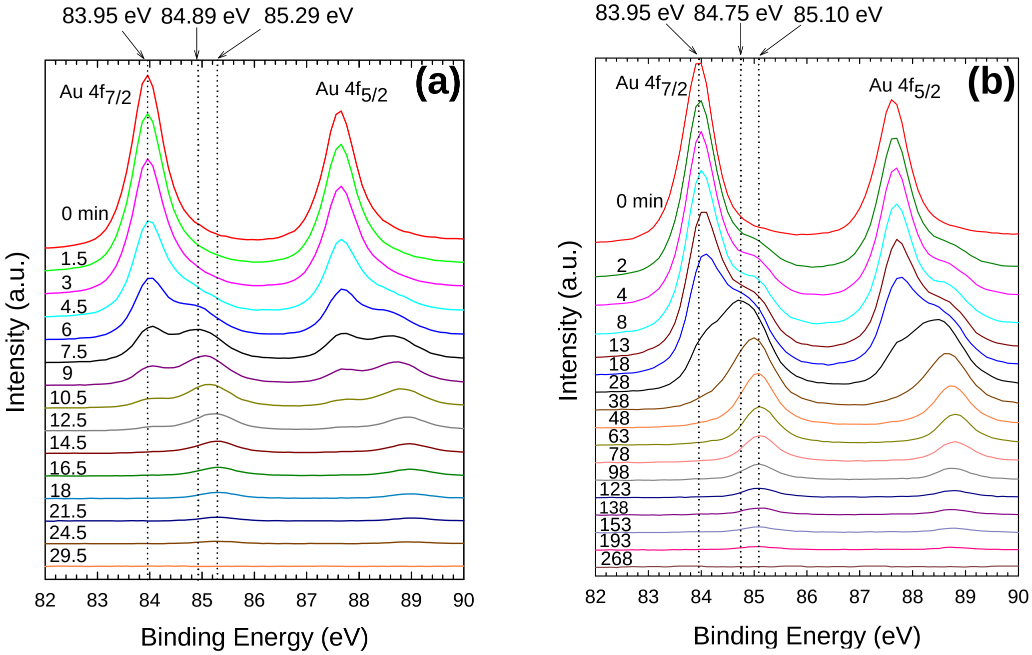

Figure 2.8. *(a) Au 4f XPS spectra, at different* Ar^+ *sputtering time intervals, of Au on GaAs(100), formed by immersion of the GaAs shards in 1 mM* $KAuCl_4$ *(aq). (b) Au 4f XPS spectra, at different* Ar^+ *sputtering time intervals, of Au on InP(100), formed by immersion in 1 mM* $KAuCl_4$ *and 2%* H_2SO_4 *(aq).*[24]

Curve fitting was carried out only in the region known to contain the Au 4f peaks. The deconvolution of the broad Au $4f_{7/2}$ peaks was carried out on the spectra observed after 7.5 min of sputtering for Au/GaAs(100) (Figure 2.9a), and after 28 min for Au/InP(100) (Figure 2.9b). In both cases deconvolution revealed two additional gold features other than metallic gold. The binding energies of the deconvoluted peaks are 84.01, 84.82 and 85.20 eV in the case of GaAs(100), and 84.08, 84.73, and 85.12 eV for InP(100), respectively. The binding energies of the additional gold features fall comfortably in the range of known intermetallics for both cases (*vide infra*).

There are five known room temperature stable phases of Au and Ga: α-$Au_{0.88}Ga_{0.12}$, β-$Au_{0.78}Ga_{0.22}$, γ-Au_9Ga_4, AuGa and $AuGa_2$, and the observed binding energies of their Au $4f_{7/2}$ peaks, formed *via* electron beam melting of the correct Au and Ga weight ratios in vacuum, are reported to appear at 84.39, 84.59, 84.86, 85.24, and 85.51 eV, respectively.[34] The deconvoluted peak (Figure 2.9a) at 84.84 eV falls closest to γ-Au_9Ga_4, while the deconvoluted peak at 85.20 eV may be the gallium rich phase, AuGa.

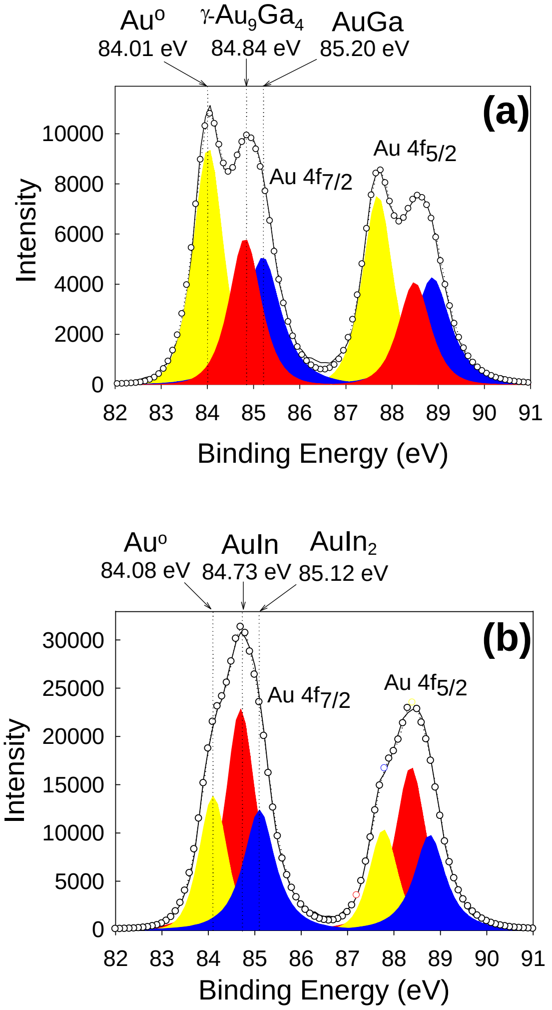

Figure 2.9. *Curve fitting analysis of (a) the Au 4f peaks observed after Ar*$^+$ *sputtering Au on GaAs(100) for 7.5 min, and on InP(100) for 28 min (b). The solid line represents the experimental data, the colored peaks are the corresponding fitted peaks, and the open circles with dotted lines are the sum of the fitted peaks.*[24]

The Ga XPS spectra are not informative because the difference in Ga core level binding energies over the compositional range between α-$Au_{0.88}Ga_{0.12}$ and $AuGa_2$ is only 0.15 eV;[34] we did not observe any discernable shift (Figure

2.10a).[24] For As on the other hand, only two peaks at 41.1 (GaAs)[35, 36] and 41.6 eV (As^o)[37] were observed after 12.5 min of sputtering (Figure 2.10b) – no Au-As intermetallics were seen by XPS of arsenic.[24] This result is not unexpected because earlier work showed that the annealing of Au on GaAs at high temperatures resulted only in the formation of Au-Ga binary phases, and the volatilization of As from the surface.[19] Furthermore, As is insoluble in Au.[38, 39] In the case of aqueous, room temperature galvanic displacement, the excess arsenic is most likely converted to water-solubilized arsenic oxides. To summarize the Au on GaAs case, depth profile XPS indicates a multilayer structure starting with the more gallium rich Au^o intermetallic alloy at the interface with GaAs, topped by a more gold rich intermetallic alloy that is covered by the deposited metallic gold.

XPS analysis of room temperature stable intermetallic phases of Au and In showed that the Au $4f_{7/2}$ binding energies appeared at 84.20, 84.80, 85.15 and 84.50 eV, corresponding to Au (10% In), AuIn, $AuIn_2$, and Au_3In, respectively.[40] Using a similar argument to the GaAs system, the deconvoluted peaks at 84.73 and 85.12 eV most likely correspond to AuIn, and $AuIn_2$, respectively. In addition, a small shift in the In $3d_{5/2}$ of 0.17 eV towards a lower binding energy was observed (Figure 2.11a). However, it is hard to differentiate between the AuIn and $AuIn_2$ phases by considering their In $3d_{5/2}$ binding energies.[40] XPS analysis of the P 2p peaks did not reveal any evidence of an intermetallic alloy between Au and P (Figure 2.11b).[24]

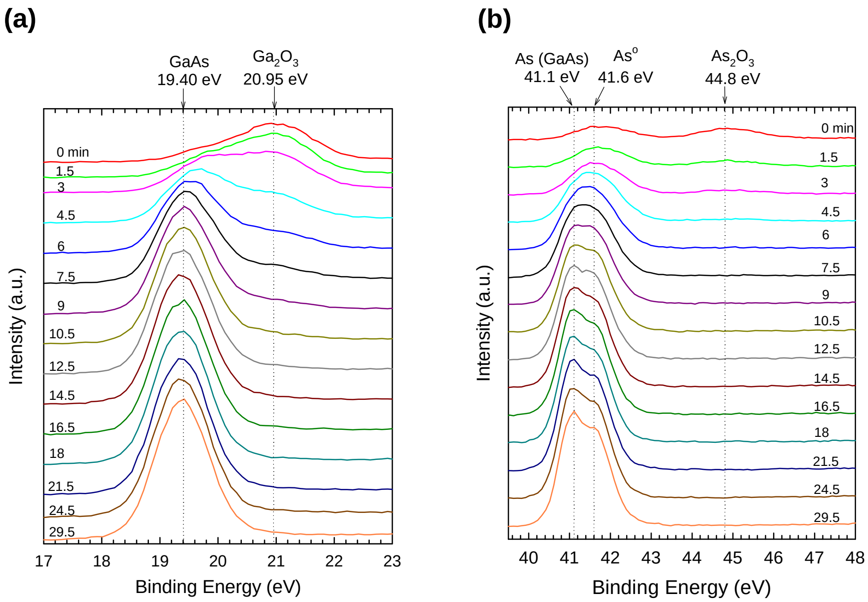

Figure 2.10. *(a) Ga $3d_{5/2}$ XPS spectra of Au on GaAs(100). (b) As 3d XPS spectra of Au on GaAs(100) after Ar$^+$ sputtering at different time intervals.*[24]

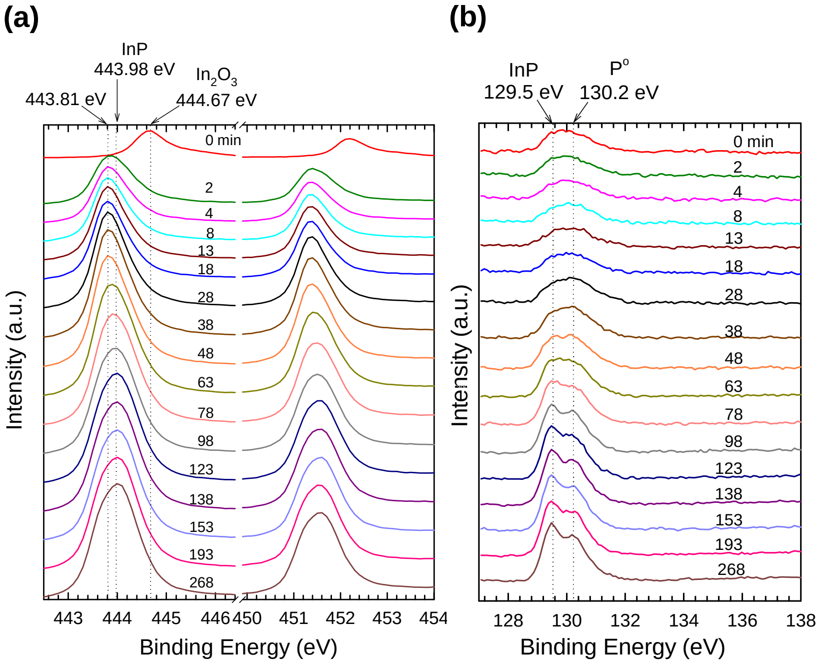

Figure 2.11. *(a) In $3d_{5/2}$ XPS spectra of Au on InP(100). (b) P 2p XPS spectra of Au on InP(100) after Ar$^+$-sputtering at different time intervals.*[24]

It is worth noting the endothermic reaction [heat of reaction (ΔH_{rxn}) = + 1.73 eV/mole] between Au and InP to produce Au_2P_3 ($2Au + 3InP \rightarrow Au_2P_3 + 3In$) accounting for the stability of InP over Au_2P_3.[13] This may explain the absence of interfacial gold-phosphorus intermetallic for the room temperature Au-InP samples prepared by galvanic displacement.

Up to now there has been scant evidence revealing the direction of elemental diffusion across the semiconductor metal interface - does the metal diffuse into the substrate and/or vice versa? An earlier study examining gold on semiconductors at room temperature (e-beam evaporation) suggested a sandwich structure in which there is an abrupt semiconductor-intermetallic interface, capped with the metal through which the semiconductor elements can diffuse.[22] Weizer and co-workers have found that both Ga (at high temperature)[18] and In (at room temperature)[16] enter the gold lattice *via* a dissociative diffusion mechanism or interstitial-substitutional diffusion – Ga atoms leave their substitutional sites in the substrate lattice and enter the gold layer as interstitials.

Cross-section scanning Auger electron line profile spectra (Figures 2.12a-b) and higher resolution cross-section SEM images (Figures 2.12c-d) were taken to provide some insight into the direction of elemental diffusion. In the case of GaAs, there is pitting and obvious undercutting (Figure 2.12c), whereas in the case of InP, a smooth interface between a semiconductor and the metal is visible (Figure 2.12d).

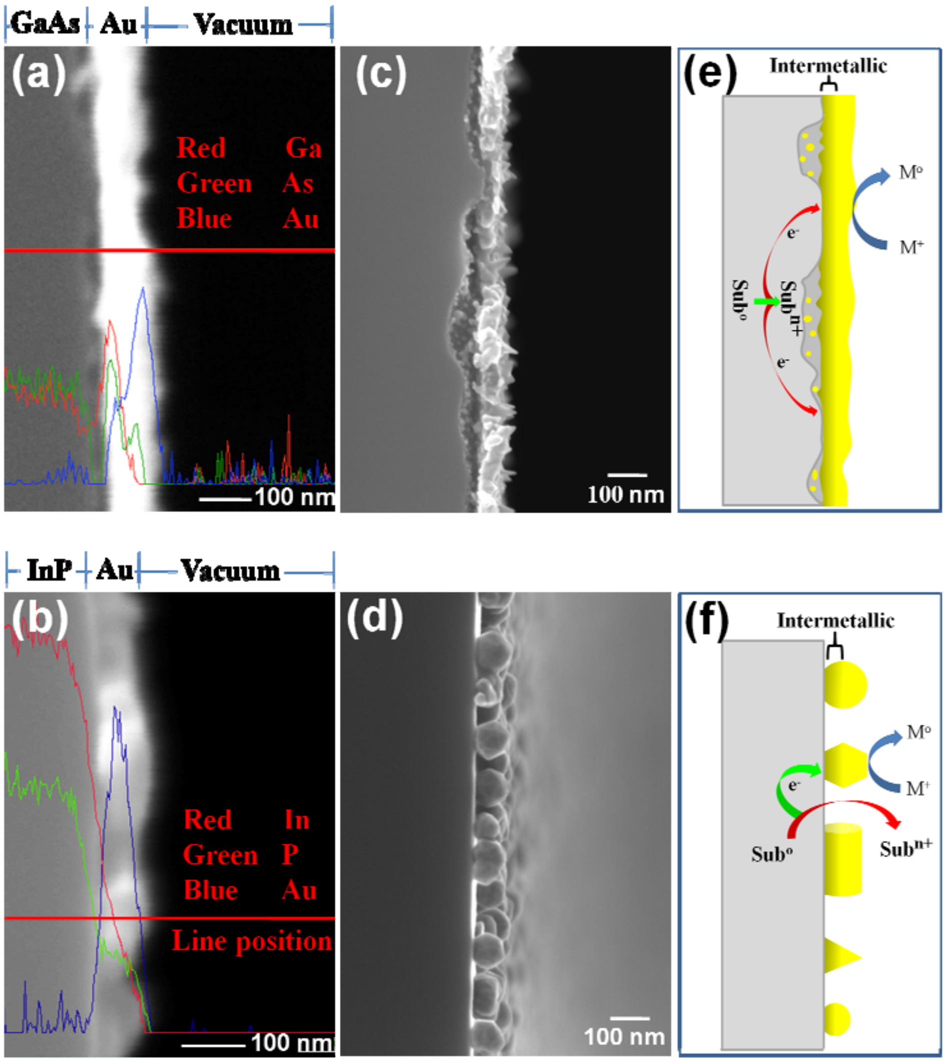

Figure 2.12. *Scanning Auger electron line profile spectra of Au on GaAs(100) (a) and InP(100) (b). Both (a) and (b) are superimposed on the SEM images taken with the scanning Auger microscope. (c-d) Cross-sectional SEM images of Au on GaAs(100), and Au on InP(100), respectively. Schematic diagrams (e-f) show the apparent diffusion (darker yellow area) of the substrate components through the gold film.*[24]

In both systems, as can be seen from the scanning Auger line profiles, there is no gold signal within the GaAs and InP substrates, whereas some semiconductor signal (Ga, As, In, P) is apparent within the gold layer. While it may be that some portion of the semiconductor signal within the gold layer is due to tenaciously bound oxides, in spite of repeated rinsing, it does suggest that metal diffusion into the semiconductor lattice is insignificant. The existence of interfacial gold alloys may account for the insignificant gold diffusion into the substrate lattice (*vide supra*). Based on the scanning Auger microscopic (SAM) data, depth profile XPS data and previous literature suggestions,[22, 41] schematic diagrams of the galvanic displacement and resulting structures are proposed in Figures 2.12e-f. An abrupt intermetallic boundary with the semiconductor is believed to be present, and some degree of diffusion of the semiconductor elements into the overlying gold leads to a possible gradient within the metal overlayer. As for the location of etching and resulting roughness, InP and GaAs show some obvious differences, as portrayed schematically in Figures 2.12e-f. Injected holes are consumed by the oxidation of the semiconductor surface so that the substrate is replaced by metal atoms (displacement mechanism). Continued displacement reactions and growth of metal could result in the formation of pitted locations neighboring the metal deposition sites, or in more remote locations.[42] In the case of GaAs, local etching appears to predominate, and there is substantial pitting observed underneath the metal deposits whereas with InP, the smooth interface suggests remote etching.

2.2.2. Ag on InP(100) and GaAs(100)

Immersion of samples of GaAs(100) and InP(100) in aqueous solutions of $AgNO_3$ leads to deposition of silver metal on the surface. The presence of an acid greatly increases the quantity of metal deposition for a given length of time, and the nature of the acid also plays a role in deposited metal morphology.[24] Exposure of GaAs(100) to 1 mM $AgNO_3$ (aq) for 5 min leads to patchy metal deposition, as seen in Figure 2.13a, whereas with the addition of 1% HF (aq), more regular silver nanoparticles with diameters of 50-80 nm are observed (Figure 2.13b). When hydrofluoric acid was exchanged with sulfuric acid, however, a more unusual morphology is observed, with flat leaf-like dendritic patterns extending over 20 microns from the central point, interspersed with vertical nanoparticles structures (Figure 2.13c-d). As shown by AFM, the heights of the leaves are about 50 nm and the interspersed taller nanoparticles structures are about 190 nm. A selected area electron diffraction (SAED) pattern (Figure 2.13g) of the silver structure is obtained from the circled area in Figure 2.13f indicates that the area observed is single crystalline Ag. Scanning Auger microscopy (SAM) was utilized to obtain compositional maps of the surface, and reveal that the leaf-like structures are indeed silver (Figure 2.14). Comparing silver leaf-like and nanoparticle structures observed on GaAs *via* galvanic displacement process from H_2SO_4 and HF containing solutions, respectively, indicate the role of the counter anions and particularly SO_4^{2-} ions in resulting in a directed growth of silver structures. The directed growth mechanism is expected to involve the adsorption of the SO_4^{2-} ions on the exposed top surfaces of the nucleated silver allowing for subsequent concentric growth and the formation of the leaf-like silver structures.

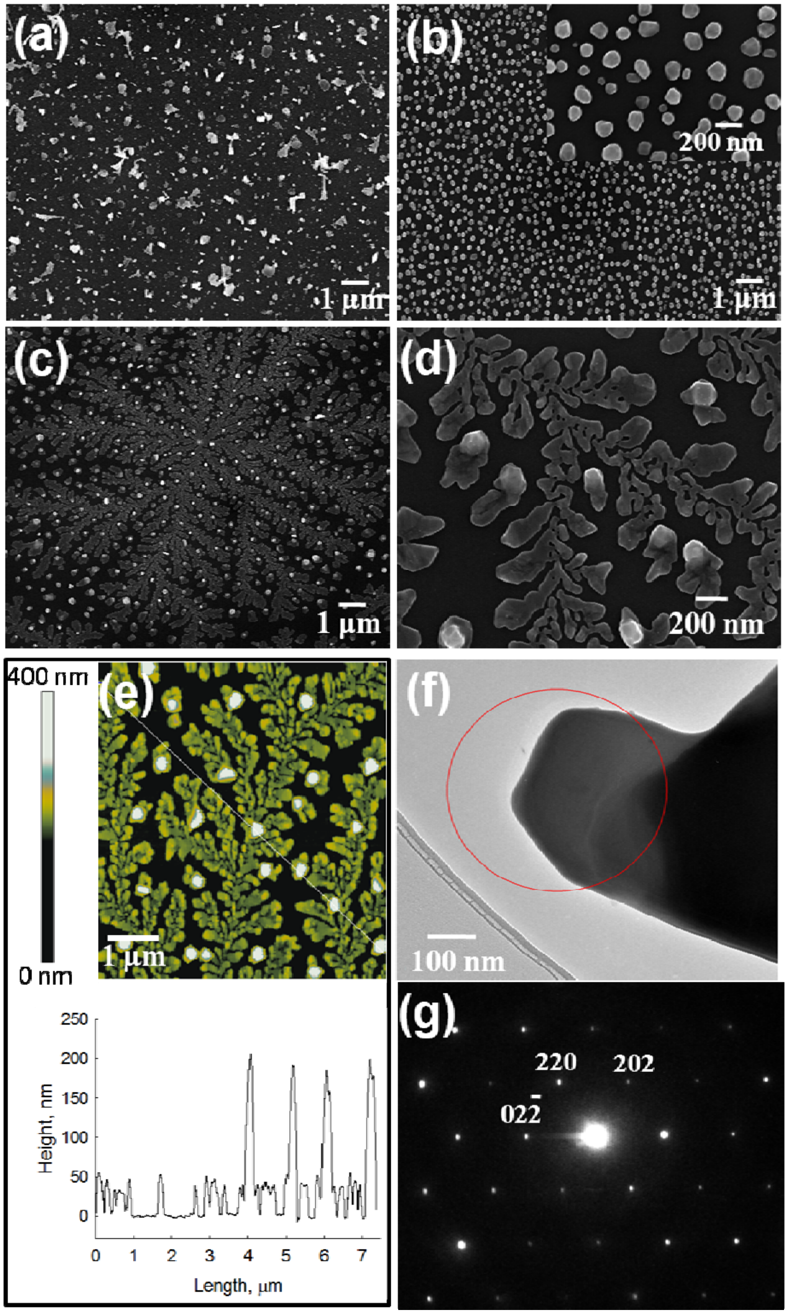

Figure 2.13. *(a-d) SEM images of silver nanostructures on GaAs(100). Deposition was carried out for 5 min from (a) 1 mM* $AgNO_3$ *(aq), (b) 1 mM* $AgNO_3$ *(aq) and 1% HF (aq). (c-d) 1 mM* $AgNO_3$ *and 2%* H_2SO_4 *(aq). (e) AFM image of Ag, on GaAs(100), formed under the same conditions for (d). (f) TEM image of silver structures grown by immersing of GaAs(100) in 1 mM* $AgNO_3$ *and 2%* H_2SO_4 *(aq) for 48 h. (g) SAED image of the selected area in image (f).*[24]

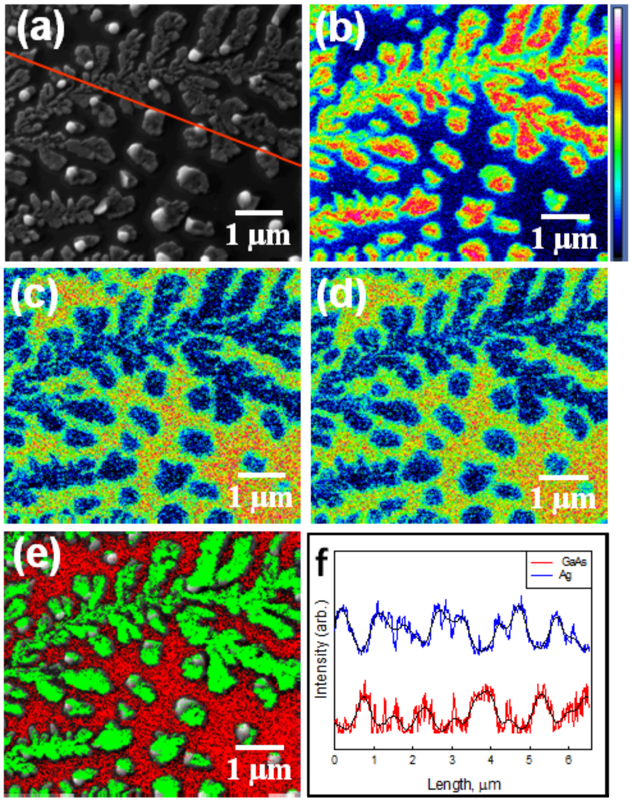

Figure 2.14. *Scanning Auger microscopy (SAM) of silver nanostructures on GaAs(100). (a) SEM image. (b) Ag MNN SAM. (c) Ga LMM SAM. (d) As LMM SAM. (e) Superimposition of Ag MNN (green) over Ga LMM (red). (f) SAM line profiles of Ag MNN, S LMM, and GaAs LMM. The line position is shown in red in the SEM image (a). The deposition was carried out from 1 mM* $AgNO_3$ *and 2%* H_2SO_4 *(aq).*[24]

Figure 2.15 shows the Ag 3d XPS depth profile spectra of the Ag nanostructures on GaAs(100), formed by immersion in 1 mM $AgNO_3$ and 2% H_2SO_4 for 5 min. At 0 min sputtering, the Ag $3d_{5/2}$ peak at 368.20 eV is visible, and corresponds to metallic Ag.[43] After 98 min, all the silver is removed. Following an intermediate length of time of 38 min sputtering, the initial peak appears to shift only a very small amount, ~ 0.5 eV to higher binding energy, to 368.67 eV.

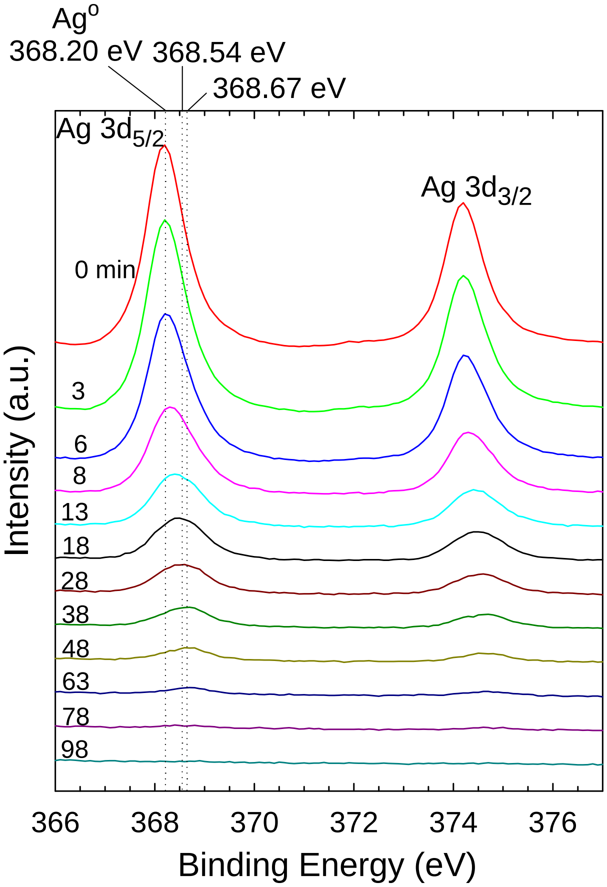

Figure 2.15. *Ag $3d_{5/2}$ XPS spectra of Ag on GaAs(100), formed by immersion in 1 mM $AgNO_3$ and 2% H_2SO_4 (aq), at different Ar^+ sputtering time intervals.*[24]

To the best of our knowledge, an Ag/GaAs intermetallic had not been observed by XPS or any other means, and thus we cannot conclude that this small shift in binding energy is meaningful in pointing towards the existence of interfacial intermetallic involving silver.[24] It is worth noting that small shifts in XPS could be due to a variety of factors, including final state effects in as-prepared metallic nanostructures, and others.[44] XPS depth profile spectra for Ga $3d_{5/2}$ and As 3d at different sputtering times (Figure 2.16) show only evidence for etching surface oxides at the beginning of sputtering followed with no peak shift during the sputtering course.

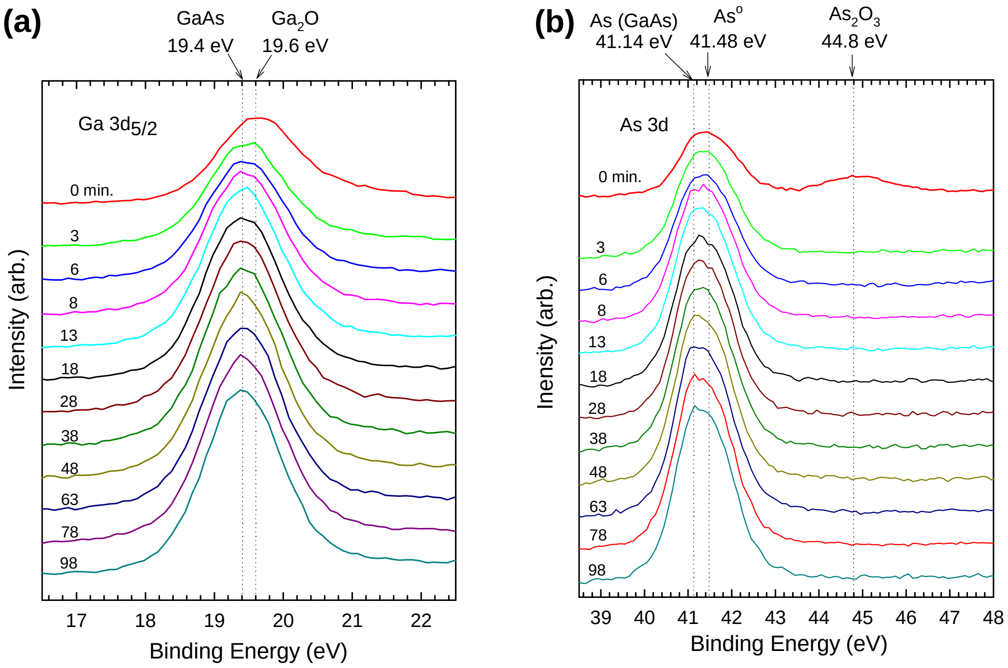

Figure 2.16. *(a) Ga $3d_{5/2}$ XPS spectra of Ag on GaAs(100), and (b) As 3d XPS spectra of Ag on GaAs(100) after Ar^+ sputtering at different time intervals.*[24]

On InP(100), a variety of different silver structures are formed upon immersion in 1 mM $AgNO_3$ (aq), depending upon the additive. As shown in Figure 2.17a, in the absence of an acid, negligible deposition occurs. In the presence of 1% HF (aq), large (300 nm) silver particles are seen, while with 2% H_2SO_4 (aq), large silver structures are formed (Figures 2.17b-f).[24, 42] The Ag 3d XPS depth profile spectra of the silver nanostructures on InP(100), formed by immersion in 1 mM $AgNO_3$ and 2% H_2SO_4 for 5 min shows only a peak at 368.2 eV (Ag^o), before sputtering (Figure 2.18). With further sputtering, no shift in the peak position is observed up until complete disappearance of silver, after 110 min sputtering.

The In $3d_{5/2}$ depth profile XPS spectra at increasing sputtering times shows only the expected components such as InP (443.98 eV)[45] and In_2O_3 (444.71 eV)[46] (Figure 2.19). Again, there is no noticeable peak shift right up to the point where the silver is completely removed (200 minutes). As in the case of GaAs and silver, intermetallics between silver and InP are not known; because of the lack of comparative intermetallic data and no apparent XPS shift, no conclusion can be reached as to the existence of an Ag/InP intermetallic layer.

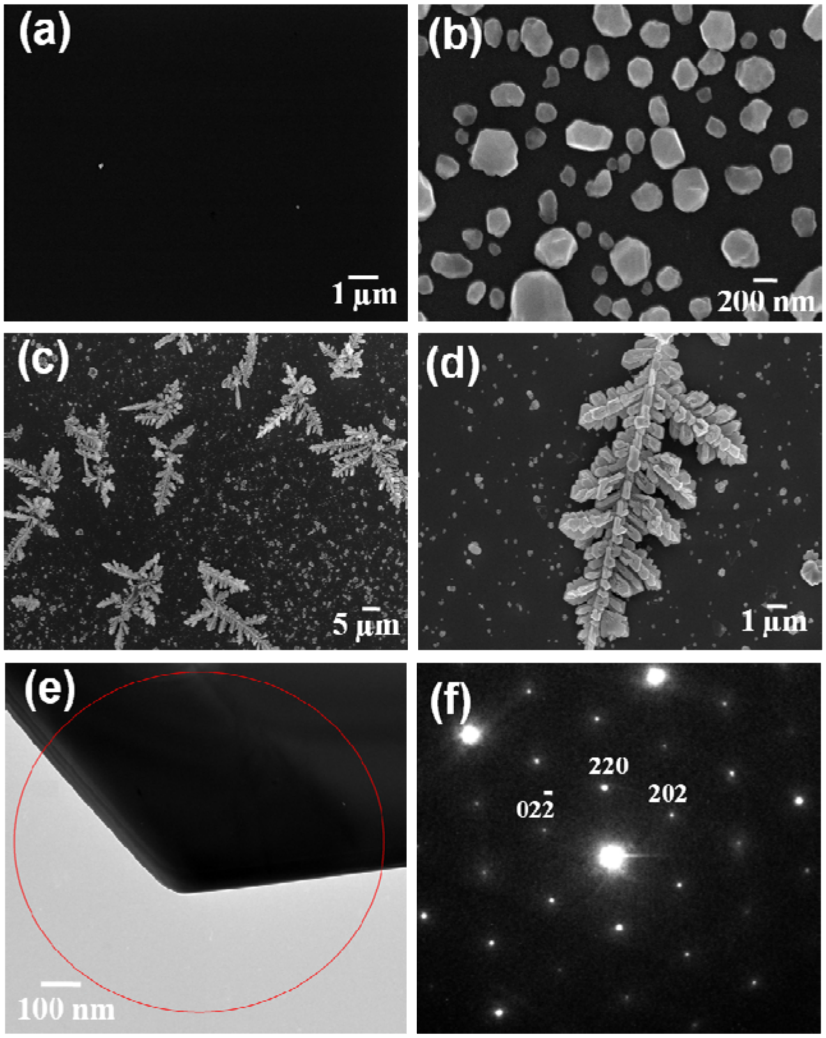

Figure 2.17. *SEM images of Ag nanoparticles formed on InP(100) formed by immersion in (a) 1 mM* $AgNO_3$ *(aq) for 30 min. (b) 1 mM* $AgNO_3$ *and 1% HF for 30 min. (c-d) 1 mM* $AgNO_3$ *and 2%* H_2SO_4 *(aq) for 30 min. (e) TEM image of silver structures grown by immersing of InP(100) in 1 mM* $AgNO_3$ *and 2%* H_2SO_4 *(aq) for 48 h. (f) SAED image of the selected area in image (e).*[24]

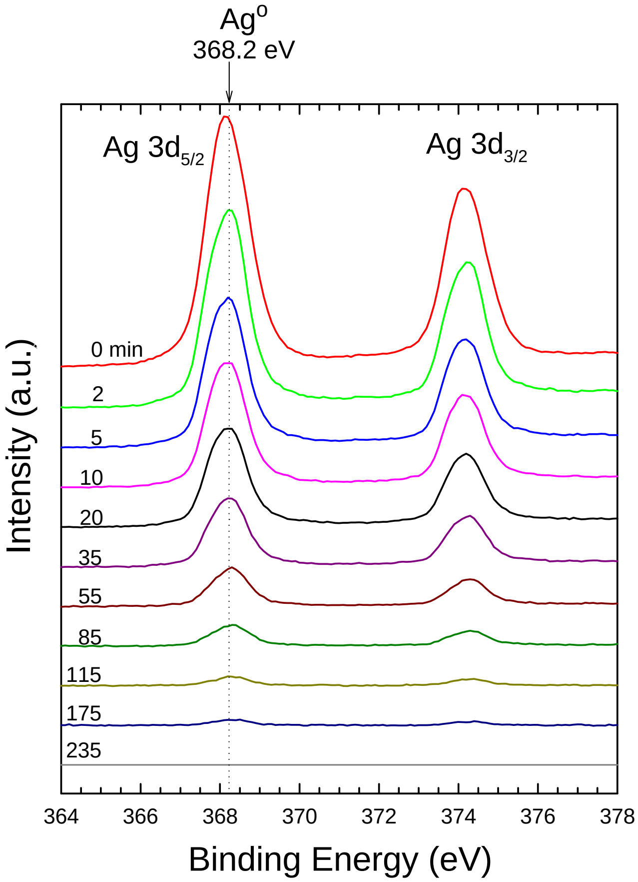

Figure 2.18. *Ag 3d XPS spectra of Ag on InP(100), formed by immersion in 1 mM $AgNO_3$ and 2% H_2SO_4 (aq) for 5 min, at different Ar^+ sputtering time intervals.*[24]

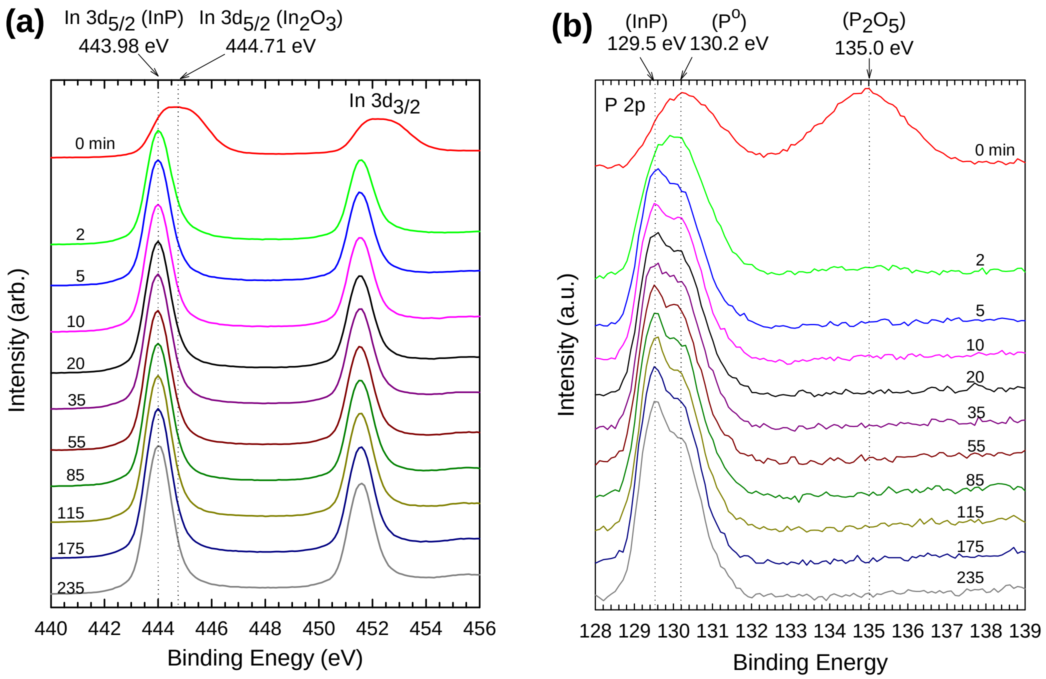

Figure 2.19. *(a) In $3d_{5/2}$ XPS spectra of Ag on InP(100), and (b) P $2p_{3/2}$ XPS spectra of Ag on InP(100) after Ar^+ sputtering at different time intervals.*[24]

Cross section scanning Auger electron line profiles (SAM, Figure 2.20) differ somewhat from the gold on GaAs and InP systems (*vide infra*). The signal for silver does not appear as abrupt at the semiconductor-silver interface as it did for the situation with gold. While there is no evidence whatsoever for an intermetallic with silver, the SAM may be suggestive of some diffusion of silver into the bulk GaAs and InP, although this remains to be verified by other means.

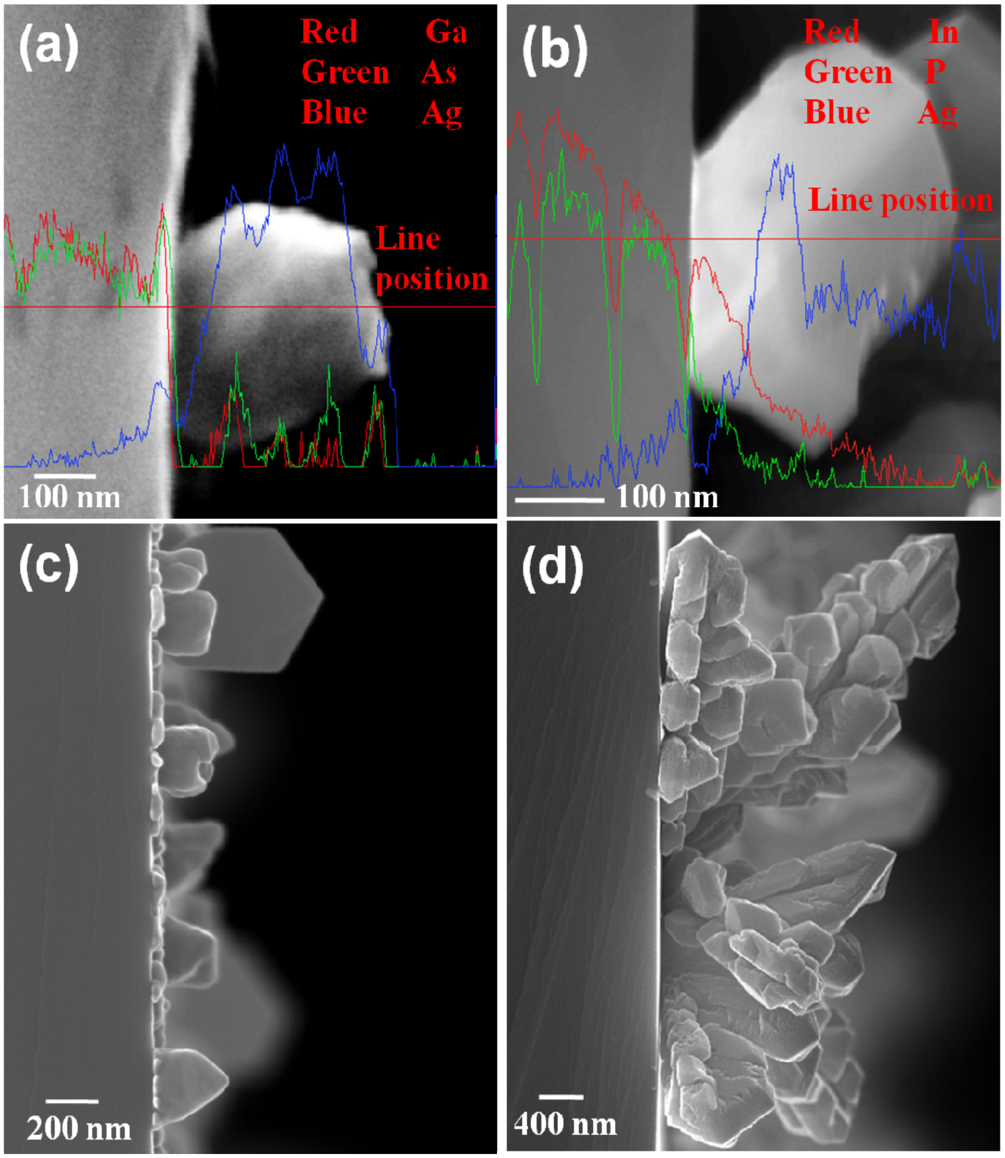

Figure 2.20. *(a) Scanning Auger electron line profile spectra of Ag on GaAs(100). (b) Scanning Auger electron line profile spectra of Ag on InP(100). Both (a) and (b) are superimposed on the SEM images taken with the scanning Auger microscope. (c-d) Cross section SEM images of Au on GaAs(100), and Au on InP(100), respectively.*[24]

2.3. Conclusions

This chapter described an investigation of the nature of the interface formed between the metals (gold and silver), and the technologically relevant semiconductor substrates, InP and GaAs, produced *via* room temperature galvanic displacement. Interfacial characterization was performed *via* XPS depth profile analyses. Cross-sectional scanning Auger electron line profile spectra assisted in the investigation of the diffusion of metals into the semiconductor lattice and vice versa.

Immersion of these III-V semiconducting materials in a solution of the ionic gold and silver precursors results in deposition of firmly bound metal on the surface with varying morphologies, depending upon the conditions. Depth profile XPS indicates the presence of an intermetallic layer sandwiched between gold on GaAs and InP. The intermetallic may be a combination of two different compositions, as suggested by deconvolution of the XPS spectra at intermediate stages of profiling. A more Ga- or In-rich intermetallic is located closer to the bulk semiconductor, and is covered by a more metal-rich alloy in contact with the overlying metal deposit. The compositions of the gold intermetallics for GaAs and InP are most likely γ-Au_9Ga_4 and AuGa, and AuIn and $AuIn_2$, respectively.

Cross section scanning Auger electron line profile spectra suggest little diffusion of the metals into the semiconductor lattice. It appears, therefore, that in the case of gold on InP and GaAs, dissociative diffusion of the semiconductor into the metal is favored, leading to a structure in which the intermetallic is located at an abrupt semiconductor-intermetallic boundary. In the case of silver on GaAs and InP, no evidence can be gleaned to support the presence of an intermetallic layer.

2.4. Experimental Section

Generalities:

InP (100) n-type, s doped, wafers (resistivity = 0.001 Ω•cm) were purchased from AXT Inc. $KAuCl_4 \cdot xH_2O$ and $AgNO_3$ were purchased from Strem Chemicals. All experiments were carried out under standard ambient laboratory illumination. The semiconductor wafers were cut into 1x1 cm^2 shards and were sonicated first in acetone and subsequently in methanol, each for ten minutes. The substrates were then dried using a nitrogen stream. The InP wafer shards were placed in 100 ml of 1:1 49 % HF (aq) and 18 MΩ (Barnstead) water for 10 min. The wafer shards were subsequently rinsed *via* dipping for 2 min each into five beakers containing 18 MΩ water and then dried with a N_2 stream. GaAs (100) n-type, Si doped, wafers (resistivity = 0.001 Ω•cm) were purchased from AXT, Inc. The GaAs (100) wafer shards, 1x1 cm^2, were sonicated in acetone and methanol for 10 min each and dried using a nitrogen stream. The GaAs wafer shards were placed in a H_2SO_4:H_2O_2:H_2O (4:1:100) solution for 10 min then HCl:H_2O (1:3) for 2 min and 18 MΩ water for 10 min. The shards were then dipped for 2 min each into five beakers containing 18 MΩ water and then dried with an N_2 stream.

Surface Characterization:

The metallic nanostructures were characterized by atomic force microscopy (AFM), scanning electron microscopy (SEM), transmission electron microscopy (TEM), scanning Auger microcopy (SAM), and X-ray photoelectron spectroscopy (XPS). SEM, SAM, and XPS were performed under high-vacuum conditions ($<10^{-8}$ Torr). The atomic force microscope used in this study was a Nanoscope IV (Digital Instruments/Veeco) using commercially available Si cantilevers in tapping mode under ambient conditions.

SEM (Hitachi S-4800 FE-SEM) of metal nanostructures was typically performed with electron energy of 20 keV. Auger measurements were carried out using JAMP-9500F Auger microscope (JEOL). The accelerating voltage and the emission current for both the SEM and Auger imaging were 15 KV and 8 nA, respectively. The sample was rotated 30 degrees away from the primary electron beam to face the electron energy analyzer. An M5 lens with 0.6 % energy resolution was used for the Auger spectroscopy and imaging. The Auger peaks of Ag M4N45N45 (350 eV) and Au M5N67N67 (2015 eV) were selected for the mapping. The Auger mapping for each element was obtained by plotting (P - B)/B, where P and B are peak and background intensities, respectively. The intensities were then scaled using the JEOL processing software for increased contrast. The average escape depth for Ag MNN electrons from GaAs is estimated to be 0.7 nm according to the NIST IMFP database.

XPS (Kratos Analytical, Axis- Ultra) was performed using monochromatic Al KR with a photon energy of 1486.6 eV. The pressure in the XPS chamber was ~8 x 10^{-10} Torr at time of measurement. For sputtering, 5 keV Ar^+ ions were used with a beam current of 0.9 μA on the sample. The average escape depths for Au 4f and Ag 3d electrons from GaAs are estimated to be 2.1 and 1.7 nm, respectively, and those from InP are estimated to be 2.4 and 2.0 nm, respectively, according to the NIST IMFP database. The data were calibrated on the basis of the C 1s peak. The Ag 3d and Au 4f metallic positions were also calibrated using sputtered Ag and Au films, respectively. For the investigation in this study, only the Au $4f_{7/2}$ emission line at the lower binding energy (BE), but higher intensity, has been considered. Before fitting the data, a Shirley background was calculated and subtracted from the original spectra. The spectra were analyzed using non-linear least square fitting procedures (CASA software), which follows the guidelines outlined by Joyce *et al.*[47] The Au $4f_{7/2}$ spectra were fitted into several components consisting of the spin-orbit-split Voigt functions.

X-ray diffraction was performed on a Bruker D8 Discover instrument equipped with a sealed Cu tube. Glancing incidence diffraction (GIXRD) analyses were performed in this work. All GIXRD patterns were collected with an incident angle $\omega = 3^{\circ}$. The peaks in the X-ray diffraction pattern were identified in terms of the Bragg angle, 2θ.

TEM images and electron diffraction patterns were recorded on a 200 kV JEOL 2200FS TEM/STEM instrument. For TEM sample preparation GaAs(100) and InP(100) were immersed in 10 ml of 1 mM $AgNO_3$ and 2% H_2SO_4 (aq) for 48 h. Silver structures growing out from the substrate were then transferred in a vial containing 100% ethanol and a drop of the resultant solution was placed on carbon grid to be characterized.

2.5. References

(1) Sze, S. M. *Physics of Semiconductor Devices* Wiley: New York, 1981.

(2) Sze., S. M. *Semiconductor Devices, Physics and Technology*; Wiley: New York 1985.

(3) Lee, Y. C.; Park, C. S. *Microwave and Optical Technology Letters* **2007**, *49*, 575-578.

(4) Lin, Y. S.; Chen, B. Y.; Ho, C. H. *Journal of the Electrochemical Society* **2007**, *154*, H951-H956.

(5) Liu, T. A.; Lin, G. R.; Chang, Y. C.; Pan, C. L. *Optics Express* **2005**, *13*, 10416-10423.

(6) Salehi, A.; Kalantari, D. J. *Sensors and Actuators B-Chemical* **2007**, *122*, 69-74.

(7) Gol'dberg, Y. A.; Nasledov, D. N.; Tsarenkov, B. V. *Pribory i Tekhnika Eksperimenta* **1971**, *3*, 207.

(8) Donzelli, G. P.; Guarini, G.; Vidimari, F. *Thin Solid Films* **1978**, *55*, 25-33.

(9) Sun, Y. G.; Yan, H. F.; Wiederrecht, G. P. *Journal of Physical Chemistry C* **2008**, *112*, 8928-8938.

(10) Sun, Y. G.; Wiederrecht, G. P. *Small* **2007**, *3*, 1964-1975.

(11) Nezhad, M. R. H.; Aizawa, M.; Porter, L. A.; Ribbe, A. E.; Buriak, J. M. *Small* **2005**, *1*, 1076-1081.

(12) Piotrowska, A.; Auvray, P.; Guivarc'H, A.; Pelous, G.; Henoc, P. *Journal of Applied Physics* **1981**, *52*, 5112-5117.

(13) Wada, O. *Journal of Applied Physics* **1985**, *57*, 1901-1909.

(14) Szydlo, N.; Olivier, J. *Journal of Applied Physics* **1979**, *50*, 1445-1449.

(15) Shunk, F. A. *Constitution of Binary Alloys, Second Supplement*; McGraw-Hill: New York, 1969.

(16) Fatemi, N. S.; Weizer, V. G. *Journal of Applied Physics* **1989**, *65*, 2111-2115.

(17) Fatemi, N. S.; Weizer, V. G. *Journal of Applied Physics* **1990**, *67*, 1934-1939.

(18) Weizer, V. G.; Fatemi, N. S. *Journal of Applied Physics* **1988**, *64*, 4618-4623.

(19) Holloway, P. H.; Mueller, C. H. *Thin Solid Films* **1992**, *221*, 254-261.

(20) Bauer, C. L. *Surface Science* **1986**, *168*, 395-403.

(21) Plante, M. C.; Garrett, J.; Ghosh, S. C.; Kruse, P.; Schriemer, H.; Hall, T.; LaPierre, R. R. *Applied Surface Science* **2006**, *253*, 2348-2354.

(22) Hiraki, A.; Shuto, K.; Kim, S.; Kammura, W.; Iwami, M. *Applied Physics Letters* **1977**, *31*, 611-612.

(23) Magagnin, L.; Maboudian, R.; Carraro, C. *Journal of Physical Chemistry B* **2002**, *106*, 401-407.

(24) Sayed, S. Y.; Daly, B.; Buriak, J. M. *Journal of Physical Chemistry C* **2008**, *112*, 12291-12298.

(25) Sayed, S. Y.; Wang, F.; Mallac, M.; Meldrum, A.; Egerton, R. F.; Buriak, J. M. *ACS Nano* **2009**, *3*, 2809-2817.

(26) Srinivasan, R.; Suni, II *Surface Science* **1998**, *408*, L698-L702.

(27) Warren, S.; Reitzle, A.; Kazimirov, A.; Ziegler, J. C.; Bunk, O.; Cao, L. X.; Renner, F. U.; Kolb, D. M.; Bedzyk, M. J.; Zegenhagen, J. *Surface Science* **2002**, *496*, 287-298.

(28) Rossiter, C.; Suni, II *Surface Science* **1999**, *430*, L553-L557.

(29) Porter, L. A.; Choi, H. C.; Ribbe, A. E.; Buriak, J. M. *Nano Letters* **2002**, *2*, 1067-1071.

(30) Hou, T.; Greenlief, M.; Keller, S. W.; Nelen, L.; Kauffman, J. F. *Chemistry of Materials* **1997**, *9*, 3181-3186.

(31) Kirchner, C.; George, M.; Stein, B.; Parak, W. J.; Gaub, H. E.; Seitz, M. *Advanced Functional Materials* **2002**, *12*, 266-276.

(32) Traub, M. C.; Biteen, J. S.; Brunschwig, B. S.; Lewis, N. S. *Journal of the American Chemical Society* **2008**, *130*, 955-964.

(33) Seah, M. P.; Smith, G. C.; Anthony, M. T. *Surface and Interface Analysis* **1990**, *15*, 293-308.

(34) Jayne, D. T.; Fatemi, N. S.; Weizer, V. G. *Journal of Vacuum Science & Technology A-Vacuum Surfaces and Films* **1992**, *10*, 2802-2805.

(35) Contour, J. P.; Massies, J.; Saletes, A. *Japanese Journal of Applied Physics Part 2-Letters* **1985**, *24*, L563-L565.

(36) Traub, M. C.; Biteen, J. S.; Michalak, D. J.; Webb, L. J.; Brunschwig, B. S.; Lewis, N. S. *Journal of Physical Chemistry B* **2006**, *110*, 15641-15644.

(37) Surdu-Bob, C. C.; Saied, S. O.; Sullivan, J. L. *Applied Surface Science* **2001**, *183*, 126-136.

(38) Persson, A. I.; Larsson, M. W.; Stenstrom, S.; Ohlsson, B. J.; Samuelson, L.; Wallenberg, L. R. *Nature Materials* **2004**, *3*, 677-681.

(39) Hansen, M. *Constitution of Binary Alloys, 2nd ed*; McGraw Hill: New York, 1958.

(40) Jayne, D. T.; Fatemi, N. S.; Weizer, V. G. *Journal of Vacuum Science & Technology A-Vacuum Surfaces and Films* **1991**, *9*, 1410-1415.

(41) Hiraki, A.; Kim, S.; Kammura, W.; Iwami, M. *Surface Science* **1979**, *86*, 706-710.

(42) Aizawa, M.; Cooper, A. M.; Malac, M.; Buriak, J. M. *Nano Letters* **2005,** *5*, 815-819.

(43) Aizawa, M.; Buriak, J. M. *Journal of the American Chemical Society* **2006**, *128*, 5877-5886.

(44) Cuenya, B. R.; Baeck, S. H.; Jaramillo, T. F.; McFarland, E. W. *Journal of the American Chemical Society* **2003**, *125*, 12928-12934.

(45) Mizokawa, Y.; Iwasaki, H.; Nishitani, R.; Nakamura, S. *Journal of Electron Spectroscopy and Related Phenomena* **1978**, *14*, 129-141.

(46) Faur, M.; Faur, M.; Jayne, D. T.; Goradia, M.; Goradia, C. *Surface and Interface Analysis* **1990**, *15*, 641-650.

(47) Joyce, J. J.; Delgiudice, M.; Weaver, J. H. *Journal of Electron Spectroscopy and Related Phenomena* **1989**, *49*, 31-45.

Chapter 3

Heteroepitaxial Growth of Gold Nanostructures on Silicon by Galvanic Displacement

3.1. Introduction

Galvanic displacement has seen application in a number of different areas, particularly those related to the construction of nanoscale metallic and semiconductor architectures. For instance, Carraro and co-workers used galvanic displacement to produce gold nanoparticle catalyst arrays in silicon trenches for the synthesis of horizontally suspended silicon nanowires (NWs).[1] Gösele and co-workers demonstrated that gold nanoparticles on silicon surfaces, prepared *via* galvanic displacement, resulted in the growth of a high quantity of epitaxial Si nanowires with neat and sharp crystallographic interfaces whereas evaporated gold films led to low amounts of epitaxial nanowires, with defects at the silicon nanowire-bulk silicon interface.[2, 3] The group of Kamins and co-workers from Hewlett Packard (HP) demonstrated galvanic displacement directly on silicon nanowires to produce gold nanoparticle-decorated silicon nanostructures.[4] Galvanic displacement has also been found to be amenable to nanoscale patterning *via* self-assembled block copolymer templates, reverse micelle deposition on surfaces, and Dip Pen Nanolithography (DPN) to produce, in a controlled manner, metallic nanostructures on a variety of different semiconductor interfaces.[1, 5-7] In a completely unrelated application, galvanic displacement of silver nanoparticles on silicon can be used to etch silicon nanowire arrays in a wet chemical fashion.[8]

Silicon has been extensively involved in IC systems and modern electronics and served as the foundation for the multibillion-dollar electronic industry.[9-13] Although, gold-on-silicon nanostructures, prepared by galvanic displacement, have been used in the fabrication of many device architectures, the Au-Si interface is not well understood, and is the source of much interest. A detailed understanding of the nature and the structure of the gold-silicon interface as prepared by galvanic displacement, and the subsequent growth mode of the gold nanostructures merits detailed consideration not only from a technological perspective, but also to elucidate fundamentals in interfacial nanoscience.[1, 6, 14, 15] In terms of galvanic displacement of metals on semiconductors, a number of basic questions remain that do not yet allow for a convergent set of conclusions to be made as to the nature of these interfaces. For instance in the case of gold on silicon, XPS depth profiling clearly indicates evidence for the existence of undefined interfacial gold-silicon intermetallics (see chapter 1).[16] Whereas synchrotron surface X-ray diffraction studies point to heteroepitaxial growth of few gold-monolayers on silicon, as indicated from the q scan measurements, showing a diffraction from gold (111) planes parallel to Si(111) substrate (Figure 3.1.).[17]

The heteroepitaxial growth of two materials of lattice mismatch lower than 15% is not surprising.[18] However, for a 25% lattice mismatched gold-silicon system, heterepitaxial behaviour needs to be understood. Moreover, the relationship or connection between the presence of intermetallics and heteroepitaxy is difficult to envisage. In addition to questions regarding the growth mechanism of metallic nanoparticles on semiconductors *via* galvanic displacement, both Volmer-Weber[17, 19-21] and Stranski-Krastanov modes[22] of growth have been suggested. In order to attempt to answer some of these questions, we harnessed the precision of transmission electron microscopy (TEM) nanobeam diffraction analyses to characterize, in detail, the nature of gold-silicon interfaces formed *via* galvanic displacement on flat single crystal Si(111) and Si(100) surfaces, and silicon nanowires.

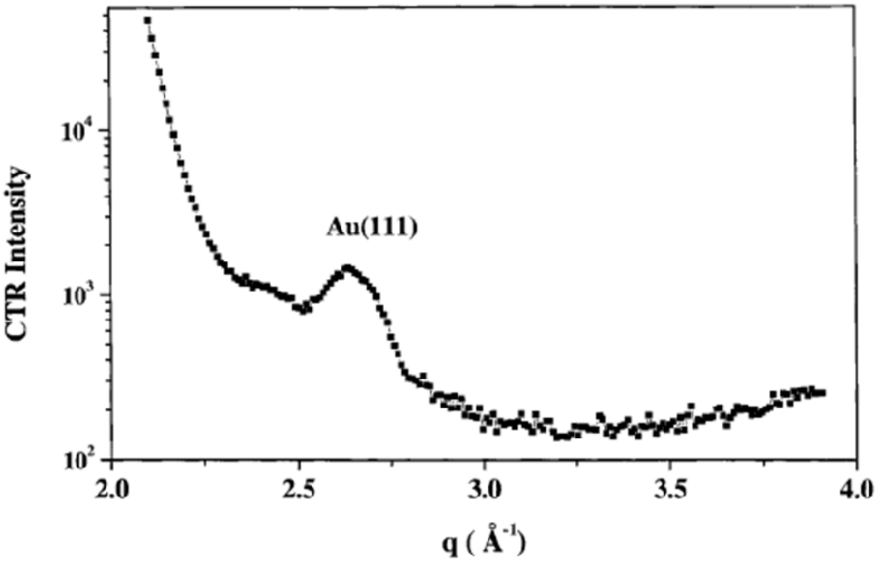

Fugure 3.1. *Specular q scan of Si substrate after deposition of 1.9 monolayer (ML) gold by galvanic displacement method.*[17] *Where* $q = (4\pi/\lambda)\ \sin\theta$.[23] *Copyright © 2002 Elsevier. Reproduced with permission from ref. 17.*

3.2. Results and Discussions

The synthesis of gold nanostructures on silicon surfaces was carried out through immersion of the semiconductor wafer in a solution of metal ions with a sufficiently high oxidation potential; this reaction, galvanic displacement, occurs spontaneously as outlined in Figure 3.2. The reaction is essentially a corrosion reaction in conjunction with metal deposition - the semiconductor acts as a source of electrons that reduce the metal ions in solution to M(0) on the surface, while surface atoms are oxidized and solubilized either locally and/or distally, from an exposed surface.[24-26]

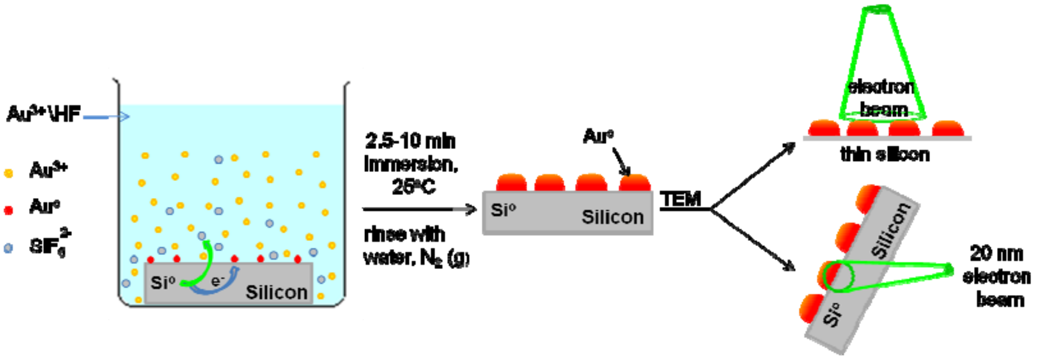

Figure 3.2. *A silicon substrate is immersed in a mixture of a gold salt, [$KAuCl_4$ (aq)], and HF (aq) at room temperature. Galvanic displacement occurs when the semiconductor surface acts as the electron source for the reduction of the metal salt. HF (aq) is required to ensure the formation of soluble SiF_6^{2-} (aq) and related species from the resulting oxidized silicon to allow for continued electron transfer. Transmission electron microscope (TEM) investigations were then carried out on backside thinned planar and cross sectioned samples.*[27]

In the case of silicon, hydrofluoric acid is required to ensure continuous metallic growth since the spontaneously formed silicon oxide product is a dielectric, and would prevent further metal ion reduction. The silicon oxide layer is dissolved *in-situ* to form soluble SiF_6^{2-} (aq) species according to equation (1):[28]

$$Si\ (s) + 6F^-\ (aq) \rightarrow SiF_6^{2-}\ (aq) + 4e^- \qquad E^o_{SiF_6^{2-}/Si} = -1.2\ V\ vs.\ NHE \qquad (1)$$

$$AuCl_4^-\ (aq) + 3e^- \rightarrow Au^o\ (s) + 4Cl^-\ (aq) \qquad E^o_{Au^{3+}/Au^o} = 1.42\ V\ vs.\ NHE \qquad (2)$$

Figure 3.3 shows the formation of nanostructured gold films on single crystal shards of Si(111) and Si(100), and silicon nanowires, by immersion in dilute $KAuCl_4$ (aq) and HF (aq) for short periods of time (second to minutes). Longer immersion times results in greater quantities of metallic deposition on all of the studied silicon surfaces (Figure 3.3), as expected.[4, 29] In the case of Si(111), plan view (top view) SEM images (Figure 3.3 a-d) reveal that increasing the immersion time from 2.5 to 10 min resulted in changing the morphology of the grown gold deposits from islands to continuous films. However, in the case of Si(100) (Figure 3.3e-h), increasing the immersion time, up to 10 min, resulted in the formation of gold islands of larger sizes [compare (d) and (h) in Figure 3.3]. Cross-section SEM images show no appreciable difference in the thickness (ca. 20 nm) of the gold layers [formed after immersion of Si shards for 7.5 min in the reaction mixture, Figure 3.4 (a, b)]. Face centered cubic (fcc) metals such as silver, gold, and platinum have a high tendency to grow on (111) surfaces as a result of the highest close packing nature of (111) planes.[30, 31] Through detailed XRD analysis, Nason *et al*. studied the formation of epitaxial (evaporated) films on different Si surfaces and the strength of epitaxy was found to be in the order of Si(111) > Si(110)> Si(100).[30]

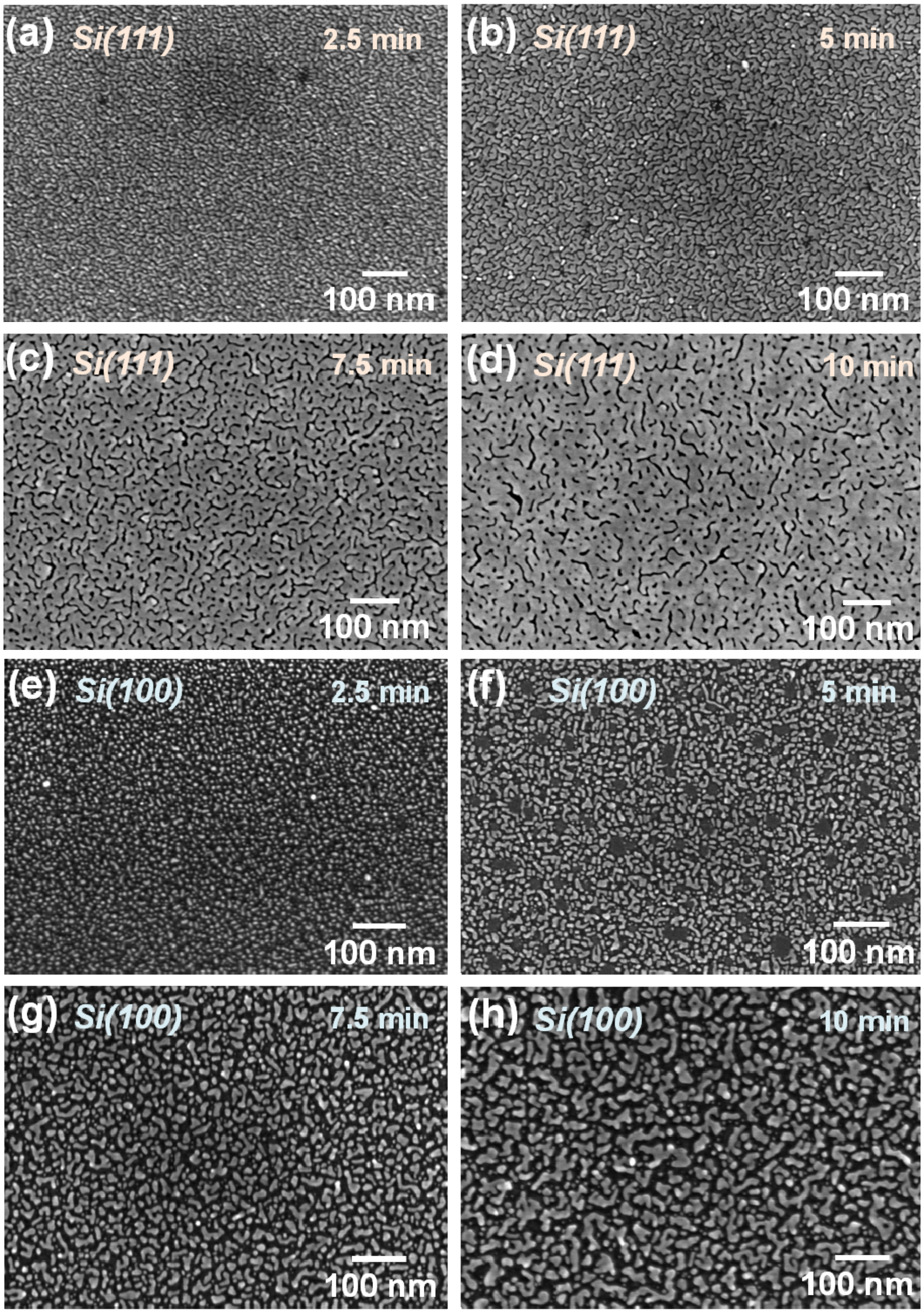
(a) Si(111) 2.5 min
100 nm
(b) Si(111) 5 min
100 nm
(c) Si(111) 7.5 min
100 nm
(d) Si(111) 10 min
100 nm
(e) Si(100) 2.5 min
100 nm
(f) Si(100) 5 min
100 nm
(g) Si(100) 7.5 min
100 nm
(h) Si(100) 10 min
100 nm

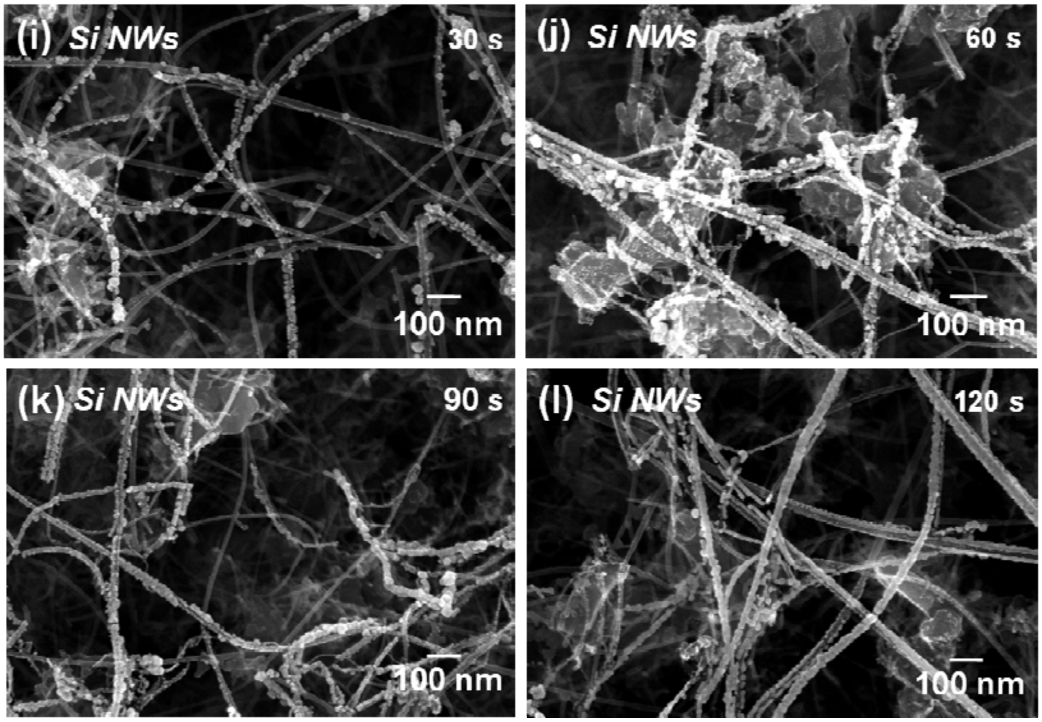

Figure 3.3. *Scanning electron micrographs (SEM) for gold nanostructures grown by galvanic displacement on different silicon surfaces such as Si(111), Si(100), and Si NWs. In the case of both Si(111) (a-d), and Si(100) (e-h), the semiconductor shards were immersed in a mixture of 0.1 mM* $KAuCl_4$ *(aq) and 1% HF (aq) for different immersion times, ranging from 2.5 – 10 min. In the case of Si NWs (i-l), the deposition bath was composed of 1 mM* $KAuCl_4$ *(aq) and 1% HF (aq), and the deposition time ranges from 30-120 s.*[27]

Silicon nanowires (NWs) were functionalized with gold nanoparticles by galvanic displacement (Figure 3.3i-l). The deposition process involved spotting of a 10 µl drop of 1 mM $KAuCl_4$ (aq) and 1% HF (aq) on the nanowire-coated substrate surface for 30-120 s. Shorter exposure times on the order of 30 s resulted in the formation of gold nanoparticles of different sizes (20-30 nm) (figure 3.4c). Further deposition of gold with increasing the exposure time resulted in the coalescence of gold deposits and formation of extended gold islands.

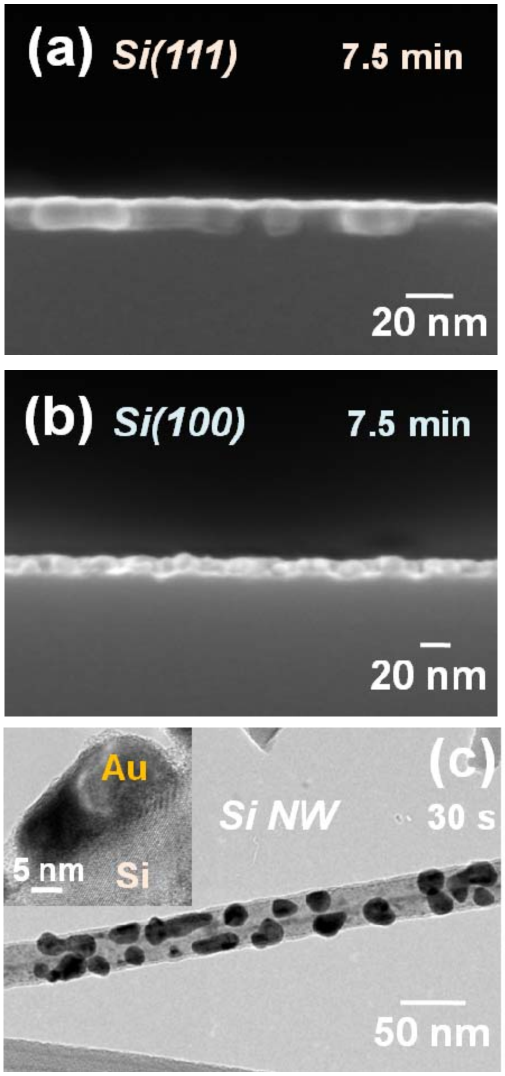

Figure 3.4. *Cross-sectional SEM images of Au films on Si(111) (a), and Si(100) (b), formed after the immersion of the Si shards in 0.1 mM* $KAuCl_4$ *(aq) and 1% HF (aq) for 7.5 min. (c) Transmission electron microscopy (TEM) image for gold nanoparticles on a silicon nanowire following removal of the Si nanowires in (Figure 3.2i, conditions: 1 mM* $KAuCl_4$ *(aq) and 1% HF (aq) for 30 s) from their substrate via sonication in 100% ethanol, followed by spotting the supernatant layer on a lacy carbon grid. The inset shows HRTEM image of a Si nanowire with a single gold nanoparticle.*[27]

3.2.1. Heteroepitaxial Growth of Gold Nanoparticles on Silicon Surfaces.

In order to characterize the structure and morphology of the gold nanoparticle layer topping the silicon, the substrates were characterized by high resolution transmission electron microscopy (HRTEM) and electron diffraction (beam size ~20-100 nm). In order to carry out TEM, the flat hydrogen-terminated silicon surfaces (500 micron-thick wafer shards) were immersed in a 0.1 mM $KAuCl_4$ (aq) and 1% HF (aq) solution for 2.5 min, and then the backside of the silicon shard was mechanically polished until the silicon was thinned to less than a micron to permit TEM imaging. Shorter immersion times were used to ensure a thin gold layer appropriate for plan view TEM (2.5 minutes versus 7.5 minutes). Figure 3.5a shows, for example, the plan view bright field (BF) TEM image for a gold nanoparticle film on a Si(111) substrate. The dark areas are the gold deposits (less transmitted intensity), whereas the lighter areas (more transmitted intensity) correspond to the silicon substrate – mass contrast. In order to investigate the orientation of the gold layer with respect to the underlying silicon planes, low and high resolution TEM images were taken along the $[\bar{1}12]$ zone axis of silicon (Figure 3.5b-c). The parallel Moiré-fringes (*vide infra*) of the gold nanoparticles on Si(111) are visible. The fringe spacing *D,* measured from the marked area in Figure 3.5b, is 9.5 Å. In order to calculate the theoretical fringe spacing, *D*, for parallel Moiré-fringes, the following equation is used,[32]

$$D = \frac{\mathrm{d}_{\mathrm{Si}\{111\}}\,\mathrm{d}_{\mathrm{Au}\{111\}}}{\mathrm{d}_{\mathrm{Si}\{111\}} - \mathrm{d}_{\mathrm{Au}\{111\}}} \tag{3}$$

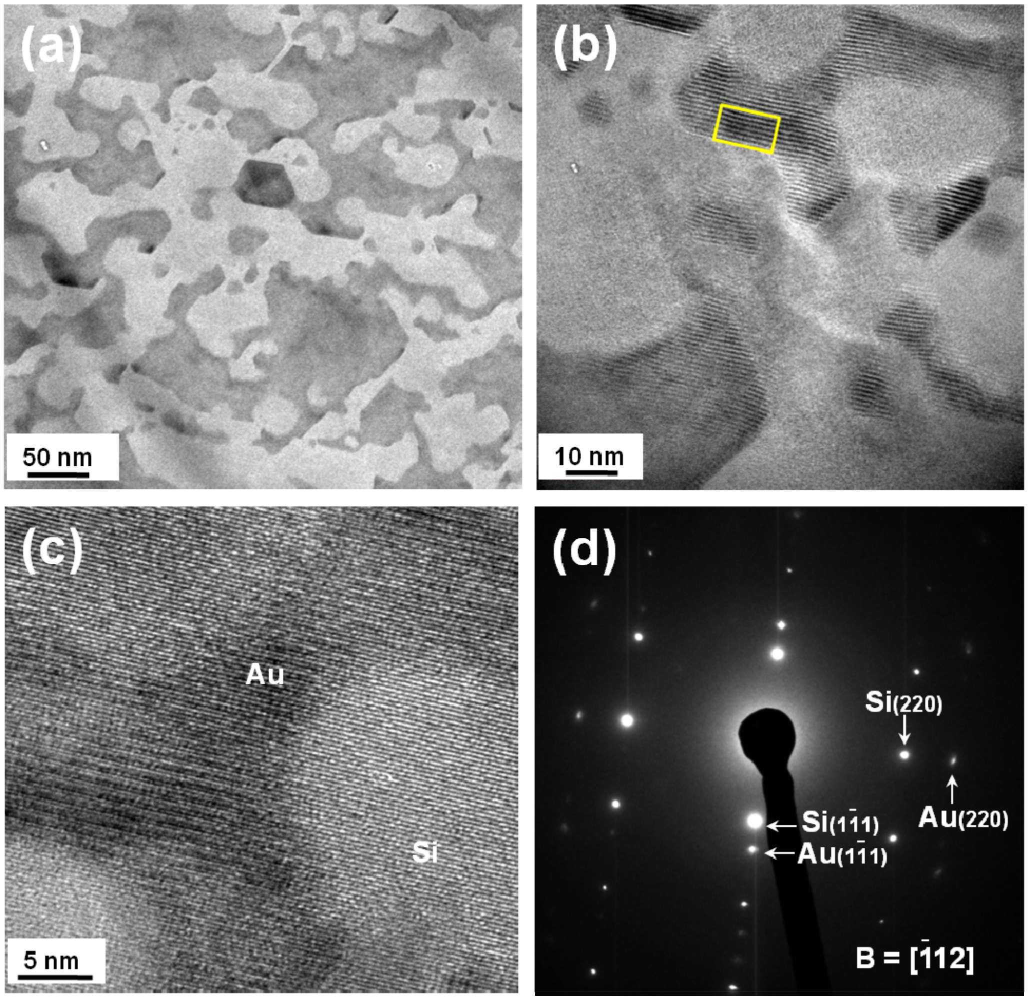

Figure 3.5. *Transmission electron micrographs for a gold film on Si(111), formed by immersing the silicon substrate in 0.1 mM* $KAuCl_4$ *(aq) and 1% HF (aq) for 2.5 min. (a) Plan view bright field (BF) TEM image. (b) and (c) HRTEM images taken close to the* $[\bar{1}12]$ *zone axis. (d) Selected area electron diffraction (SAED) pattern taken along the* $[\bar{1}12]$ *zone axis. The yellow box in image b marks the area used to calculate the fringe spacing D in equation 3.*[27]

where $d_{Si\{111\}}$ (3.134 Å) and $d_{Au\{111\}}$ (2.355 Å) are the interplanar spacings for the silicon {111} and gold {111} planes, respectively. Based on the lattice parameters of the gold and silicon {111} planes, *D* is calculated to be 9.47 Å, identical within experimental error to the observed value of 9.5 Å. Therefore, the Moiré-fringes are parallel to both the gold and silicon planes. Such alignment is suggestive of an epitaxial relationship in which a single crystalline layer of gold is oriented in a parallel manner on the single crystalline Si(111),[18, 32, 33] as has been suggested for galvanic displacement of gold on silicon based surface X-ray diffraction spectroscopy results.[17]

In order to confirm the epitaxial relationship between gold and silicon, selected area electron diffraction (SAED, beam size ~100 nm) was taken along the $[\bar{1}12]$ zone axis (Figure 3.5d). The silicon pattern consists of spots, due to its single crystal nature, arising from diffraction from the $(1\bar{1}1)$, (220) and $(13\bar{1})$ planes; gold shows diffraction from these same planes. Other features of note include the parallel feature of the {112} family of crystallographic planes, of both the silicon substrate and the gold overlayer. Consequently, for each Bragg diffraction spot from silicon substrate, there is gold diffraction spot of identical orientation to that of silicon. The gold $(1\bar{1}1)$ and (220) planes are parallel to the silicon $(1\bar{1}1)$ and (220) planes, respectively: Au$(1\bar{1}1)$//Si$(1\bar{1}1)$ and Au(110)//Si(110). Hence, the SAED pattern is strongly indicative of the Au(111)$[\bar{1}12]$//Si(111)$[\bar{1}12]$ in-plane epitaxial relationship of the gold-on-silicon.

Further investigation by X-ray diffraction (XRD) (Figure 3.6a) for thicker gold films on Si(111) immersed in 0.1 mM $KAuCl_4$ (aq) and 1% HF (aq) for 20 min showed gold peaks for only the (111) and (222) planes. Figure 3.6b shows the XRD 2D frame showing only a diffraction spot from Au(111) in the 2θ range of 27.4 - 62.4°. These results indicate that the only plane that is parallel to the Si(111) substrate is the Au(111) plane and the preferential growth of the gold layer along the <111> growth direction; the gold layer grew along the same crystallographic direction as the underlying substrate. Moreover, the θ-2θ scan (Figure 3.6a) indicate the <111> direction as the out-of-plane orientation for the gold film. Hence the out-of-plane relationship of Au on silicon can be represented as Au(111)//Si(111).

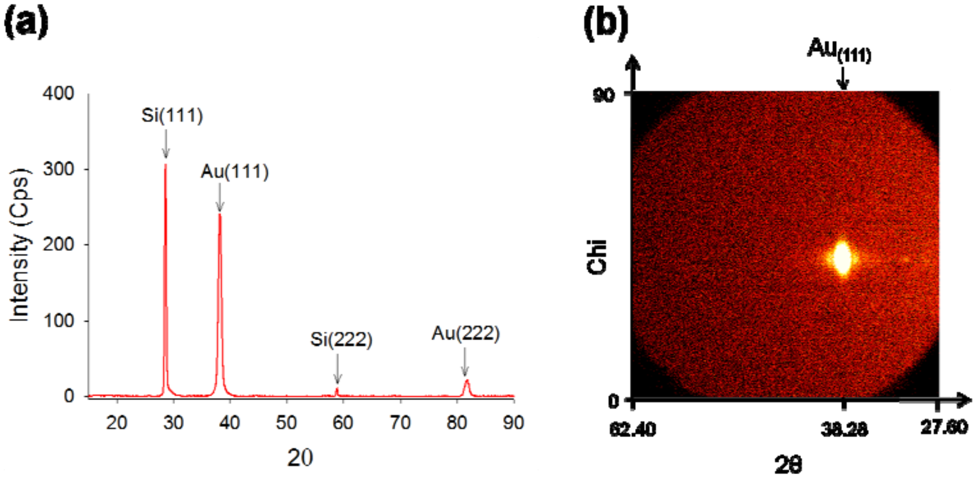

Figure 3.6. *(a) XRD θ-2θ scan for gold film on Si(111), produced after the immersion of the silicon shards in 0.1 mM* $KAuCl_4$ *(aq) + 1% HF (aq) for 20 min.* ***.*** *(b) XRD 2D diffraction frame showing a diffraction spot for Au(111) plane.*[27]

The phenomenon of heteroepitaxial crystallization involves the epitaxial growth of a layer (an epilayer) with a chemical composition and, typically, structural parameters different from those of the substrate.[18] Lattice mismatch or misfit (the disregistry of the interfacial atomic arrangement of the substrate and the overgrown epilayer) is known to have a significant effect on epitaxy.[18] Au(111) and Si(111) with interplanar d spacings of 2.355 Å and 3.134 Å, respectively, have about a 25% lattice mismatch. By considering the coincident site lattice interface (CSL), however, in which three silicon lattices match with four gold lattices, $4xd_{Au(111)}$ = 9.420 Å and $3xd_{(Si(111)}$ = 9.402 Å, the lattice mismatch is only 0.2% (Figure 3.7). Such heteroepitaxy has previously been observed for evaporated gold on silicon following annealing at temperatures greater than 380ºC.[34] A CSL interface has been considered for the epitaxial growth of the electron-beam evaporated silver on Si(111) surfaces.[35]

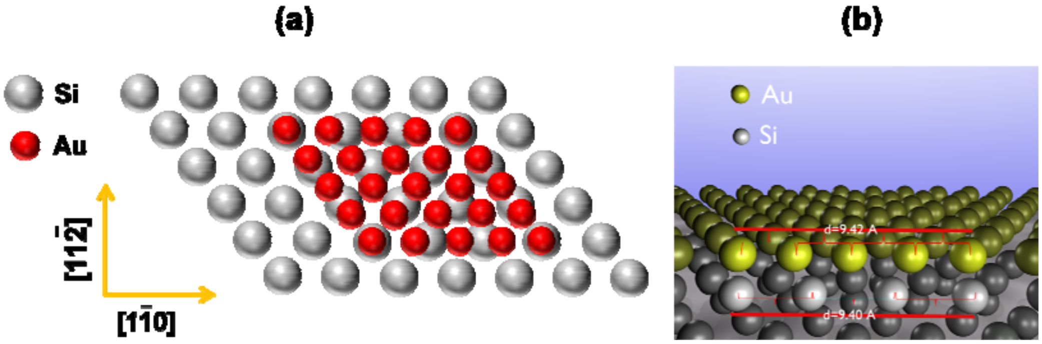

Figure 3.7. *Schematic diagram showing the coincidence of 3 Si lattices with 4 Au lattices for gold film on Si(111) [coincident site lattice interface (CSL)]. (a) Top view. (b) Side view.*[27]

In order to visualize the gold nanoparticle-silicon interfaces of Au/Si(111) and Au/Si(100) and confirm heteroepitaxy, cross-sectional high resolution TEM (HRTEM) investigations were carried out for Au-Si samples prepared after immersion of the Si shards in a mixture of 0.1 mM $KAuCl_4$ (aq) and 1% HF (aq) for 7.5 min. Figure 3.8a shows a cross-sectional HRTEM image for a gold nanocrystallite on Si(111) that reveals the coincidence of four gold lattice fringes with three silicon lattice fringes, as marked by the yellow and pink lines, respectively. This interfacial coincident nature can account for the heteroepitaxial growth of gold on Si by galvanic displacement. In addition, the top epitaxial gold planes are clearly observed parallel to the direction of those of the underlying silicon substrate as seen from the alignments of the gold and Si atoms along the white lines (Figure 3.8a). Similar results were observed for Au/Si(100) as shown in Figure 3.8b. In the case of gold on Si(100) (Figure 3.8b), the gold-silicon interface displays a significant degree of heterogeneity - some areas have very clear coincident gold and silicon lattices, whereas others appear less ordered. In the inset of Figure 3.8b, one ill-defined region is highlighted, the exact composition of which is as-of-yet unknown *(vide infra)*.

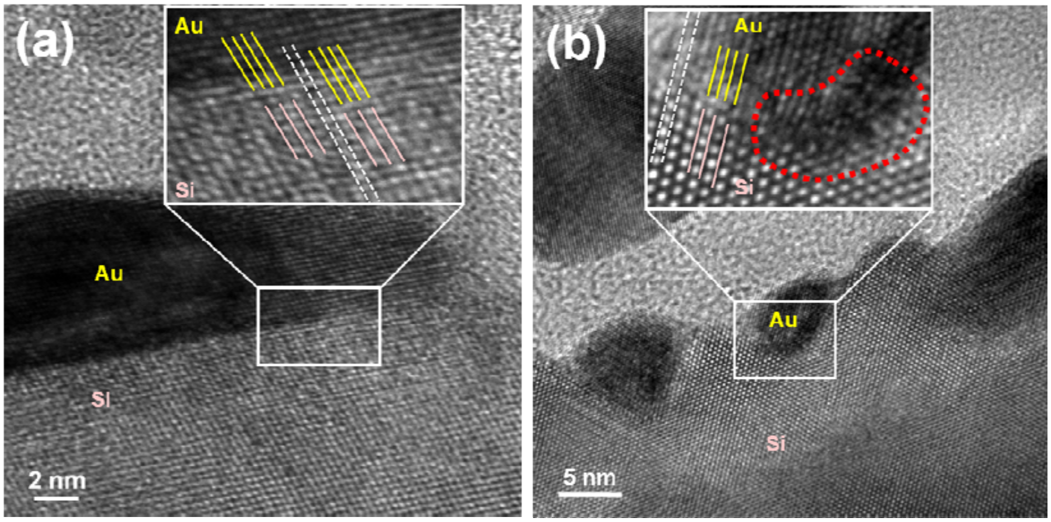

Figure 3.8. *Cross-sectional HRTEM images for gold-silicon interfaces, formed by immersing the substrates in 0.1 mM* $KAuCl_4$ *(aq) and 1% HF (aq) for 7.5 min. (a) Si(111). (b) Si(100). The yellow and pink lines show the coincident site lattice interfaces for the gold and silicon planes, respectively. The area in (b), outlined in red, highlights an ill-defined region of the gold-silicon interface. Both images were taken close to the [110] zone axis. The white lines show the alignment and the parallel nature of the gold epilayer to the underlying silicon substrate.*[27]

Because prior literature contains much postulation regarding the existence of intermetallics (gold-silicides),[16, 22] nanobeam diffraction with a 20 nm probe was utilized to glean further information about the interface between a single gold nanocrystallite and Si(111) and Si(100) surfaces, and Si nanowires. As shown in Figure 3.9, the heteroepitaxial gold-silicon relationship is visible from the nanobeam diffraction patterns of all the cross-sectional gold-silicon interfaces; The existence of gold Bragg diffraction spots of identical orientations to those of Si, and the common zone axis for gold and Si diffractions, indicate the parallel nature of the corresponding planes. Equivalently, the alignment of gold and silicon diffraction spots, marked by red and blue lines, respectively, indicates that the growth of the crystalline gold is in the direction of the underlying silicon planes; both materials diffract along the same zone axes. In the case of Si(111) and Si(100), diffraction patterns were taken along the [110] zone axis, and the [111] for the nanowires.

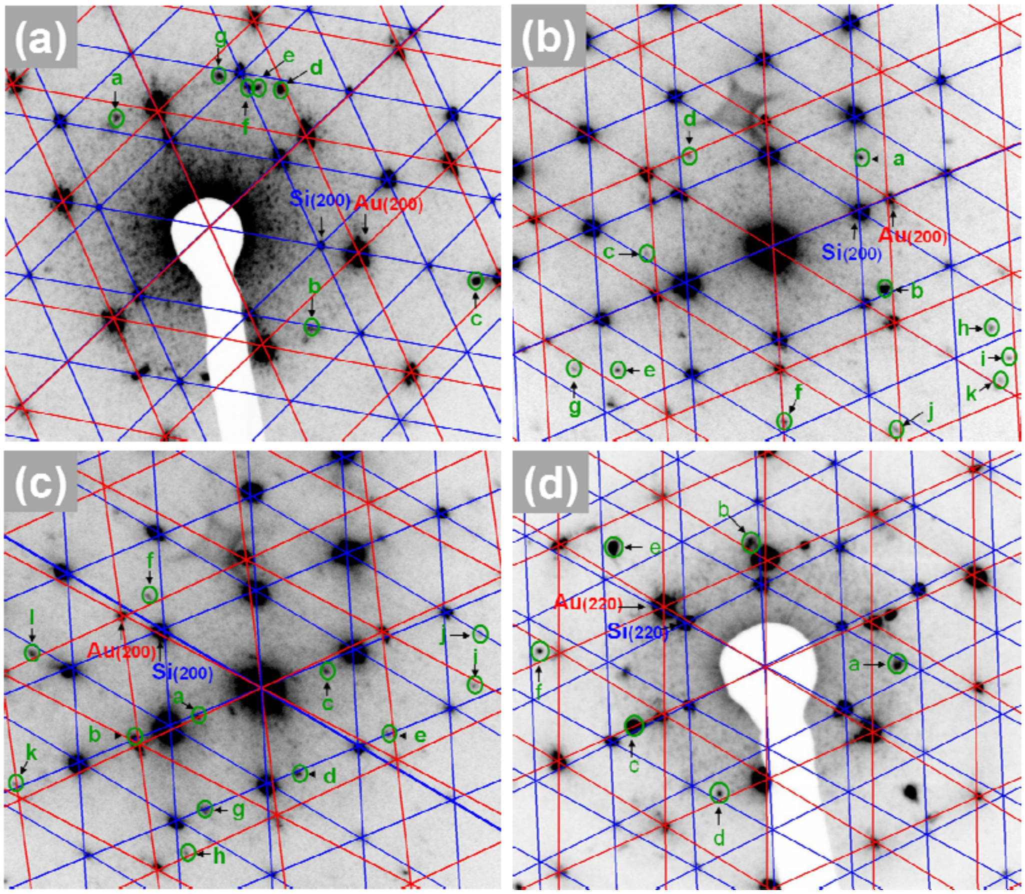

Figure 3.9. *Nanobeam diffraction patterns (probe ~20 nm) of gold-on-silicon samples. Blue and red lines correspond to silicon and gold planes, respectively. (a-c) Cross-sectioned gold-on-silicon wafers prepared through immersion of Si wafer shards in 0.1 mM* $KAuCl_4$ *(aq) + 1% HF (aq) for 7.5 min. Diffraction patterns were taken close to the [110] zone axis (a-c). (a) Si(111); (b+c) Diffraction patterns for Si(100), taken at different locations. (d) Diffraction pattern, taken close to the [111] zone axis, from an interface between an individual gold nanoparticle and a silicon nanowire prepared using 1 mM* $KAuCl_4$ *(aq) and 1% HF (aq) for 30 s.*[27]

There are, however, diffraction spots that do not correspond to either gold or silicon planes, and have interplanar spacings unrelated to the marked gold or silicon planes (red/blue lines), as indicated in green in Figures 3.9a-d. It is possible that the extra spots on Si(100)/gold result from the presence of crystalline gold silicides. In Figure 3.9a for gold on Si(111), there are 7 additional spots (in green), of which 4 can be indexed against the Au_2Si, Au_5Si, Au_7Si intermetallics (summarized in Table 3.1). In Figure 3.9b for gold on Si(100), 11 additional spots are observed of which 9 can be indexed for intermetallics (summarized in Table 3.2), and in Figure 3.9c, for a different region of gold on Si(100), 12 extra spots are observed of which 7 can be indexed for intermetallics (summarized in Table 3.3). The spots in the Si(100) case correspond to the following intermetallics: Au_7Si, Au_4Si, Au_5Si, and Au_2Si. Similarly, 6 extra spots are observed in the diffraction pattern for a gold nanoparticle on a silicon nanowire (Figure 3.9d), 3 of which can be indexed to the Au_2Si, Au_5Si and Au_7Si intermetallics (summarized in Table 3.4). Because the nanoprobe diffraction studies are certainly not comprehensive with respect to determination and characterization, and identification of all of the gold silicides phases due to the very high complexity of the system, the characterization of these gold silicides cannot be considered complete. We surmise that the intermetallics reside in the ill-defined regions (*vide supra*, Figure 3.8b) since there is no evidence for involvement of foreign material in the Si/Au interfacial layers. The gold-silicon interfaces are therefore most likely composed of regions of heteroepitaxial gold-on-silicon, and separate domains containing an intermetallic sandwiched between the gold and silicon layers.

planes	d measured, Å	silicides	d expected, Å
Si(111)	Standard		3.13
Si(200)	2.72		2.71
Au(111)	2.33		2.36
Au(200)	2.04		2.04
a	2.10	----	
b	2.17	Au_2Si(840)	2.18
c	1.13	----	
d	1.96	Au_7Si(400)	1.96
e	2.08	Au_2Si(664)	2.10
f	2.12	----	
g	2.04	Au_5Si(311)	2.03

Table 3.1. *Analysis of the nanobeam diffraction pattern shown in Figure 3.9a. The Si(111) interplanar spacing was used to calibrate the d-spacings of the observed diffraction spots. Identifications of all of the gold-silicides were performed according to the following JCPDS reference tables: (JCPDS # 26-724,* Au_2Si*), (JCPDS # 26-723,* Au_7Si*), and (JCPDS # 26-725,* Au_5Si*).*[27]

planes	d measured, Å	silicides	d expected, Å
Si (111)	standard		3.13
Si (200)	2.71		2.71
Au (111)	2.36		2.36
Au (200)	2.02		2.04
a	2.33	----	----
b	2.36	Au_2Si(820)	2.36
c	2.32	Au_2Si(660)	2.30
d	2.34	Au_5Si_2(220)	2.34
e	1.49	Au_4Si(321)	1.49
f	1.70	Au_2Si(882)	1.70
g	1.34	Au_5Si(430)	1.35
h	1.25	Au_7Si(620)	1.24
i	1.12	----	----
j	1.33	Au_5Si(510)	1.33
k	1.11	Au_7Si(640)	1.09

Table 3.2. *Analysis of the nanobeam diffraction pattern shown in Figure 3.9b. The Si(111) interplanar spacing was used to calibrate the d-spacings of the observed diffraction spots. Identifications of all of the gold-silicides were performed according to the following JCPDS reference tables: (JCPDS # 26-724,* Au_2Si*), (JCPDS # 26-723,* Au_7Si*), (JCPDS # 26-725,* Au_5Si*), and (JCPDS # 39-735,* Au_4Si*).*[27]

planes	d measured, Å	silicides	d expected, Å
Si (111)	standard		3.13
Si (200)	2.71		2.71
Au (111)	2.33		2.36
Au (200)	2.02		2.04
a	4.63	Au_2Si(410)	4.72
b	2.34	Au_2Si(820)	2.36
c	4.63	----	----
d	3.45	Au_5Si(200)	3.37
e	2.34	Au_5Si(220)	2.38
f	2.17	Au_2Si(840)	2.18
g	2.34	----	----
h	1.76	----	----
i	1.48	Au_4Si(321)	1.48
j	1.39	----	----
k	1.19	----	----
l	1.37	Au_4Si(400)	1.38

Table 3.3. *Analysis of the nanobeam diffraction pattern shown in Figure 3.9c. The Si(111) interplanar spacing was used to calibrate the d-spacings of the observed diffraction spots. Identifications of all of the gold-silicides were performed according to the following JCPDS reference tables: (JCPDS # 26-724,* Au_2Si*), (JCPDS # 26-723,* Au_7Si*), (JCPDS # 26-725,* Au_5Si*), and (JCPDS # 39-735,* Au_4Si*).*[27]

planes	d measured, Å	silicides	d expected, Å
Si(220)	standard		---
Au(220)	1.44		1.44
a	1.27	$Au_2Si(1566)$	1.28
b	1.27	----	----
c	1.22	$Au_5Si(521)$	1.23
d	1.22	----	----
e	0.87	$Au_7Si(911)$	0.86
f	0.74	----	----

Table 3.4. *Analysis of the nanobeam diffraction pattern shown in Figure 3.9d. The Si(110) interplanar spacing was used to calibrate the d-spacings of the observed diffraction spots. Identifications of all of the gold-silicides were performed according to the following JCPDS reference tables: (JCPDS # 26-724,* Au_2Si*), (JCPDS # 26-723,* Au_7Si*), and (JCPDS # 26-725,* Au_5Si*).*[27]

Figures 3.9b and 3.9c, as stated earlier, show the nanobeam diffraction patterns for gold nanoparticle-Si(100) interfaces from different locations. Figure 3.9c shows an area in which the gold planes are tilted by about ~3.3° from the silicon planes. A 2.0° tilting was observed for Au planes on Si nanowires as well, Figure 3.9d. Crystallographic tilting of heteroepitaxial systems with their vicinal substrates is often observed;[36] for instance, tilting of heteroepitaxial gold and silver on silicon has been described previously,[17, 37-40] and has been ascribed to misfit dislocation (disregistry of the epilayer and substrate planes),[36, 38, 41] misfit between the height of a gold monolayer and a silicon step,[39] or may be a contribution of both. In the case of a silicon surface in an aqueous HF solution under galvanic displacement conditions, the surface will certainly not be flat, and thus surface roughness is most likely playing an important role in the observed epitaxial tilting (Figure 3.10), which can lead to defects and dislocations.[27] Additionally, aqueous HF etching to Si(100) surfaces was found to result in more surface disordering (roughness) relative to Si(111) surfaces.[42, 43]

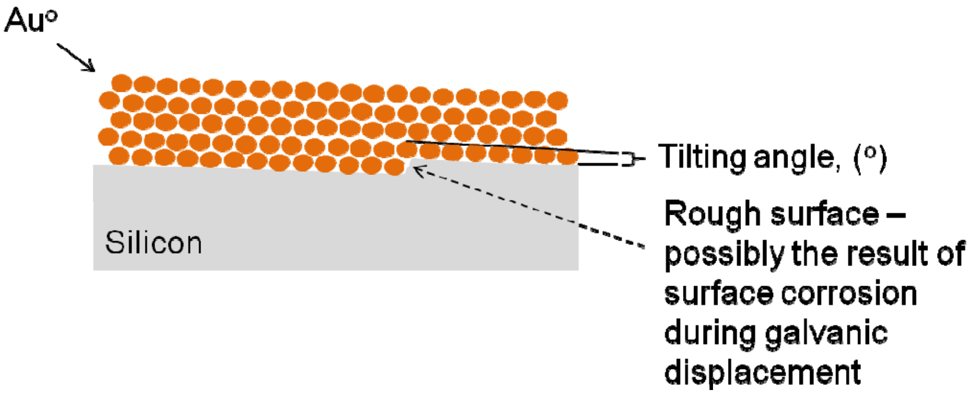

Figure 3.10. *Schematic diagram illustrating the possible effect of surface roughness, created as a result of the substrate corrosion during the galvanic displacement process, on the epitaxial tilting of gold on silicon surfaces.*

3.2.2. Epitaxy Growth Mode

For galvanic displacement of gold on silicon, two growth modes have been postulated to be in operation: the Stranski-Krastanov (SK) mode,[22] and Volmer-Weber (VW) growth (see Scheme 1.3 in Chapter 1).[17, 19-21] The SK mode is common in lattice mismatched heteroepitaxial systems such as InAs on GaAs,[44, 45] Ge on Si,[46] Ag on Si,[47] and Au on Si.[22, 48, 49] Through their AFM studies of galvanic displacement of gold on silicon, Carraro and co-workers suggest surface morphology that is consistent with the SK mode of growth, in which the silicon surface is coated with a gold silicon silicide base monolayer, decorated with gold nanoparticles.[22] The SK mode was also postulated to be the growth mode for evaporated gold on Si(111) as judged *via* STM surface studies.[48, 49] A three dimensional (3D), island or Volmer Weber (VW) growth mode has also been reported for the deposition of gold on silicon surfaces by galvanic displacement.[17, 19-21] For galvanically displaced gold on silicon, AFM studies along with surface X-ray diffraction[17] and surface second harmonic generation[19-21] analyses reveal Au cluster formation which would be suggestive of a 3D or VW growth mechanism.

In order to try to shed some light on the possible mechanism, detailed cross-sectional TEM imaging was employed, as shown in Figure 3.11 for Au on Si(111) and Figure 3.12 for Au on Si(100). Two silicon wafers were immersed for 7.5 min in a solution of 0.1 mM $KAuCl_4$ (aq) and 1% HF (aq), followed by gluing them together with a ~100 nm layer of M-Bond and then microtomed to form a sandwich less than one micron thick (details in the experimental section).

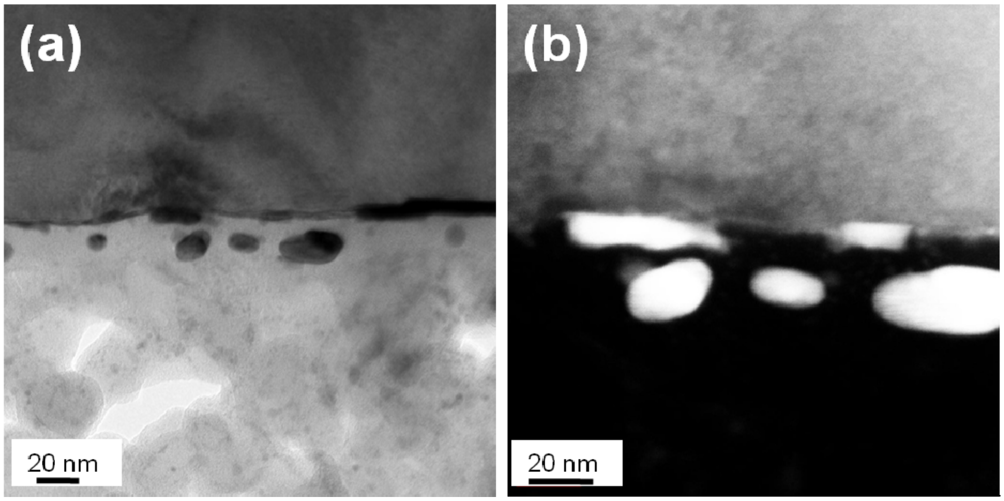

Figure 3.11. *Cross-sectional transmission electron microscopy (TEM) images for Au galvanically displaced on Si(111) after immersing the silicon substrate in 0.1 mM KAuCl$_4$ (aq) + 1% HF (aq) for 7.5 min. (a) Bright-field TEM image. (b) Dark-field TEM image.*[27]

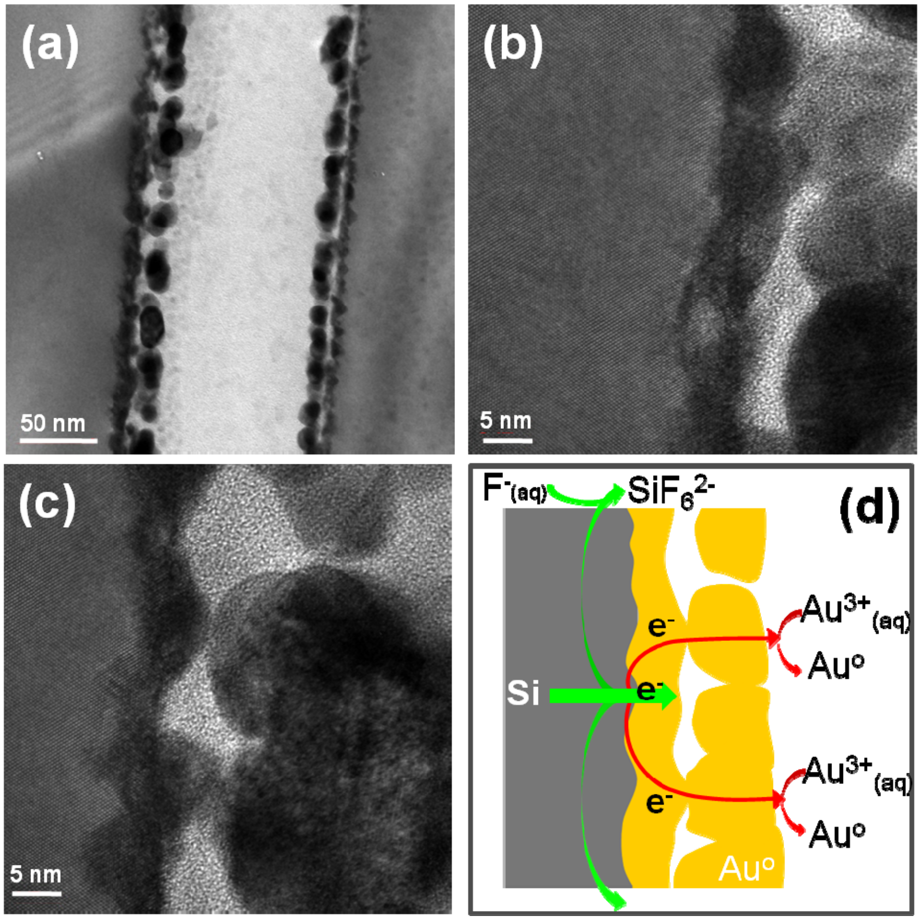

Figure 3.12. *TEM images showing the growth mode of Au on Si(100). (a) Cross-section TEM image of gold-on-Si(100) grown by immersing the silicon substrate in 0.1 mM KAuCl$_4$ (aq) + 1% HF (aq) for 7.5 min. (b) and (c) Cross-section HRTEM images of the same sample shown in (a). (d) Schematic diagram showing VW growth during the galvanic displacement process.*[27]

As can be seen in Figures 3.12a-c [for Au on Si(100), there is a ~5 nm thick layer of gold (gold lattice planes are visible)], closely allied with the silicon substrate, capped by an overlayer of necked gold particles. The high resolution TEM images (Figure 3.12b and c) show that the ~5 nm gold layer is formed by the coalescence of gold nanoparticles that presumably grew from the initially formed nuclei on the rough (on the nanoscale) silicon surface. The rough nature of this interface results in scattered nucleation events,[50] followed by growth of metallic gold until the metal deposits make contact with each other. The apparent overlayer of nanoparticle growth, above the initial gold-silicon contact, results from further deposition on the surface with longer immersion times in which the more closely silicon-bonded gold acts as the cathodic layer through which electron transport takes place. These electrons, produced from the corrosion of the exposed silicon surface, perhaps nearby or distal,[51-54] reduce gold ions in close vicinity in the solution to metallic gold, producing the necked particle overlayer. Figure 3.12d schematically illustrates a possible mechanism for the galvanic displacement process for gold on silicon, in which electrons from silicon dissolution promoted by fluoride ion lead to reduction of gold (III) complexes in the aqueous solution. The discrepancy between the observed results from different research groups most likely arises from the varying conditions used by each. If the conditions are such that deposition occurs on atomically flat hydride-terminated Si(111) planes, for instance, then an SK growth mode would be more likely. In our case, silicon surface roughening (on the nanoscale) is promoted by galvanic displacement,[57] and thus the VW growth appears to predominate, at least initially. The observed roughening of the interfaces during galvanic displacement is almost certainly the cause for VW island growth mode, and may also be the source of interfacial heterogeneity with respect to gold-silicon intermetallic formation, and heteroepitaxy.

3.2.3. Preferential Growth of Au Nanoparticles on Si NWs

In galvanic displacement (GD) process, the semiconductor surfaces act as the source of reducing electrons for the reduction of metal ions from the deposition bath. Hence, GD has shown selective metal deposition on the exposed semiconductor surfaces. Semiconductor nanowires functionalized with metallic nanoparticles, prepared by GD, were found to be useful in a variety of applications including sensing and photovoltaic research due to the large surface area of the nanowires, which act as a support for the nanoparticles.[55-58] The determination of the 2 and 3D morphology of the metallic deposits and the nanowire support and, in particular, the determination of the preferential orientation and deposition of the gold deposits on silicon nanowires, which are composed of several exposed facets, is important not only for the fundamental science behind the study, but also for choosing the appropriate nanowires whose facets and growth directions can be controlled depending on the synthetic conditions.[59, 60]

Transmission electron microscopy 2D imaging has become an indispensable technique to obtain detailed structural information on materials. Recently, electron tomography (ET) has shown an extra advantage of the TEM.[61, 62] ET allows the capture of multiple 2D images taken at different tilt angles and hence it can be used to reconstruct and give information about the object's 3D morphology and orientation.[61] This approach has been shown to be a versatile method to characterize the 3D structure of biological specimen,[62] quantum dots,[61] and catalysts.[63]

In order to investigate the orientation of gold nanoparticles (prepared by GD) on Si NWs, we performed electron tomography for a gold-Si NW prepared after exposure of a Si NWs substrate to a mixture of 1 mM $KAuCl_4$ (aq) and 1% HF (aq) for 30 s. Figure 3.13 shows two tilting series taken with low (Figure 3.13a) and high resolution (Figure 3.13b). Each series of projections was collected over a tilt range of 0 – 75^o, with an image recorded every 15^o. The 2D image (i) (Figure 3.13a), shown at a 0^o tilting angle, indicates that the nanoparticles are all aligned along the pink line. However, with further tilting along the axis shown in image (vi) in Figure 3.13a, the Au nanoparticles start to be resolved. At a tilting angle of 75^o, the nanoparticles appeared to be lying on two opposite or parallel faces. This phenomenon explains the alignment seen at the 0^o tilting angle, and indicates a preferential face deposition of gold nanoparticles. Figure 3.14 shows a low resolution TEM 2D image revealing the preferential alignment and growth of gold nanoparticles. A 3D model (Figure 3.15) was reconstructed from 140 images taking from a tilting series starting from -70^o to 70^o, with 1^o steps. This model shows the opposite alignment of the gold deposits.

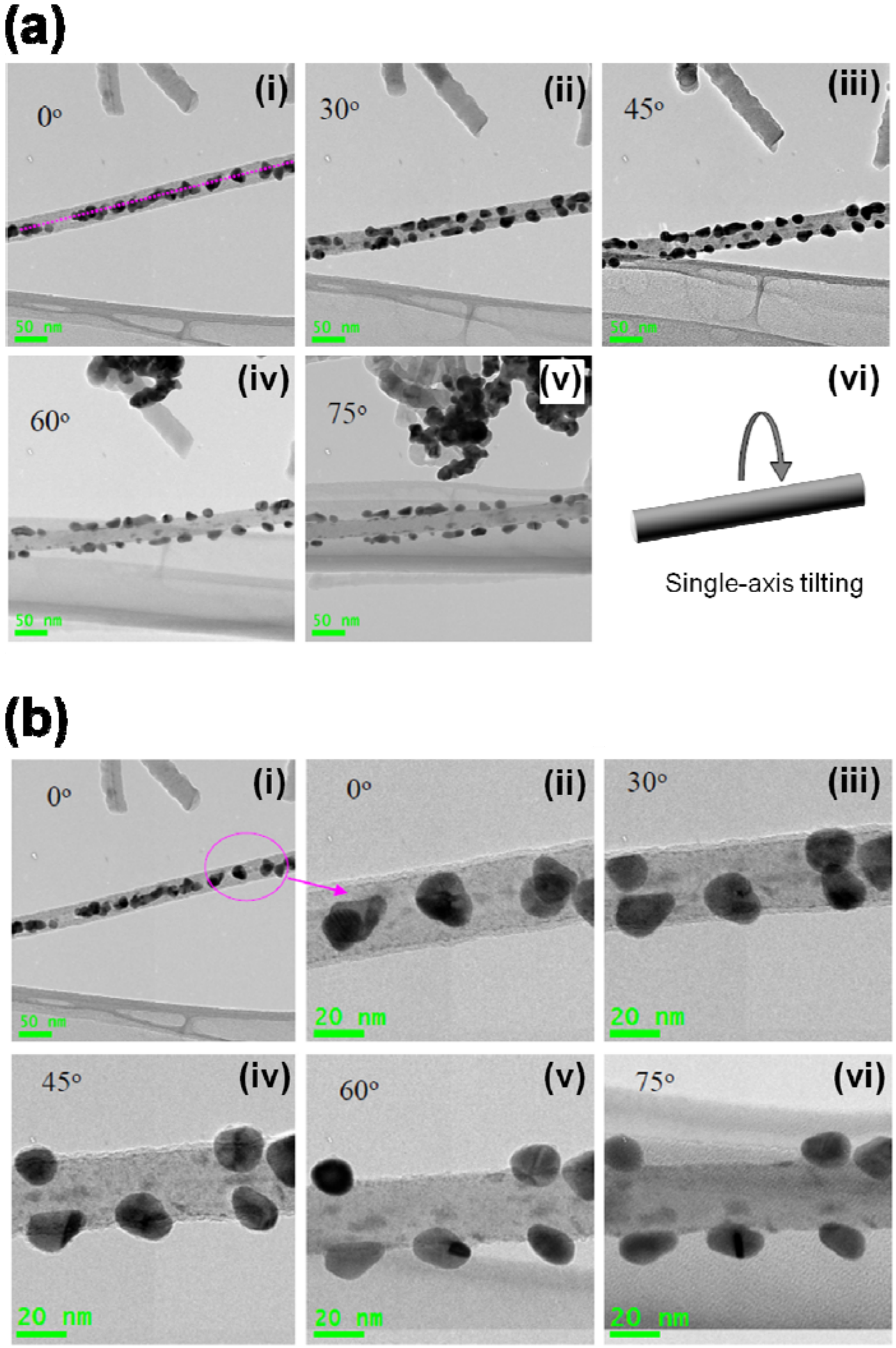

Figure 3.13. *Bright-field TEM micrographs of Au nanoparticles on a Si nanowire at different degrees of sample tilting starting from* 0^{o} *to* 75^{o} *at a* 15^{o} *tilting step. (a), and (b) are tilting series at lower and higher magnifications, respectively.*

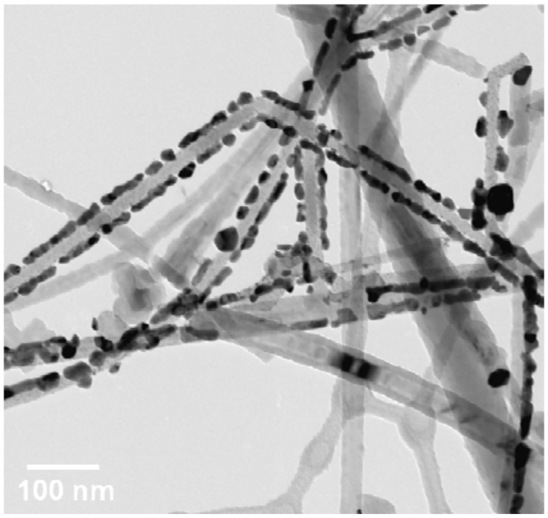

Figure 3.14. *Bright-field TEM micrograph for gold nanoparticles grown on Si NWs after 30 s of surface exposure to a mixture of 1 mM* $KAuCl_4$ *(aq) and 1% HF (aq).*

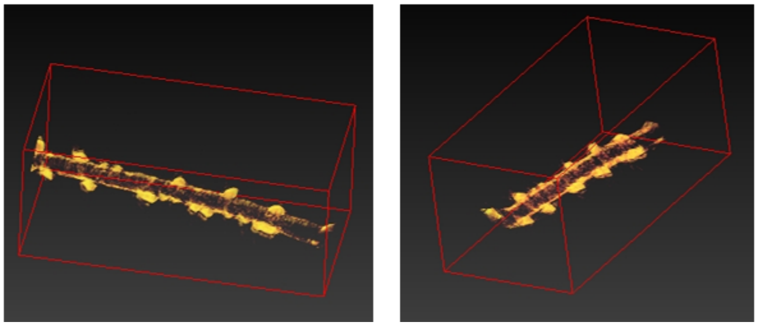

Figure 3.15. *Views of a 3D reconstruction model of the Au/Si NW, collected from a tilting series from -70 to* 70^o *at* 1^o *per step.*

In order to characterize the nanowire faces, a high resolution TEM image (Figure 3.16 b) was taken along the [111] zone axis from the red marked area in the TEM image shown in Figure 3.16a. A nanobeam diffraction pattern (Figure 3.9d) was taken from the Au-Si interfacial area, marked yellow, in Figure 3.16b.

The diffraction pattern was taken along the [111] zone axis, indicating the (111) plane as the exposed side of the Si nanowire. Moreover, as shown in the HRTEM image (Figure 3.16b), the nanowire side covered with gold nanoparticles is the (110) face, and the growth direction of the nanowire is the <112>. Si nanowires with a <112> growth direction are characterized by only one configuration, a rectangular shape with two (111) and two (110) faces (Figure 3.17).[60] Figures 3.18a and 3.18b show the 3D reconstructed model for a Au/Si NW, while Figures 3.18c-f show cross-sectional slices taken along the reconstructed model shown in Figures 3.18a and 3.18b. The cross-sectional view seen in Figure 3.18c indicates the rectangular nature of the nanowire. Moreover, the opposite location of the gold nanoparticles is seen from the slices shown in Figures 3.18d-f. The driving force for the gold deposition on the Si(110) rather than the Si(111) faces is most likely due to surface energy differences between the two crystal planes.[64] Si(110) faces are of higher surface energy (1.43 J m^{-2}) compared to 1.23 J m^{-2} for Si(111).[64] Moreover, from the atomic model shown in Figure 3.19, the Si(110) is the most open structure, while the Si(111) surface is the closest packed, with each apical silicon atom being trisubstituted. Therefore, the (110) surfaces, being less substitutes, are more reactive compared to the (111). Hence, the reactivity of the (110) planes may explain the selective deposition over these surfaces.

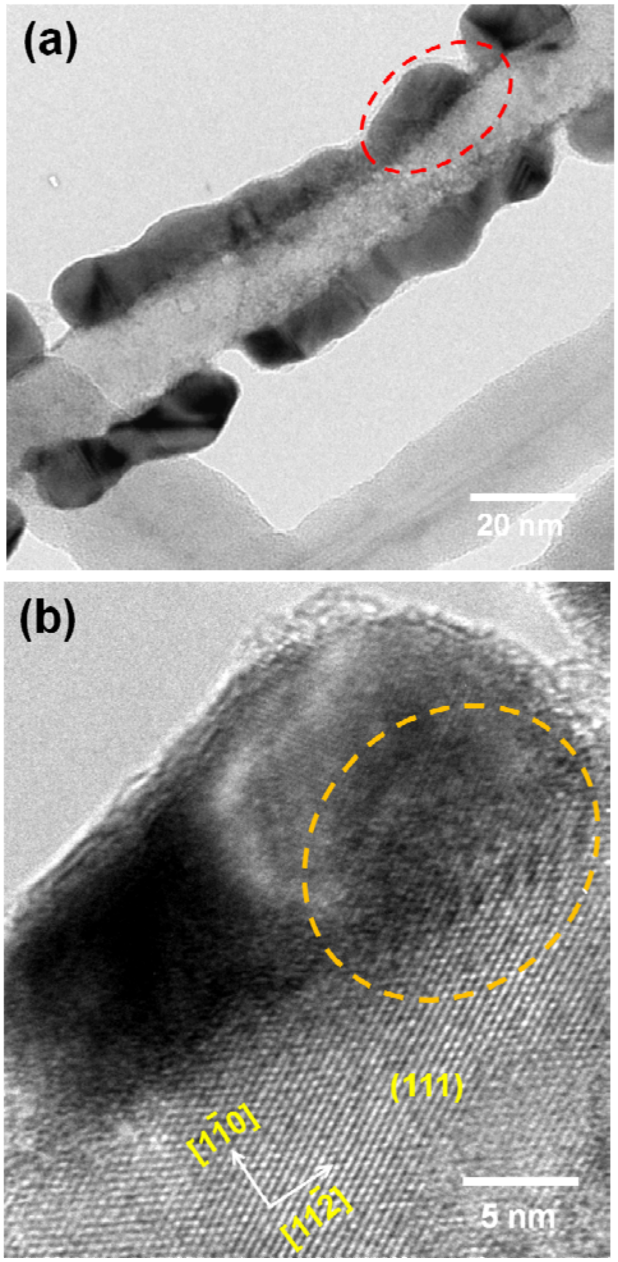

Figure 3.16. *(a) Bright-field TEM micrograph for gold nanoparticles grown on Si NWs after 30 s of surface exposure to a mixture of 1 mM* $KAuCl_4$ *(aq) and 1% HF (aq). (b) High resolution TEM micrograph of the marked (red) area in image (a), and the yellow marked area resulted in the nanobeam diffraction pattern in Figure 9d.*

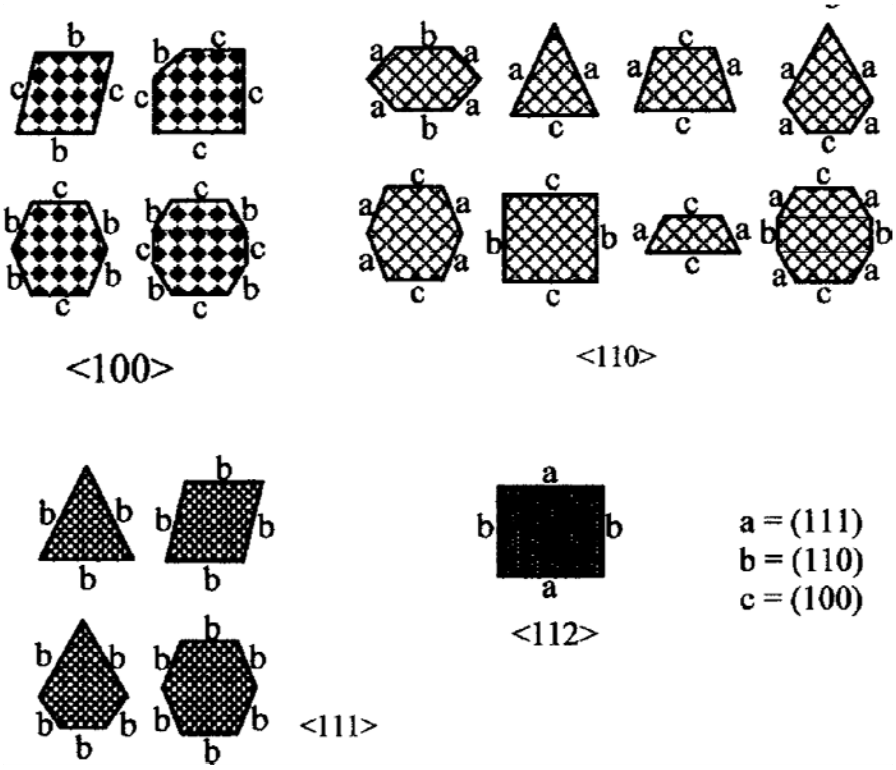

Figure 3.17. *Cross-sectional models of <100>, <110>, <111>, and <112> Si NWs.*[60] *Copyright © American Institute of Physics. Reproduced with permission from ref. 60.*

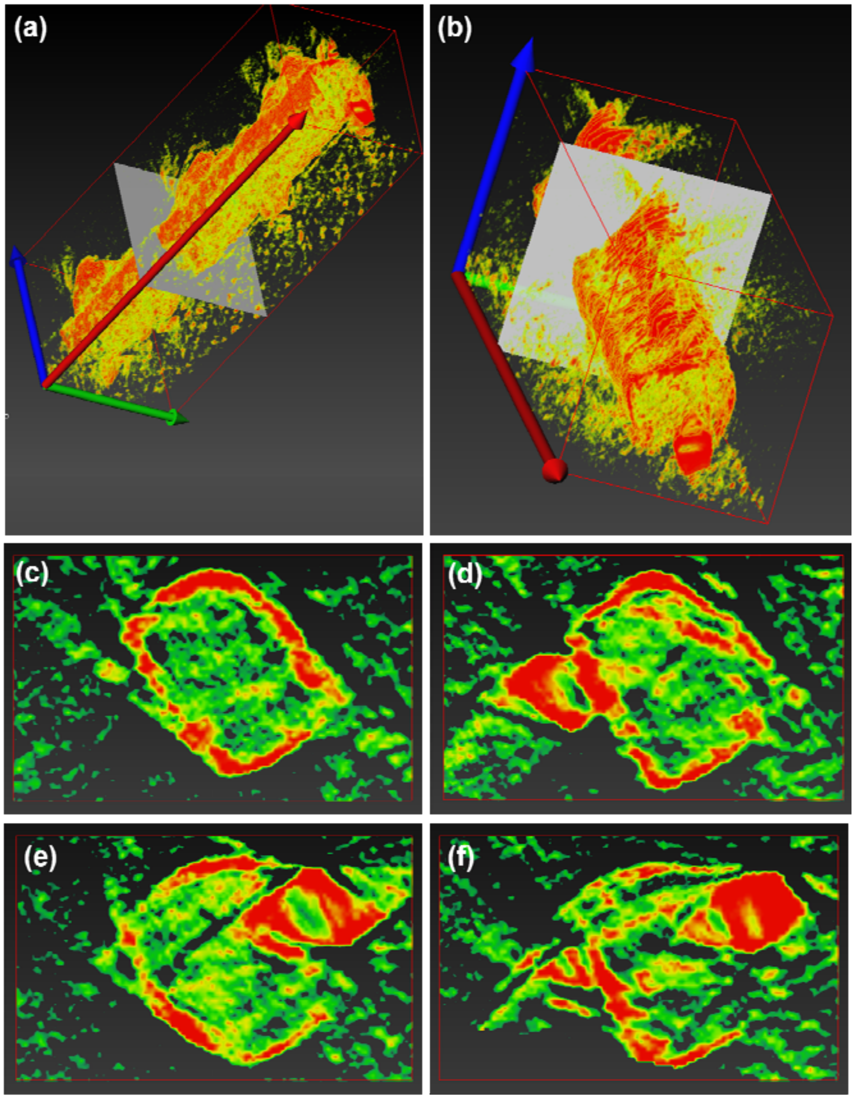

Figure 3.18. *(a, b) 3D electron tomographic reconstructions of a Au/Si NW, obtained from a tilting series from -70*^{o} *to 70*^{o} *at 1*^{o} *per step. The white plane indicates an example location of a 2D section through the 3D reconstructed sample volume. (c-f) Cross-sectional views for slices taken along the reconstructed data cube shown in (a) and (b). Data were obtained and reconstructions were performed by Peng Li MSc, a technical officer at the National Institute for Nanotechnology. Presented with permission from Mr. Peng Li.*

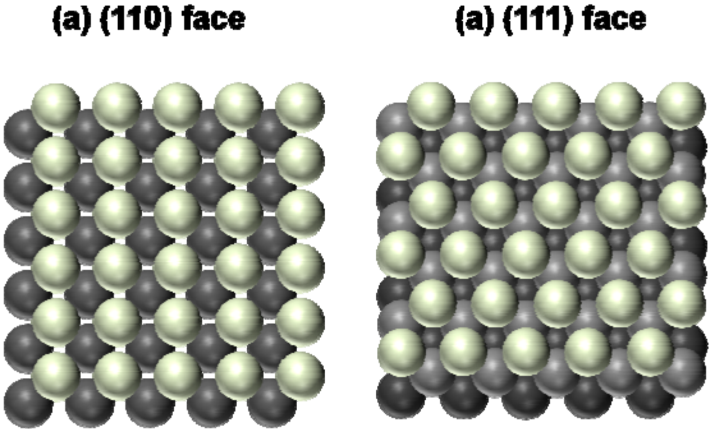

Figure 3.19. *(a), and (b) Atomic models for Si(110) and Si(111) surfaces, respectively.*

It is worth noting, that Dr. Dong Wang (a former Postdoctoral Fellow in Buriak group) carried out preliminary examinations of the Si(111) and Si(110) surfaces with regards to their corrosion resistance. However, this research point needs to be continued. Moreover, Dr Wang studied the deposition of gold nanoparticles on Si(110) surfaces with etched pits, prepared through the etching of Si(110) samples covered with a monolayer of self-assembled polystyrene-*block*-poly (4-vinyl pyridine) "PS-*b*-P4VP" block copolymer [PS-*b*-P4VP, (*M*n) 128 400-*b*-33 500 g/mol)] in dilute HF (aq) (Figure 3.20a), of (111) and (100) exposed faces (Figure 3.20b). As shown in Figure 3.20c, the immersion of a patterned Si(110) shard in a 15 μM $KAuCl_4$ (aq) + 0.1% HF (aq) solution for 8 min resulted in the deposition of gold nanoparticles on the Si(110) surfaces with minor or negligible deposition inside the pits walls [(111) and (100) faces]. These results agree with the preferred gold deposition on Si(110) faces of <112> Si nanowires (Figure 3.16).

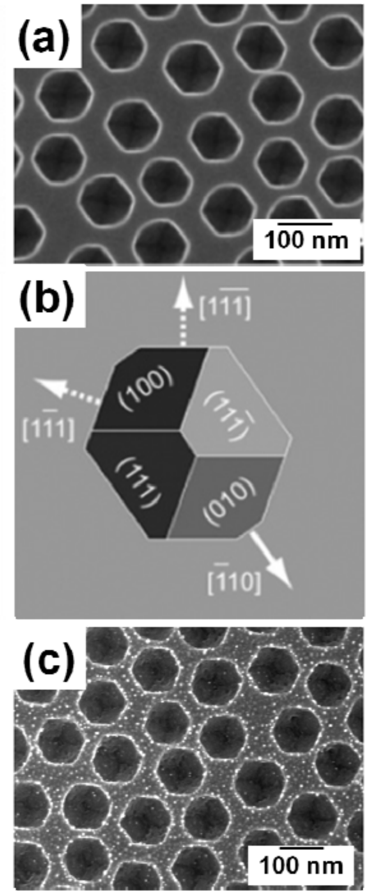

Figure 3.20. *(a) SEM micrograph of Si(110) surface with pits formed by etching a sample covered with a monolayer of self-assembled PS-b-P4VP block copolymer [PS-b-P4VP, (Mn , 128 400-b-33 500 g/mol)] in Ar sparged 0.01% HF (aq) for 40 min.*[65] *(b) a proposed model showing the exposed faces of the etch pits.*[65] *(c) SEM image of gold nanoparticles grown after the immersion of the patterned Si(110) shard in a mixture of (15 µM* $KAuCl_4$ *(aq) + 0.1% HF (aq)) for 8 min. Copyright © 2007 American Chemical Society. Reproduced with permission from ref. 65. Image (c) was presented with permission from Dr. Dong Wang.*

3.3. Conclusions

Galvanic displacement is a useful approach for synthesizing metal-on-semiconductor interfaces for a range of applications. Through detailed TEM and nanobeam diffraction studies of galvanic gold deposition on silicon [Si(100), Si(111) and silicon nanowires], a better understanding of the interface between the silicon and the metallic gold was achieved. A heteroepitaxial relationship between the gold and silicon was confirmed, and was directly observed by high resolution TEM on both single crystal silicon shards and nanowires, revealing a coincident of four gold to three silicon atoms (lattice mismatch of 0.2%). Nanobeam diffraction patterns taken from a 20 nm gold-silicon interfacial area reveal a host of spurious spots that are clearly not derived from known gold or silicon planes, but are suggestive of gold-silicon intermetallics. Cross-section TEM images of microtomed samples reveal a rough silicon interface and nucleated island growth of gold that is suggestive of Volmer-Weber growth, under these conditions. Finally, electron tomography revealed a preferential face deposition of gold nanoparticles on <112> Si NWs by galvanic displacement method.

3.4. Experimental Section

Generalities:

Unless otherwise noted, all experiments were performed under ambient laboratory conditions. Si(111) and Si(100) (p-type, B-doped, $\rho<0.005\ \Omega\cdot\mathrm{cm}$, 500 μm thickness) wafers were purchased from Silicon Quest International, Inc. $KAuCl_4 \cdot xH_2O$ was purchased from Strem Chemicals. Anchored silicon nanowires were grown by the vapour liquid solid technique on a p-type (B–doped) Si(100) substrate.[4, 66]

Pretreatment of Silicon Substrates:

All wafers were diced into 1 cm^2 pieces with a diamond scriber. Silicon shards were degreased in a methanol ultrasonic bath for 15 min and dried under a nitrogen stream. The wafers were then cleaned using the following standard RCA cleaning procedures.[67] The wafers were first immersed into a hot solution of H_2O:NH_4OH:H_2O_2 (5:1:1) for 15 min, and after rinsing with excess water, they were immersed into a hot solution of H_2O:HCl:H_2O_2 (6:1:1) for 15 min. The wafers were again rinsed with excess water and then dried under a stream of nitrogen. Following this cleaning procedure, the wafers were immersed into 1% HF (aq) for 7 min, to remove the native surface oxide film. The samples were then rinsed with water and dried under a nitrogen stream. In the case of silicon nanowires, the wafer was divided into smaller pieces. Each substrate was cleaned by immersion in a mixture of H_2SO_4:H_2O_2 (aq) (1:1) for 5 min.[4] The samples were then rinsed with distilled water and dried under nitrogen. To hydrogen passivate the silicon nanowires, the substrates were immersed in 1% HF (aq) for 3 min, then rinsed with water and dried under nitrogen.

Metal Deposition:

The silicon wafer shard was immersed in the desired aqueous gold salt and hydrofluoric acid solution in a Teflon beaker. The gold salt/acid solutions were prepared by mixing 0.1 ml of 0.01 M $KAuCl_4 \cdot xH_2O$ and 9.9 ml of 1% HF (aq) for a given time. After metal deposition, the sample was thoroughly rinsed with water and dried under a nitrogen stream. In the case of silicon nanowires, a 10 µl drop of 1 mM $KAuCl_4$ (aq) and 1% HF (aq) was placed on the nanowire-coated substrate surface for 30 s, then rinsed with distilled water and dried under nitrogen.[4]

Surface Characterization:

The gold nanostructures on the silicon surfaces were characterized by scanning electron microscopy (SEM), transmission electron microscopy (TEM), and X-ray diffraction (XRD). SEM (Hitachi S-4800 FE-SEM) of gold nanostructures was typically performed with an electron energy of 20 keV. TEM images and nanobeam electron diffraction patterns, using a probe of about 20 nm, were recorded on a 200 kV JEOL 2200FS TEM/STEM instrument, equipped with a high tilt cryo-polepiece. X-ray diffraction was performed on a Bruker D8 Discover instrument equipped with a sealed Cu tube. The peaks in the X-ray diffraction pattern were identified in terms of the Bragg angle, 2θ.

TEM Sample Preparation:

For cross-sectional samples of Si(111) and Si(100), six gold-silicon samples were glued together using M-Bond. A 3 mm cylinder was then cut from the side of the six wafers using an ultrasonic cutter and this cylinder was then inserted into a copper cylinder with epoxy. The copper tube was cut by a diamond saw into small disks about 600 μm thick. Each disk was then polished on both sides to 100 μm thickness. A ~1 μm thickness was achieved by dimpling from both sides. For plan view samples, the backside of the silicon shard was mechanically polished until the silicon was thinned to less than a micron. After achieving sub-micron thicknesses for both cross-section and plan view samples, ion milling was then used to create a small hole and clean the surface. Milling was done at low temperature (< –100ºC with LN_2 cooling) at 6º milling angle, and with a voltage/current of 5V/3mA at the beginning, and 0.5V/3mA for final polishing. In the case of silicon nanowires, the substrate was immersed into a vial with 100% ethanol and ultrasonicated for 5 min. A drop of the supernatant layer was then spotted onto a lacy carbon grid.

3.5. References

(1) San Paulo, A.; Arellano, N.; Plaza, J. A.; He, R. R.; Carraro, C.; Maboudian, R.; Howe, R. T.; Bokor, J.; Yang, P. D. *Nano Letters* **2007**, *7*, 1100-1104.

(2) Shimizu, T.; Xie, T.; Nishikawa, J.; Shingubara, S.; Senz, S.; Gosele, U. *Advanced Materials* **2007**, *19*, 917-920.

(3) Shimizu, T.; Senz, S.; Shingubara, S.; Gosele, U. *Applied Physics A-Materials Science & Processing* **2007**, *87*, 607-610.

(4) Yasseri, A. A.; Sharma, S.; Kamins, T. I.; Li, Z.; Williams, R. S. *Applied Physics A-Materials Science & Processing* **2006**, *82*, 659-664.

(5) Aizawa, M.; Buriak, J. M. *Journal of the American Chemical Society* **2005**, *127*, 8932-8933.

(6) Gao, D.; He, R. R.; Carraro, C.; Howe, R. T.; Yang, P. D.; Maboudian, R. *Journal of the American Chemical Society* **2005**, *127*, 4574-4575.

(7) Porter, L. A.; Choi, H. C.; Schmeltzer, J. M.; Ribbe, A. E.; Elliott, L. C. C.; Buriak, J. M. *Nano Letters* **2002**, *2*, 1369-1372.

(8) Hochbaum, A. I.; Chen, R. K.; Delgado, R. D.; Liang, W. J.; Garnett, E. C.; Najarian, M.; Majumdar, A.; Yang, P. D. *Nature* **2008**, *451*, 163-U165.

(9) Bahar, R. I.; Hammerstrom, D.; Harlow, J.; Joyner, W. H.; Lau, C.; Marculescu, D.; Orailoglu, A.; Pedram, M. *Computer* **2007**, *40*, 25.

(10) Allan, A.; Edenfeld, D.; Joyner, W. H.; Kahng, A. B.; Rodgers, M.; Zorian, Y. *Computer* **2002**, *35*, 42-53.

(11) Wolfe, C. M.; Holonyak, J., N. ; Stillman, G. E. *Physical Properties of Semiconductors*; Prentice Hall: Englewood Cliff, NJ, 1989.

(12) Sze, S. M. *Semiconductor Devices, Physics, and Technology*; Wiley: New York, 2002.

(13) Adachi, S. *Handbook on Physical Properties of Semiconductors*; Kluwer Academic: Norwell, 2004.

(14) Doerk, G. S.; Ferralis, N.; Carraro, C.; Maboudian, R. *Journal of Materials Chemistry* **2008**, *18*, 5376-5381.

(15) Yasseri, A. A.; Sharma, S.; Jung, G. Y.; Kamins, T. I. *Electrochemical and Solid State Letters* **2006**, *9*, C185-C188.

(16) Zhao, L. Y.; Siu, A. C. L.; Petrus, J. A.; He, Z. H.; Leung, K. T. *Journal of the American Chemical Society* **2007**, *129*, 5730-5734.

(17) Warren, S.; Reitzle, A.; Kazimirov, A.; Ziegler, J. C.; Bunk, O.; Cao, L. X.; Renner, F. U.; Kolb, D. M.; Bedzyk, M. J.; Zegenhagen, J. *Surface Science* **2002**, *496*, 287-298.

(18) Herman, M. A., Richter, W. & Sitter, H. *Epitaxy; Physical Principles and Technical Implementation*; Springer 2004.

(19) Rossiter, C.; Suni, II *Surface Science* **1999**, *430*, L553-L557.

(20) Srinivasan, R.; Suni, II *Surface Science* **1998**, *408*, L698-L702.

(21) Srinivasan, R.; Suni, II *Journal of the Electrochemical Society* **1999**, *146*, 570-573.

(22) Ferralis, N.; Maboudian, R.; Carraro, C. *Journal of Physical Chemistry C* **2007**, *111*, 7508-7513.

(23) *Bruker Axs Inc., Bruker Advanced X-Ray Solutions: General Area Detector Diffraction Systems (GAADS)*; GAADS User's Manual: Madison.

(24) Oskam, G.; Long, J. G.; Natarajan, A.; Searson, P. C. *Journal of Physics D-Applied Physics* **1998**, *31*, 1927-1949.

(25) Aizawa, M.; Cooper, A. M.; Malac, M.; Buriak, J. M. *Nano Letters* **2005**, *5*, 815-819.

(26) Carraro, C.; Maboudian, R.; Magagnin, L. *Surface Science Reports* **2007**, *62*, 499-525.

(27) Sayed, S. Y.; Wang, F.; Mallac, M.; Meldrum, A.; Egerton, R. F.; Buriak, J. M. *ACS Nano* **2009**, *3*, 2809-2817.

(28) Miyake, H.; Ye, S.; Osawa, M. *Electrochemistry Communications* **2002**, *4*, 973-977.

(29) Magagnin, L.; Maboudian, R.; Carraro, C. *Journal of Physical Chemistry B* **2002**, *106*, 401-407.

(30) Nason, T. C.; You, L.; Lu, T. M. *Journal of Applied Physics* **1992**, *72*, 466-470.

(31) Li, B. Q.; Zuo, J. M. *Physical Review B* **2005**, *72*, -.

(32) De Graef, M. *Intoduction to Conventional Transmission Electron Microscopy*; Cambridge University Press, 2003.

(33) Pashley, D. W., Stowell, M. J., Jacobs, M. H. & Law, T. J. *Philosophical Magazine* **1964**, *10*, 127-158.

(34) Yokota, Y.; Hashimoto, H.; Saito, N.; Endoh, H. *Japanese Journal of Applied Physics Part 2-Letters* **1986**, *25*, L168-L170.

(35) Li, B. Q.; Zuo, J. M. *Surface Science* **2002**, *520*, 7-17.

(36) Ayers, J. E.; Ghandhi, S. K.; Schowalter, L. J. *Journal of Crystal Growth* **1991**, *113*, 430-440.

(37) Sugihara, S.; Okazaki, K.; Suganuma, K. *Journal of Materials Science* **1993**, *28*, 2455-2458.

(38) Legoues, F. K.; Liehr, M.; Renier, M.; Krakow, W. *Philosophical Magazine B-Physics of Condensed Matter Statistical Mechanics Electronic Optical and Magnetic Properties* **1988**, *57*, 179-189.

(39) Munford, M. L.; Maroun, F.; Cortes, R.; Allongue, P.; Pasa, A. A. *Surface Science* **2003**, *537*, 95-112.

(40) Piscopiello, E.; Tapfer, L.; Antisari, M. V.; Paiano, P.; Prete, P.; Lovergine, N. *Physical Review B* **2008**, *78*, 0353051 - 0353057.

(41) Sundaravel, B.; Das, A. K.; Ghose, S. K.; Sekar, K.; Dev, B. N. *Applied Surface Science* **1999**, *137*, 11-19.

(42) Eaglesham, D. J.; Higashi, G. S.; Cerullo, M. *Applied Physics Letters* **1991**, *59*, 685-687.

(43) Chabal, Y. J.; Higashi, G. S.; Raghavachari, K.; Burrows, V. A. *Journal of Vacuum Science & Technology A-Vacuum Surfaces and Films* **1989**, *7*, 2104-2109.

(44) Karrai, K.; Warburton, R. J.; Schulhauser, C.; Hogele, A.; Urbaszek, B.; McGhee, E. J.; Govorov, A. O.; Garcia, J. M.; Gerardot, B. D.; Petroff, P. M. *Nature* **2004**, *427*, 135-138.

(45) Bimberg, D.; Grundmann, M.; Ledentsov, N. N.; Ruvimov, S. S.; Werner, P.; Richter, U.; Heydenreich, J.; Ustinov, V. M.; Kopev, P. S.; Alferov, Z. I. *Thin Solid Films* **1995**, *267*, 32-36.

(46) Hansson, P. O.; Albrecht, M.; Dorsch, W.; Strunk, H. P.; Bauser, E. *Physical Review Letters* **1994**, *73*, 444-447.

(47) Glueckstein, J. C.; Evans, M. M. R.; Nogami, J. *Physical Review B* **1996**, *54*, 11066-11069.

(48) Rota, A.; Martinez-Gil, A.; Agnus, G.; Moyen, E.; Maroutian, T.; Bartenlian, B.; Megy, R.; Hanbucken, M.; Beauvillain, P. *Surface Science* **2006**, *600*, 1207-1212.

(49) Kirakosian, A.; Lin, J. L.; Petrovykh, D. Y.; Crain, J. N.; Himpsel, F. J. *Journal of Applied Physics* **2001**, *90*, 3286-3290.

(50) Niwa, D.; Homma, T.; Osaka, T. *Journal of Physical Chemistry B* **2004**, *108*, 9900-9904.

(51) Torcheux, L.; Mayeux, A.; Chemla, M. *Journal of the Electrochemical Society* **1995**, *142*, 2037-2046.

(52) Hon, M.; DelRio, F. W.; White, J. T.; Kendig, M.; Carraro, C.; Maboudian, R. *Sensors and Actuators A-Physical* **2008**, *145*, 323-329.

(53) Pierron, O. N.; Macdonald, D. D.; Muhlstein, C. L. *Applied Physics Letters* **2005**, *86*.

(54) Miller, D. C.; Gall, K.; Stoldt, C. R. *Electrochemical and Solid State Letters* **2005**, *8*, G223-G226.

(55) Galopin, E.; Barbillat, J.; Coffinier, Y.; Szunerits, S.; Patriarche, G.; Boukherroub, R. *ACS Applied Materials & Interfaces* **2009**, *1*, 1396-1403.

(56) Yan, S. C.; He, N. Y.; Song, Y. C.; Zhang, Z. J.; Qian, J. Q.; Xiao, Z. D. *Journal of Electroanalytical Chemistry* **2010**, *641*, 136-140.

(57) Fang, C.; Agarwal, A.; Widjaja, E.; Garland, M. V.; Wong, S. M.; Linn, L.; Khalid, N. M.; Salim, S. M.; Balasubramanian, N. *Chemistry of Materials* **2009**, *21*, 3542-3548.

(58) Peng, K. Q.; Wang, X.; Wu, X. L.; Lee, S. T. *Nano Letters* **2009**, *9*, 3704-3709.

(59) Wu, Y.; Cui, Y.; Huynh, L.; Barrelet, C. J.; Bell, D. C.; Lieber, C. M. *Nano Letters* **2004**, *4*, 433-436.

(60) Zhang, R. Q.; Lifshitz, Y.; Ma, D. D. D.; Zhao, Y. L.; Frauenheim, T.; Lee, S. T.; Tong, S. Y. *Journal of Chemical Physics* **2005**, *123*.

(61) Arslan, I.; Yates, T. J. V.; Browning, N. D.; Midgley, P. A. *Science* **2005**, *309*, 2195-2198.

(62) Kurner, J.; Frangakis, A. S.; Baumeister, W. *Science* **2005**, *307*, 436-438.

(63) Janssen, A. H.; Yang, C. M.; Wang, Y.; Schuth, F.; Koster, A. J.; de Jong, K. P. *Journal of Physical Chemistry B* **2003**, *107*, 10552-10556.

(64) Bermond, J. M.; Metois, J. J.; Egea, X.; Floret, F. *Surface Science* **1995**, *330*, 48-60.

(65) Qiao, Y. H.; Wang, D.; Buriak, J. M. *Nano Letters* **2007**, *7*, 464-469.

(66) Sharma, S.; Kamins, T. I.; Williams, R. S. *Applied Physics A-Materials Science & Processing* **2005**, *80*, 1225-1229.

(67) Aizawa, M.; Buriak, J. M. *Journal of the American Chemical Society* **2006**, *128*, 5877-5886.

Chapter 4

Epitaxial Growth of Nanostructured Gold Films on Germanium under Ambient Conditions

4.1. Introduction

While most of the galvanic displacement literature has focused upon silicon, there is a growing interest in the metallization of germanium for a number of applications. For example, the very high mobility of both electrons and holes and the lower band gap of germanium substrates make the material ideally suited for the formation of high-speed circuits.[1-5]

With respect to galvanic displacement, metals-on-germanium have been studied thus far from both a fundamental synthetic perspective, and for applications such as surface enhanced Raman spectroscopy (SERS).[6-8] Carraro and co-workers showed in 2002 that gold-on-germanium films prepared *via* a galvanic displacement route result in very well-adhering films, and this observation, coupled with XPS evidence, suggest formation of a chemical bond at the interface between the metallic gold and the germanium.[9] Moreover, tuning the preferred orientation (texture) of the metallic epilayer is an important factor in integrated circuit performance as a result of the electrical conductivity dependence on interconnect microstructure (e.g. defects, voids, internal stress).[10]

To date, however, there is little new information relating to the nature of this chemical bonding, whether there is perhaps heteroepitaxial film formation, or the presence of intermetallics, both of which are observed in the gold-on-silicon case. In this chapter, we carry out detailed X-ray diffraction measurements and cross-sectional transmission electron microscopic (TEM) analyses to identify the nature of the gold-on-germanium interface, and demonstrate that under certain conditions, the films are heteroepitaxial.

4.2. Results and *Discussion*

The synthesis of gold films on germanium surfaces was carried out by the immersion of the germanium substrate in an aqueous gold salt solution at room temperature, as shown in Scheme 4.1. As is the case with all galvanic displacement reactions, the deposition process depends upon spontaneous redox reactions occurring between the semiconductor surface and the metal ions in the solution. As a result of the sufficiently high reduction potential of gold ions ($E^o_{Au^{3+}/Au^o} = +1.42$ V vs. NHE), the process leads to oxidation of the germanium surface that is supplying the electrons to reduce the gold ions to metallic gold on the surface, according to the following set of equations (1, 2): [9]

Anodic: $Ge \rightarrow Ge^{4+} + 4\,e^-$ $E^o_{Ge^{4+}/Ge} = 0.12$ V vs. NHE (1)

Cathodic: $Au^{3+} + 3\,e^- \rightarrow Au^o(s)$ $E^o_{Au^{3+}/Au^o} = +1.42$ V vs. NHE (2)

During the galvanic displacement process, and as a result of the oxidation of germanium surface, two germanium oxide products are formed; germanium dioxide "GeO_2" and germanium suboxide "GeO_x ($x < 2$)", as outlined in Scheme 4.1. GeO_2 is water soluble (5.0 g/l at 25° C).[11, 12] However, studies of the oxidation of hydrogen terminated germanium in water have shown evidence for the simultaneous formation and dissolution of GeO_2, leaving GeO_x ($x < 2$) covering the surface.[13] Recent studies have shown that germanium oxides, GeO_2 and GeO_x, are soluble in aqueous solution of NH_4OH, HCl, or HF.[14-17] The solubility of germanium oxides was found to increase with increasing HF concentration.[17, 18]

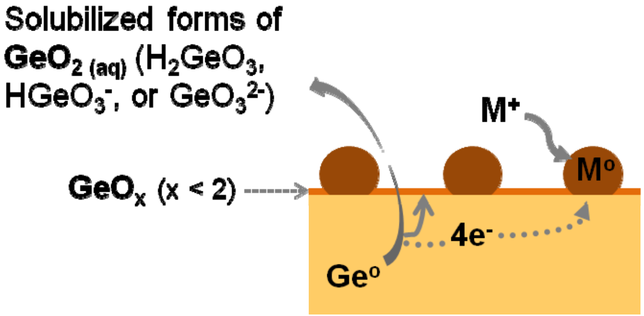

Scheme 4.1. *Galvanic displacement process on germanium: the surface acts as the reducing agent and the electron source for the reduction of metals salts. As a result of the corrosion of germanium substrate, germanium oxides, GeO_2 and GeO_x ($x < 2$), are formed; only GeO_2 is then solubilized in water as the suboxides are insoluble under these conditions.*[13, 19]

The formation of a gold film on the surface of a Ge(111) wafer shard after 20 min immersion in 0.1 mM $KAuCl_4$ (aq) at room temperature is shown in the plan view SEM image in Figure 4.1a. The germanium surface is covered with 3D gold islands of ~20 nm in thickness as revealed from the cross-sectional SEM image (Figure 4.1b). The oxidation of the germanium surface results in the formation of various forms of germanium oxide, of which GeO_2 is water soluble.[11-13] In contrast with silicon, whose oxide requires the presence of a fluoride ion source to assist in its dissolution, studies of galvanic displacement on germanium have been carried out both in its presence[9] and absence[6-8, 20-25]. When galvanic displacement is carried out under the same conditions, but in the presence of 20% HF (aq), there are no significant differences in film thickness and morphology (compare the SEM images in Figures 4.1a and 4.b, with Figures 4.1c and 4.d). Even higher concentrations of HF (aq) of 40% look similar (*vide supra*). Thus by SEM analysis, the conclusion would be that HF has little effect on the metallization of germanium, under these conditions.

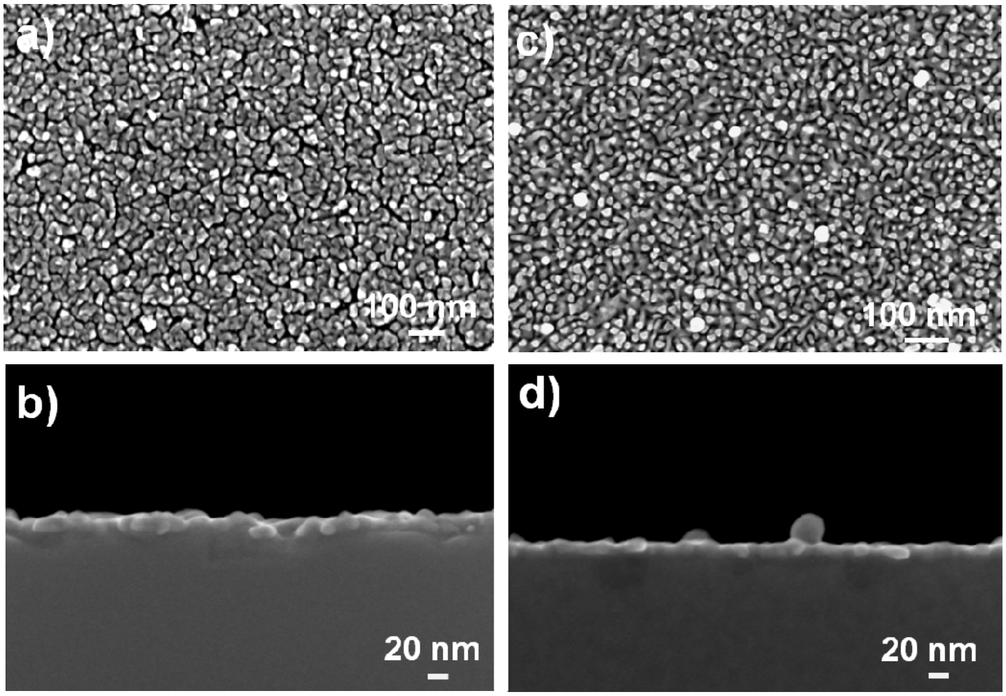

Figure 4.1. *Scanning electron micrographs (SEM) for Au films galvanically deposited on Ge(111) after 20 min immersion of germanium shards in solutions containing 0.1 mM* $KAuCl_4$ *(aq) (a, b) and 0.1 mM* $KAuCl_4$ *+ 20% HF (aq) (c, d). (a, c) and (b, d) are plan view and cross-sectional images, respectively.*[19]

While SEM is understandably the most commonly used method for characterization,[26-35] it can be deceptive as is found in this work – seemingly similar metal-on-semiconductor films (by SEM) may have very different crystallinities and relative orientations (*vide infra*). As a result, it is critical to understand the growth of the metallic films with regards to their crystallinity (are they amorphous, or poly- and single crystalline?) and to investigate the interfacial characteristics (crystal orientation, film texture, composition of the metal-semiconductor interface, etc) by complementary means.[36, 37] In this study, we describe the use of a number of different X-ray diffraction (XRD) analyses, as well as high resolution TEM and nanobeam (~5 nm) selected area electron diffraction (SAED) imaging to better illuminate the nature of these films.

While well known to the reader, a schematic diagram of the experimental XRD set-up is shown (Figure 4.2) to clearly define the various angles that will be manipulated to produce two dimensional (2D) frames, pole figures, θ–2θ scans and rocking curves for data obtained from a series of gold-on-germanium samples prepared *via* galvanic displacement. When examining these samples *via* XRD, a 2D X-ray diffraction system is advantageous because it allows the acquisition of 2 theta (2θ) X-ray Bragg diffractions over a wide range of chi (χ) angles simultaneously.[38, 39] Hence, a large fraction of diffraction rings is measured simultaneously, important for samples with a preferred orientation and texture, and therefore yielding more information than one dimensional sampling.[38, 39]

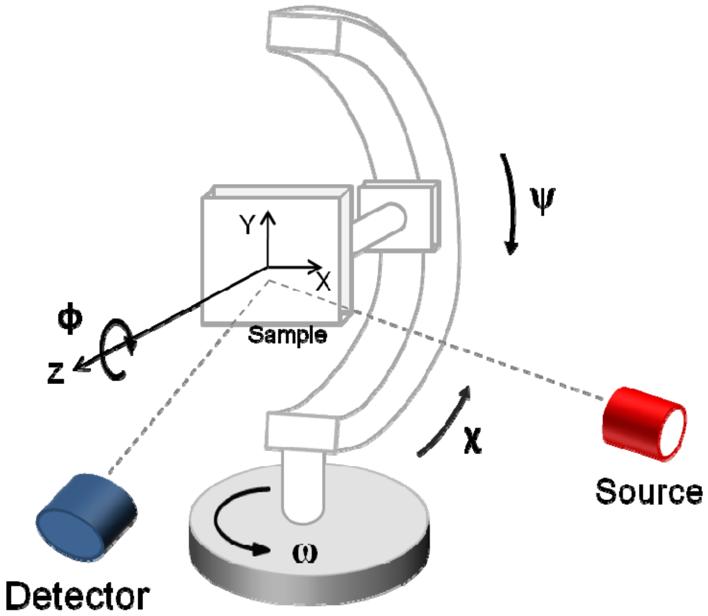

Figure 4.2. *Schematic diagram showing the experimental set up used in the in- and out-of-plane orientation analyses by X-ray diffraction. The pole figure was constructed by rotating the sample 360^o along the azimuthal axis "Φ" at different chi "χ" angles; $\chi = 90^o - \psi$. The sample was aligned vertically as shown in the figure at $\psi = 90^o$ ($\chi = 0^o$). The rocking curves were measured by fixing the detector position at the required 2θ and rocking the sample along the ω axis.*[19]

Figures 4.3a to 4.3j represent the XRD 2D frames, acquired while probing the films out-of-plane orientation by θ-2θ scans, for gold-on-germanium samples prepared under similar conditions, varying only the concentration of HF (aq). The samples were prepared by immersing a Ge(111) substrate for 20 minutes in 0.1 mM $KAuCl_4$ (aq) at room temperature and increasing the concentration of HF (aq) from 0% to 40%. Figure 4.4 shows SEM micrographs observed for gold films prepared under the same conditions for Figure 4.3. In Figure 4.3, within the 2D frame, diffraction patterns from different families of gold planes diffracting in the 2θ range of 27.6 - 62.4° are shown.

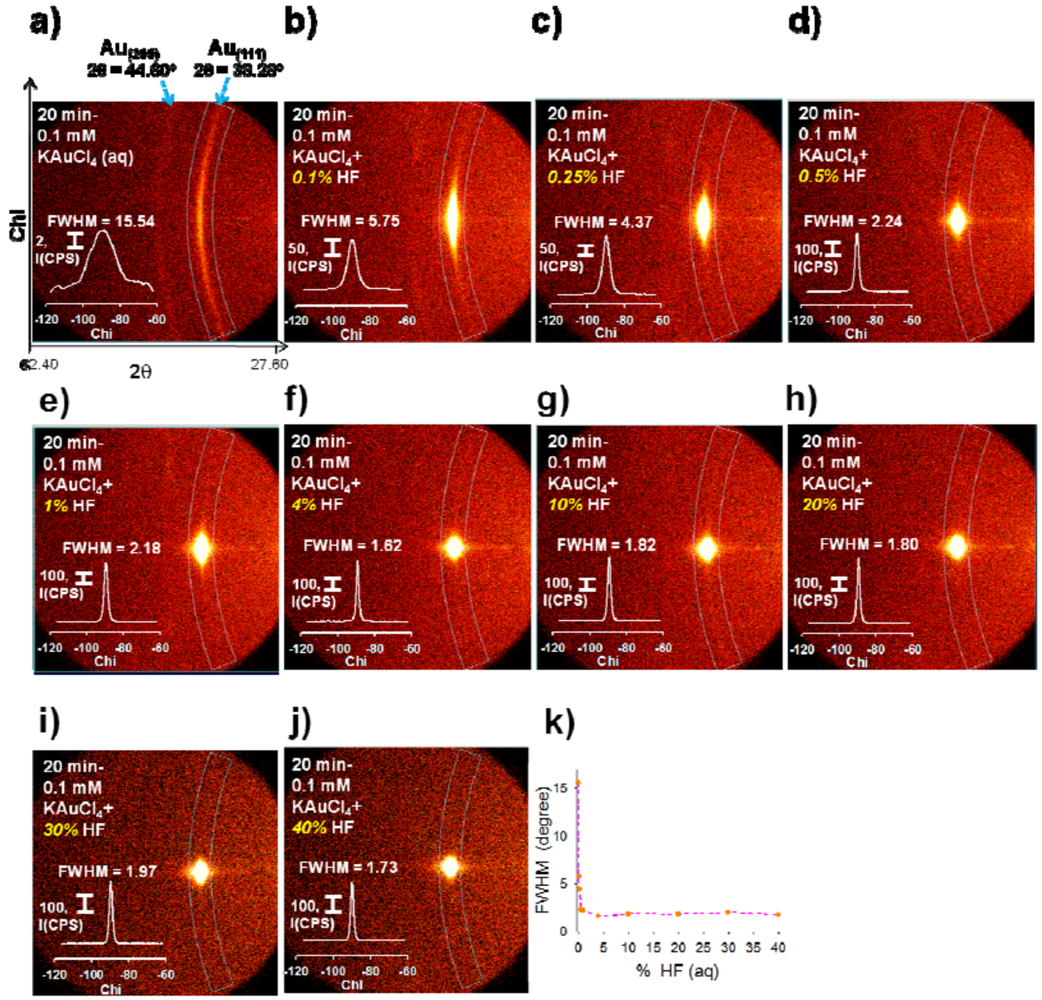

Figure 4.3. *XRD 2D frames obtained for gold galvanically deposited on germanium surfaces. The gold films are formed after a 20 min immersion of Ge(111) shards in 0.1mM $KAuCl_4$ (aq) + x% of HF (aq): (a) x = 0, (b) x = 0.1, (c) x = 0.25, (d) x = 0.5, (e) x = 1, (f) x = 4, (g) x = 10, (h) x = 20, (i) x = 30, and (j) x = 40. The inset white peaks show the (I- χ) plots, representing the diffraction intensities at 2θ = 38.28°, Au(111), along with χ. (k) The plot shows the change of the FWHM values of the (I- χ) peaks with HF concentrations.*[19]

The expected diffraction from a family of planes of a polycrystalline film with random orientation would show uniformly distributed intensity along the Debye diffraction ring.[40] Localized high intensity diffraction patterns of spots located along the ring, however, are diffractions that result from a preferred orientation of the gold film (*vide infra*).[40] The diffractions observed in the form of tightened, or less dimensional Debye diffraction rings in 2D XRD frames are a result of highly ordered film; large fraction of the film grains are oriented parallel to the substrate surface. At $\chi = 0$, at the ring central position, diffractions are observed from planes that are parallel to the substrate surface. However, on going away from the ring central position ($\chi > 0$), diffractions are observed from planes that are tilted with the same chi angle in respect to the substrate surface.

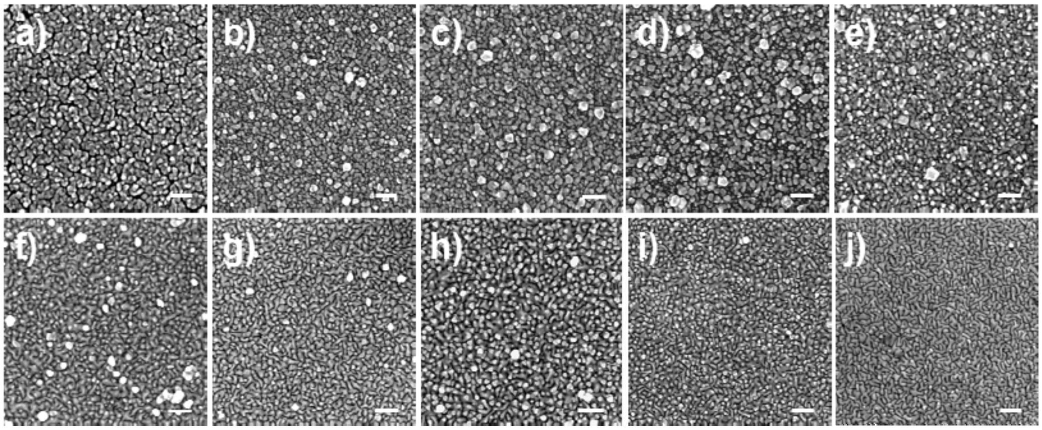

Figure 4.4. *Plan view scanning electron micrographs for gold galvanically deposited on germanium surfaces. The gold films are formed after a 20 min immersion of Ge(111) shards in 0.1 mM* $KAuCl_4$ *(aq) + x% of HF (aq); (a) x = 0, (b) x = 0.1, (c) x = 0.25, (d) x = 0.5, (e) x = 1, (f) x = 4, (g) x = 10, (h) x = 20, (i) x = 30, and (j) x = 40. The scale bars correspond to 100 nm.*[19]

As can be seen from Figures 4.3a-j, there is an obvious effect of HF (aq) concentration over the range of 0-40%, based upon the XRD 2D frame analyses for gold-on-germanium. Starting with the case of 0% HF (aq), shown in Figure 4.3a, two Debye diffraction rings are observed at $2\theta = 38.28^{\circ}$ and 44.60° that correspond to Au(111) and Au(200) planes, respectively.[41] The Au(111) ring is of higher intensity than the Au(200) ring. Moreover, the intensity of the Au(111) ring is not uniformly distributed and is somewhat concentrated towards the centre as shown in the inset for the intensity versus chi (χ) plot (FWHM = 15.54°), pointing to some degree of orientation of the grown gold film (having some fiber texture). The presence of even low concentrations of HF (aq) results in the obvious transformation of the Debye diffraction patterns from rings into spots, indicating the formation of a highly ordered (textured) gold film.

The inset intensity-chi (I-χ) peaks in Figure 4.3 represent plots of the diffraction intensity at $2\theta = 38.28^{\circ}$, the Au(111) plane, versus chi (χ). The FWHM of the inset plots can be used to represent the diffraction on the χ scale and to give an indication of the degree of orientation. When these FWHM measurements are plotted (Figure 4.3k) versus the % of HF (aq), it can be seen that the FWHM drops from 15.5° at 0% HF (aq) to 1.7° at 40% HF (aq), respectively. The greatest drop is seen from 0% HF (aq) to 0.1% (HF), indicating that even small amounts of HF (aq) are playing a critical role in the deposition process. Higher concentrations of HF (aq) do result in an increased tightening of the FWHM, but only to a small degree. Since a small FWHM within the intensity-χ plots reveals a greater degree of ordering of the Au(111) planes with respect to the Ge(111) surface plane, it can be seen that HF (aq) is resulting in ordering of the metallization on the germanium surface. Such effect may be a result of the continuous etching of the isolating germanium oxide layer during the galvanic displacement process, allowing for direct contact of the gold lattice with the underlying Ge lattices and resulting in more Au(111) planes parallel to the germanium surface.

Bragg diffractions constructing θ-2θ diffractograms result from a contribution of lattice planes that are oriented parallel to the substrate surface.[37] XRD out-of-plane investigations are essential in defining the family of planes, {hkl}, which are oriented parallel to the substrate and, equivalently, the family of directions, <hkl>, which are parallel to the substrate surface normal. XRD θ-2θ scans probing the out-of-plane orientation of the grown gold film, shown in Figure 4.5, are observed by integrating the intensity of diffraction patterns observed from diffraction frames covering a 2θ scale in the range of 2.5-112º, acquiring diffractions from all gold planes. In the absence of HF (aq), with 0.1 mM $KAuCl_4$ (aq) (Figure 4.5a), five peaks are observed for Au on Ge(111) at $2\theta = 38.28^{\circ}$, 44.60º, 64.80º, 77.63º, and 82.35º, which correspond to Au(111), Au(200), Au(220), Au(311), and Au(222), respectively.[41] The intensity ratio of Au(111) to Au(200) planes is 11.80, which is about one order of magnitude greater than the value of 1.33 observed for powder diffraction (JCPDS tables).[41] The high intensity ratio points to the oriented nature of the gold film on the germanium surface (fiber textured): The gold film has grown with a large fraction of (111) planes parallel to the Ge(111) surface.

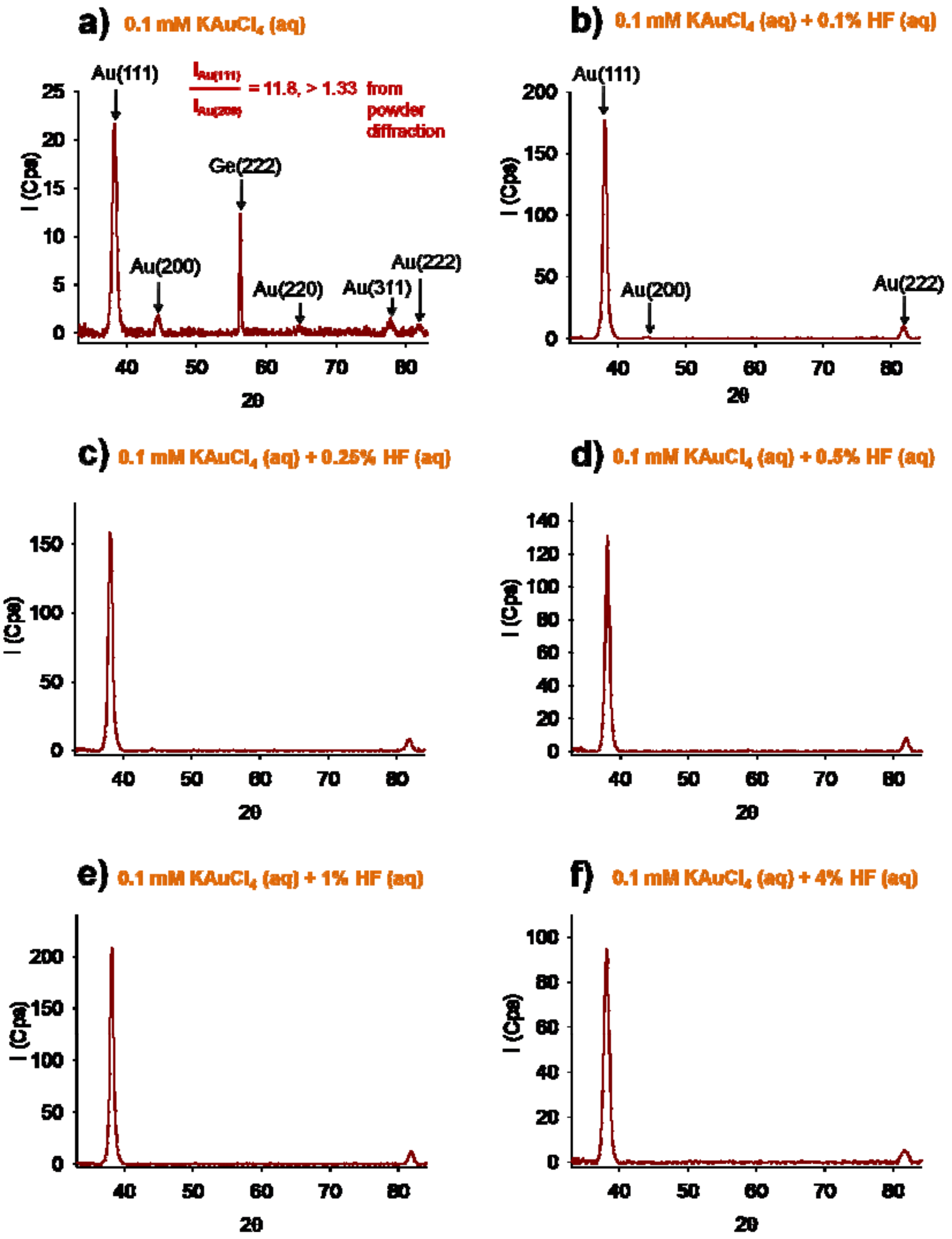

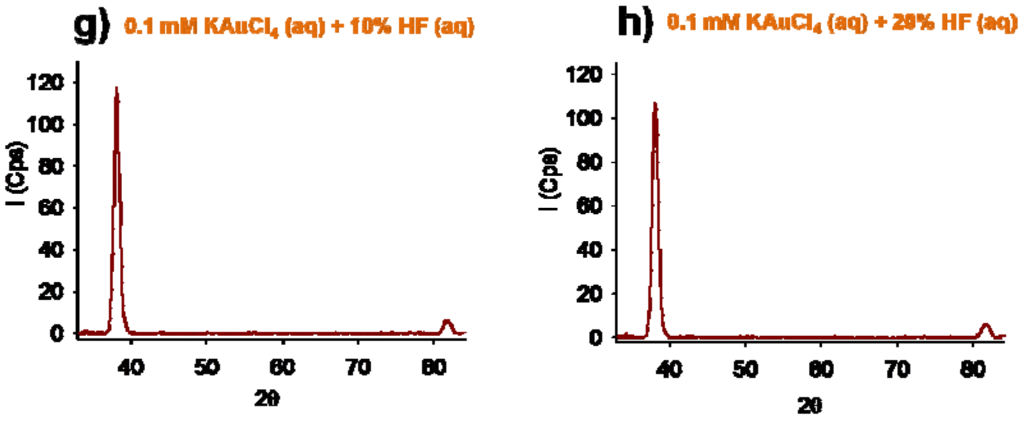

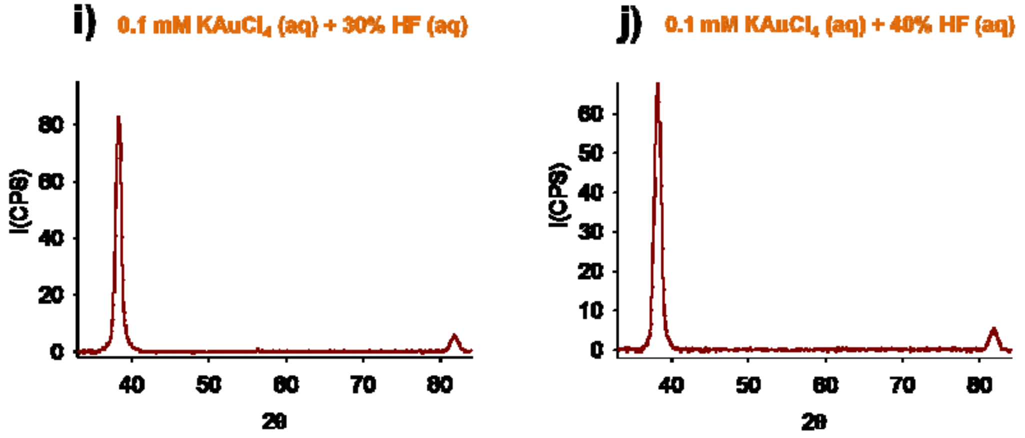

Figure 4.5. *XRD θ–2θ scan probing the out-of-plane orientation of gold films on Ge(111). The gold films were prepared after a 20 min immersion of the germanium substrate in a mixture of 0.1 mM $KAuCl_4$ (aq) + x% of HF (aq): (a) x = 0, (b) x = 0.1, (c) x = 0.25, (d) x = 0.5, (e) x = 1, (f) x = 4, (g) x = 10, (h) x = 20, (i) x = 30, and (j) x = 40.*[19]

When 0.1% HF (aq) is added to the deposition solution of 0.1 mM $KAuCl_4$ (aq), the Au(220) and Au(311) peaks vanish, leaving only the Au(111), Au(200) and Au(222) features (Figure 4.5b). In the case of HF (aq) concentrations higher than 0.25% (Figures 4.5d-j), the Au(200) peak disappears, leaving only the Au(111) and Au(222) peaks, indicating the formation of highly textured gold films on the germanium surfaces. To summarize, a Au(111)//Ge(111) out-of-plane orientation relationship is obvious in all the gold-on-germanium samples, but those with greater concentrations of HF (aq) are clearly more highly textured.

While it may be stated that the out-of-plane <111> crystallographic directions of most of the gold film crystallites are aligned parallel to the surface normal (texture axis), the crystalline orientation may (or may not) be randomly distributed in the azimuthal direction (in-plane orientation, *vide infra*), as shown schematically in Figure 4.6.[42] Fiber texture crystallites are characterized by their one degree of orientational freedom, which is the angle of rotation around the texture axis (Figure 4.6).[37]

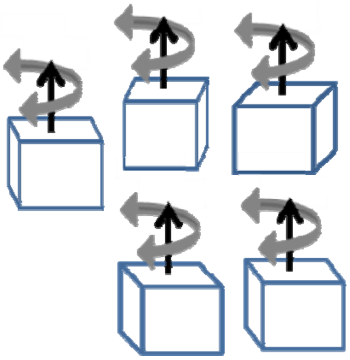

Figure 4.6. *Schematic of fiber textured crystals. The grains are aligned along the vertical (black) texture axis, while they are randomly oriented around the azimuthal (grey) axis.*[19]

Further proving the fiber texture nature of the gold film grown on Ge(111) from an aqueous gold salt deposition bath requires investigating the in-plane orientation of the Au crystallites. Pole figure analysis provides in-plane information by collecting diffraction intensities while rotating a sample azimuthally 360° along the rotation axis (Φ) at different tilting angles (χ), and setting 2θ constant at the value for the plane of interest (Figure 4.6).[37] Pole figures can differentiate between the three types of texture: random, fiber, and epitaxial. These three textures result in featureless pole figures, a ring pattern surrounding the pole figure central point, and defined spots at certain (Φ, χ) positions on the pole figure, respectively.[43]

Figures 4.7a and 4.7b show the germanium (111) surface and contour pole figures, respectively, which were obtained by setting 2θ = 27.31° for the (111) planes of germanium single crystal substrate and acquiring Bragg diffractions while rotating the sample along the substrate in-plane "azimuthal" direction at different tilting chi angles. In these figures, the spot (peak) observed at χ = 0° corresponds to diffractions acquired from the Ge {111} planes parallel to the substrate surface.[44] At χ = 70.5°, the observed three equally spaced (ΔΦ = 120°) diffractions spots (peaks) arise from the next set of (111) reflections in the face centered cubic (fcc) crystal structure.[45, 46] The locations of the three peaks agree with the calculated χ = 70.5° that corresponds to the angle between the (111) plane and each of the $(\bar{1}11)$, $(1\bar{1}1)$, and $(11\bar{1})$ planes in the cubic system (see Figure 4.8).[46]

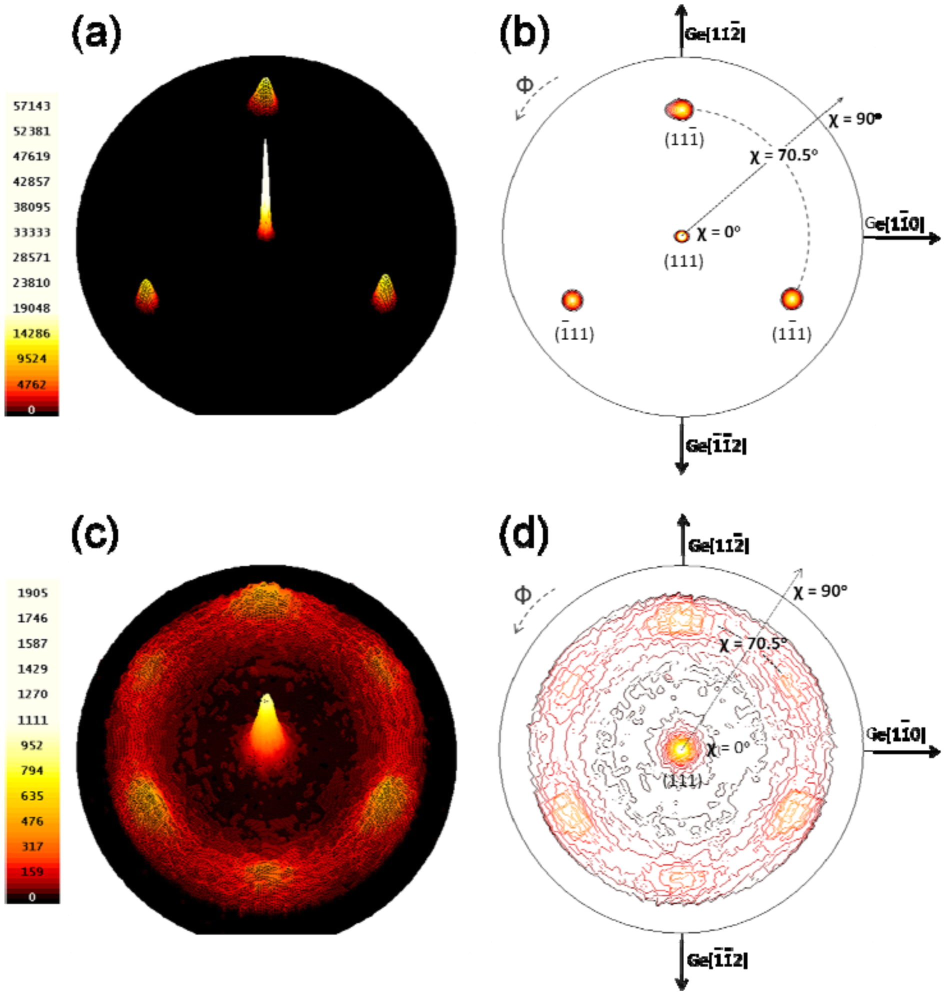

Figure 4.7. *(111) X-ray pole figures for Ge(111) substrate (a, b) and Au film, on a Ge(111) substrate, produced after a 20 min immersion of the germanium substrate in 0.1 mM* $KAuCl_4$ *(aq) (c,d). The (111) surface and contour pole figures are represented in (a, c) and (b, d), respectively. The pole figures were obtained by setting* 2θ *equals to the angle of diffraction from the (111) planes (*$2\theta = 27.31^o$ *and* 38.28^o *for Ge and Au, respectively) and collecting the diffraction intensity while rotating the sample azimuthally at different tilting angles (χ).*[19]

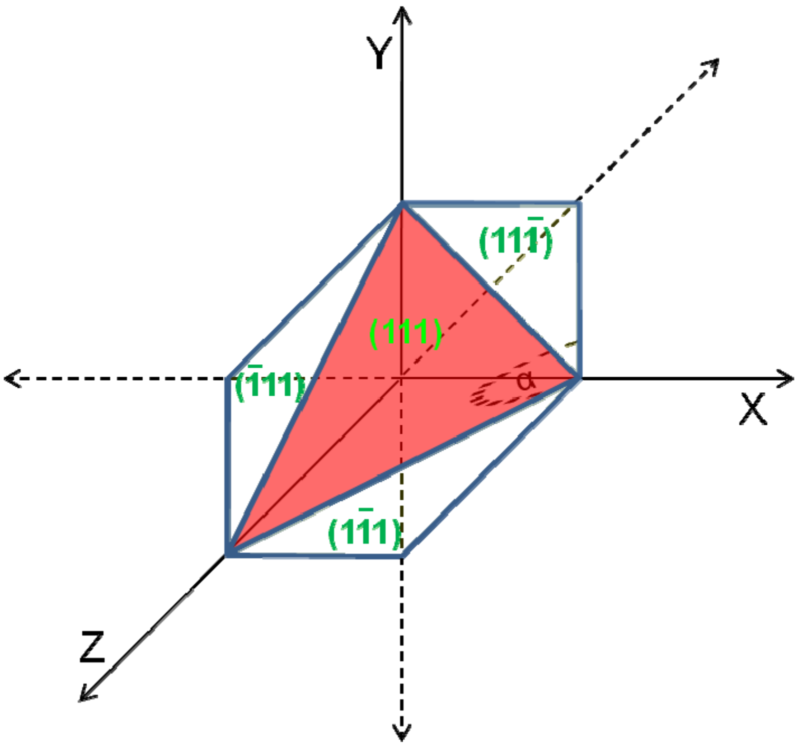

Figure 4.8. *Schematic of the (111), ($\bar{1}$11), (1$\bar{1}$1), and (11$\bar{1}$) planes of face centered cubic (fcc) structure. The angle* $\alpha = 70.5^\circ$ *represents the angle between the (111) plane and each of the ($\bar{1}$11), (1$\bar{1}$1), and (11$\bar{1}$) planes in the cubic system.*[19]

The (111) Au pole figures for a gold film grown after 20 min immersion of the germanium substrate in 0.1 mM KAuCl$_4$ (aq) in the absence of HF (aq) are shown in Figures 4.7c, and 4.7d, which were acquired by setting $2\theta = 38.28^\circ$. The diffraction peak observed at $\chi = 0^\circ$, Figure 4.7c, indicates that the <111> directions of a large fraction of gold grains are aligned normal to the substrate surface; a large fraction of Au(111) planes are parallel to the substrate surface. The ring diffraction pattern at $\chi = 70.5^\circ$ reveals diffraction from gold grains that are oriented randomly in the azimuthal, in-plane, direction (meaning that it is a fiber textured gold film as shown schematically in Figure 4.6). The pole figure analysis is a confirmation of the fiber texture behaviour indicated from the θ-2θ scan in Figure 4.5a, and the diffraction pattern in Figure 4.3a.

The θ-2θ scans shown earlier (Figures 4.5d-j) of the gold films grown from reaction mixtures containing 0.1 mM $KAuCl_4$ (aq) and HF (aq) of concentrations greater than 0.25% show diffractions from only Au(111) and Au(222), and there is no apparent difference in the out-of-plane information observed under these conditions. The pole figures can, however, help to extract more information regarding the gold-on-germanium film orientation, and in fact, show that these interfaces differ quite substantially. While investigating the in-plane orientation of a gold film grown from a solution containing 4% HF (aq) along with 0.1 mM $KAuCl_4$ (aq), the pole figure diffraction patterns (Figure 4.9a, b) indicate minor in-plane disorder as revealed from the less dimensioned ring pattern at $\chi = 70.5^\circ$. In the presence of 20% HF (aq), along with the gold salt solution in the reaction mixture, well-defined diffraction spots and peaks are observed at $\chi = 70.5^\circ$ as shown in Figures 4.9c and 4.9d. The sharpness of the Au(111) diffractions and the "clean" pole figure indicate a higher degree of alignment in the azimuthal direction, suggestive of an epitaxial gold film.

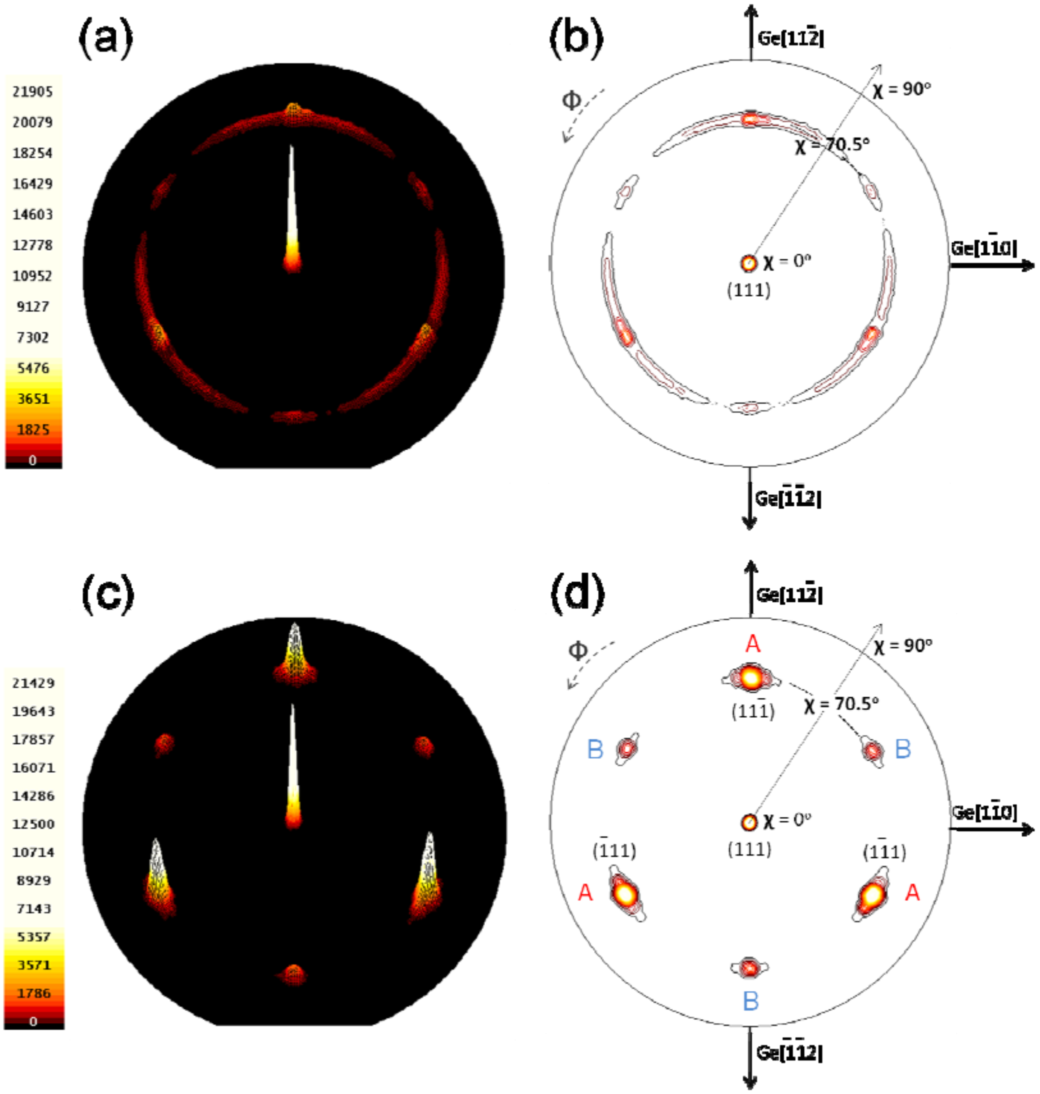

Figure 4.9. *(111) X-ray pole figures for Au films, on Ge(111) substrates, produced after a 20 min immersion of the germanium substrates in 0.1 mM* $KAuCl_4$ *(aq) solution containing 4% HF (aq) (a, b), and 20% HF (aq) (c, d). The (111) surface and contour pole figures are represented in (a, c) and (b, d), respectively. The pole figures were obtained by setting* 2θ *equals to the angle of diffraction from the Au(111) planes (*$2\theta = 38.28^{o}$*) and collecting the diffraction intensity while rotating the sample azimuthally at different tilting angles (χ).*[19]

The six peaks observed in Figure 4.9d also suggest that there are two types of epitaxy or in-plane textures for the Au/Ge(111) system. By convention, these are denoted as “A” and “B” with A peaks appearing at the same azimuthal positions as those of the Ge substrate in Figure 4.7a, while B orientation is rotated 180° relative to A with an intensity equal to ~1/5 of that of A. Hence, in the case of the A orientation, all the crystallographic directions of the gold film are coincident with those of the germanium substrate, while in the case of the B orientation the film structure is rotated 180° relative to the germanium structure. A similar A-B orientation has been observed for evaporated silver,[47] sputtered copper[48], and electrodeposited gold films on silicon surfaces. As determined from the pole figure shown in Figure 4.9d, the two epitaxial relationships for the A and B in-plane orientations are Au(111)$[11\bar{2}]$//Ge(111)$[11\bar{2}]$, and Au(111)$[\bar{1}\bar{1}2]$//Ge(111)$[11\bar{2}]$, respectively. Noticeably, in Figure 4.7c and 4.7d, these two “A and B” in-plane orientations appear to only have slight preferred alignment of all the possible random in-plane orientations.

Figure 4.10 show the (111) pole figures for gold films prepared after 20 min immersion of germanium shards in a mixture of 0.1 mM $KAuCl_4$ (aq) and 1% HF (aq) (a, b), 10% HF (aq) (c, d), 30% HF (aq) (e, f), and 40% HF (aq) (g, h). In the presence of low HF concentration (1%), the film exhibit a fiber texture nature as revealed from the diffraction ring pattern at chi = 70.5° (Figure 4.10b). However, heteroepitaxial gold films were grown on germanium surfaces in the presence of high HF concentration (Figure 4.10c-h).

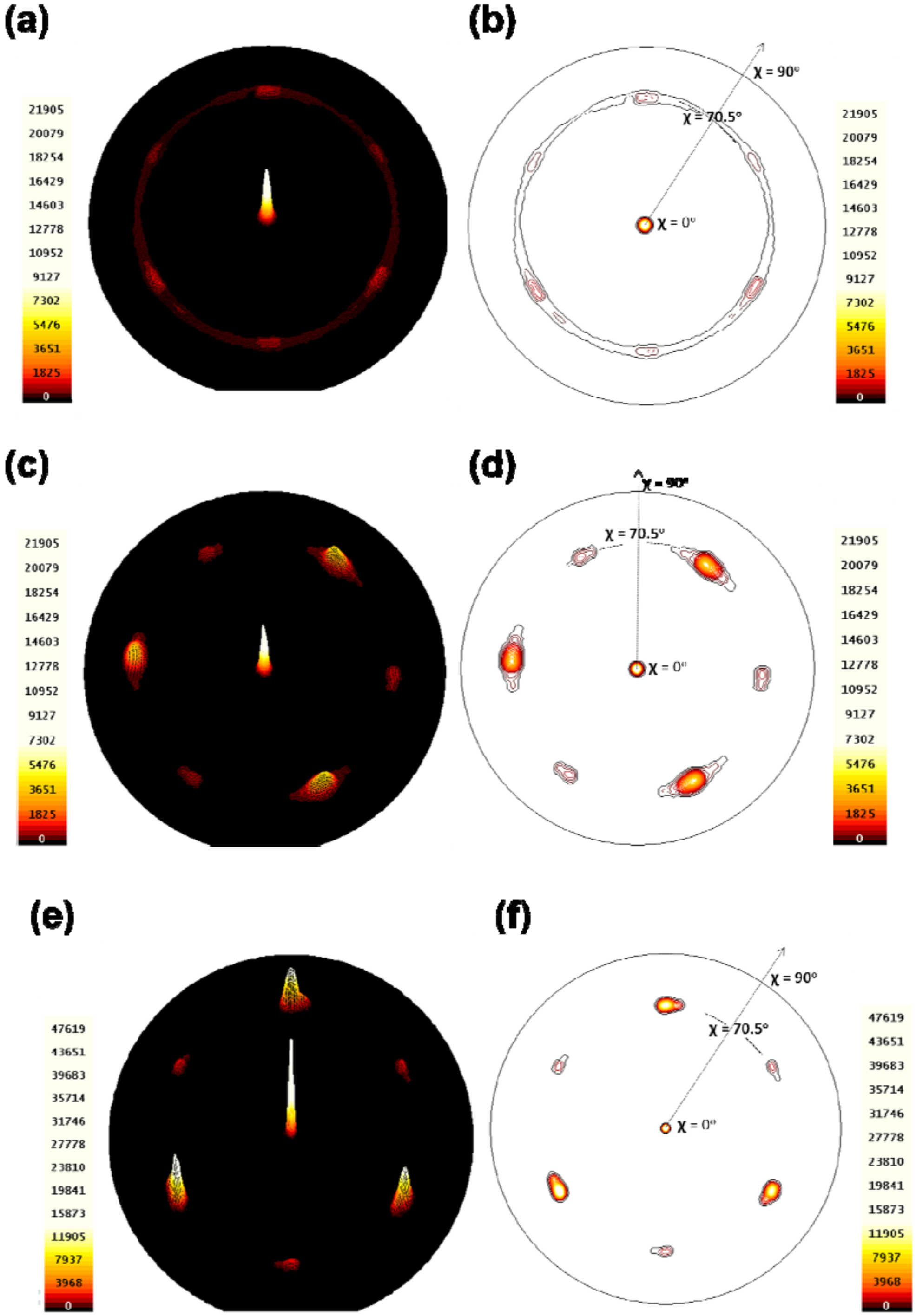
(a)
(b)
21905
20079
18254
16429
14603
12778
10952
9127
7302
5476
3651
1825
0
χ = 90°
χ = 70.5°
χ = 0°
(c)
(d)
(e)
(f)
47619
43651
39683
35714
31746
27778
23810
19841
15873
11905
7937
3968
0

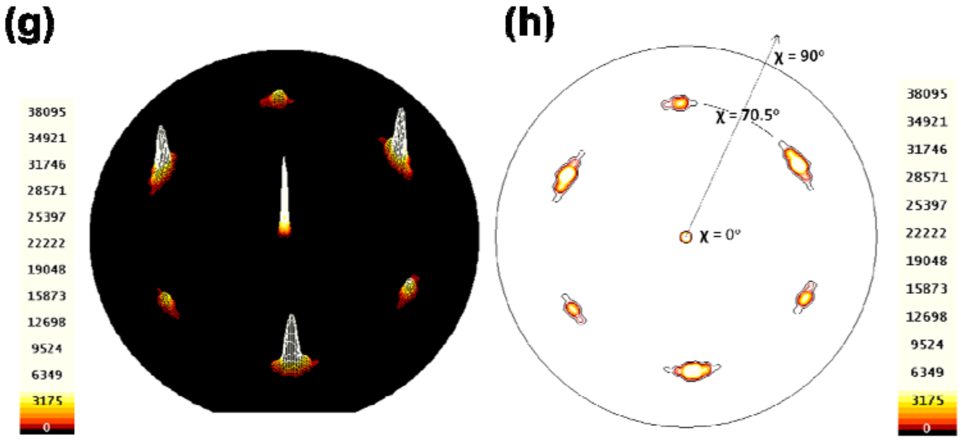

Figure 4.10. *show the (111) pole figures for gold films prepared after 20 min immersion of germanium shards in a mixture of 0.1 mM $KAuCl_4$ (aq) and 1% HF (aq) (a, b), 10% HF (aq) (c, d), 30% HF (aq) (e, f), and 40% HF (aq) (g, h).*

The concept of mosaicity has been used to describe the ideality of single crystals.[37] In the case of epitaxial film-substrate systems, mosaicity can be used to indicate the misorientation, or deviated orientation of the grains along the out-of-plane direction.[37] The out-of-plane mosaicity of the gold films on germanium was determined by X-ray rocking curves. Out-of-plane mosaicity can be investigated from rocking curves acquired by fixing the detector position at the required 2θ of the plane of interest (usually the plane with the same *hkl* out-of-plane direction) and rocking the sample along the omega "ω" axis (Figure 4.2). Figure 4.11 shows the X-ray rocking curves of a Ge(111) substrate (Figure 4.11a, 2θ was fixed at 27.31°), and Au(111) from gold films on Ge(111). Figures 4.11b and 4.11c correspond to deposition solutions of 0.1 mM $KAuCl_4$ (aq) in the absence of HF (aq), and in the presence of 20% HF (aq), respectively. In the case of Figures 4.11b and 4.11c, 2θ was fixed at 38.28°.

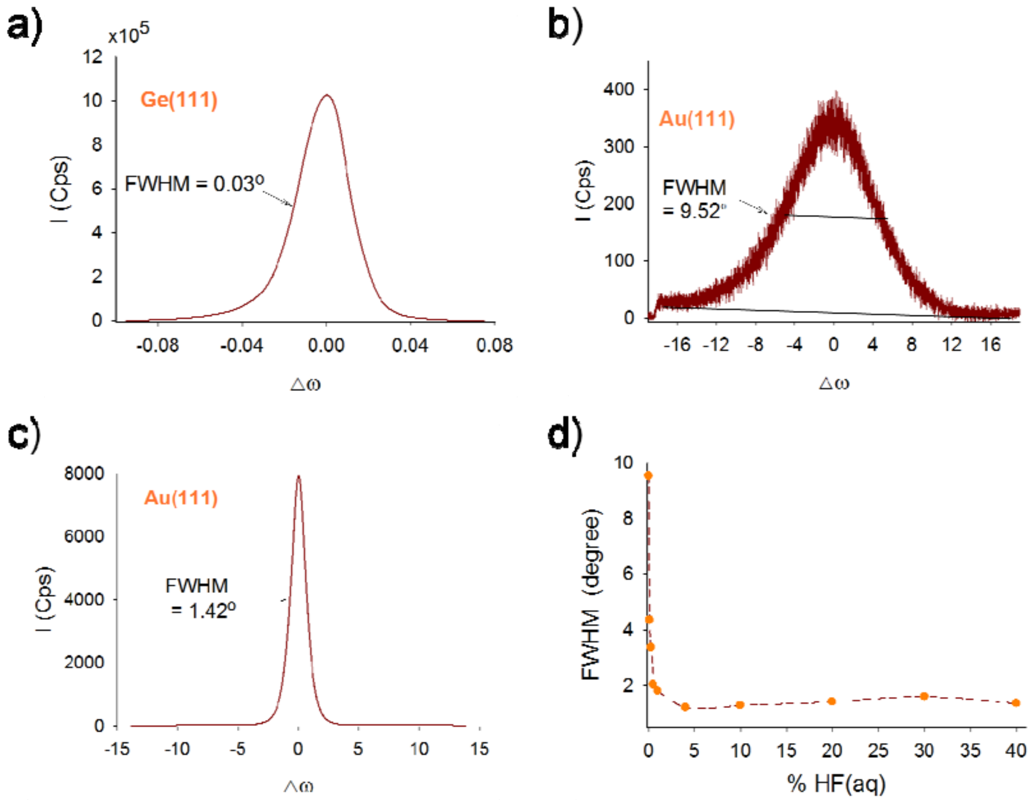

Figure 4.11. *X-ray rocking curves for Ge(111) substrate (a), Au(111) from gold films prepared after 20 min immersion of germanium substrates in 0.1 mM* $KAuCl_4$ *(aq) (b), and in a mixture of 0.1 mM* $KAuCl_4$ *+ 20% HF (aq) (c). (d) Plot shows the effect of HF (aq) concentration on the FWHM of the rocking curves.*[19]

The mosaic spread was determined from the full width at half-maximum (FWHM) of the rocking curves.[37] The FWHM of gold films grown in the presence and in the absence of 20% HF (aq) are 1.42° and 9.52°, respectively, compared to 0.03° for the germanium substrate. A plot summarizing the change in the FWHM or the mosaic spread of the gold film as a function of increasing HF (aq) concentrations is shown in Figure 4.11d. As can be clearly seen, HF (aq) is required for more ordered structures (as shown by the lower mosaic spread), which may result from the simultaneous etching of the germanium oxide products formed during the galvanic displacement processes, leading to better direct gold-germanium contact. This improved contact between the growing gold film and the underlying germanium could lead to better transfer of crystallographic “information” from the germanium to the nucleating and growing gold film, leading to a higher degree of alignment.

In order to confirm the epitaxial relationship between germanium and the resulting gold film, we harnessed the precision of transmission electron microscopy (TEM) nanobeam diffraction analyses to characterize the nature of gold-germanium interface formed *via* the galvanic displacement process. Figure 4.12a shows cross-sectional high resolution TEM image for a gold epilayer, on a single crystal Ge(111), prepared by the immersion of germanium substrate in a mixture of 0.1 mM $KAuCl_4$ (aq) and 20% HF (aq) for 20 min. Nanobeam diffraction (beam size ≈ 5 nm) patterns were taken along the $[\bar{1}12]$ zone axis from three different locations, as shown in Figure 4.12a: “1” marks the location on the germanium substrate, “2” indicates the gold-germanium interface, and “3” corresponds to the gold layer. The nanobeam diffraction patterns taken at these three spots are shown in Figures 4.12b-d. The common viewing direction “$[\bar{1}12]$” for the diffraction patterns taken from both the germanium substrate (Figure 4.12b) and the top gold layer (Figure 4.12c), is indicative of the alignment of the gold layer with the underlying germanium substrate.

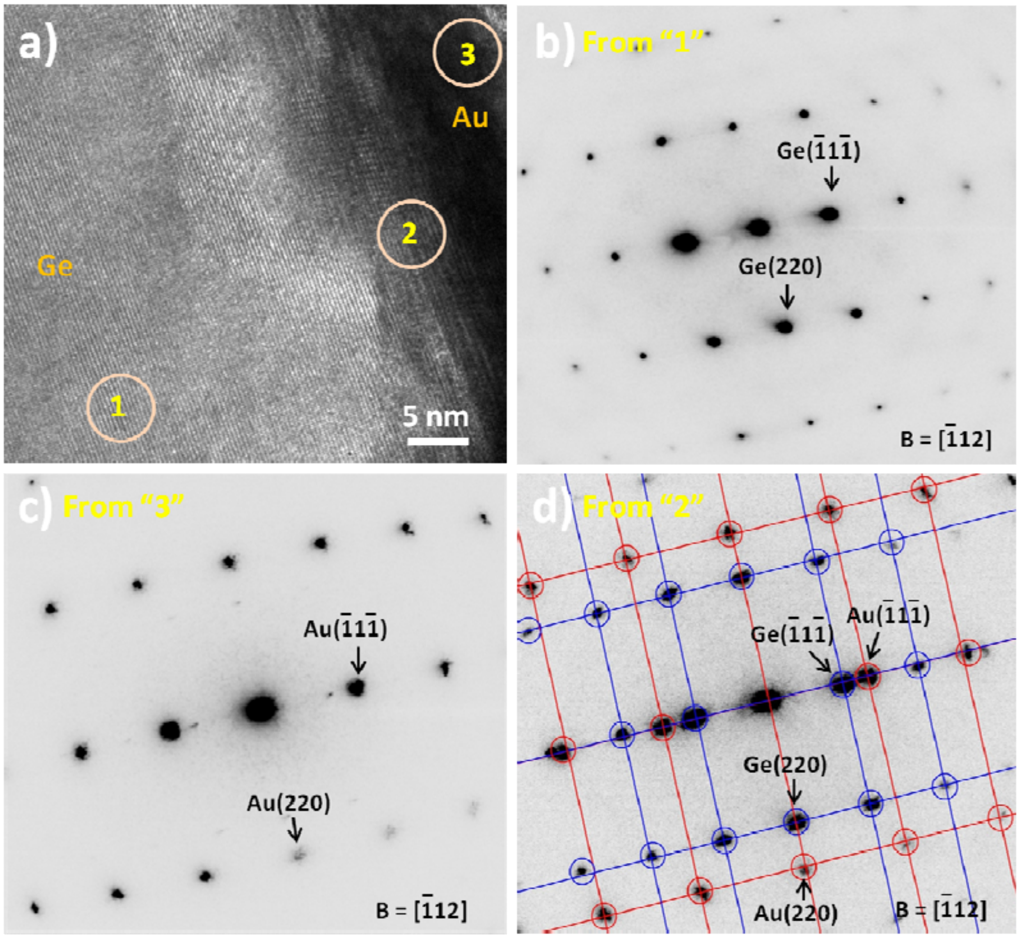

Figure 4.12. *Cross-sectional high resolution transmission electron micrograph for a gold film on Ge(111), formed by immersing the germanium substrate in 0.1 mM* $KAuCl_4$ *(aq) + 20% HF (aq) for 20 min. (b-d) Nanobeam diffraction patterns (probe ≈ 5 nm) taken along the* $[\bar{1}12]$ *zone axis from three different areas: (b) from germanium substrate (area marked 1 in image "a"), (c) from top gold area marked by 3 in image "a", and (d) from the gold-germanium interfacial area marked by 2 in image "a". Red and blue lines correspond to gold and germanium planes, respectively.*[19]

The diffraction pattern from the Au-Ge interface, Figure 4.12d, shows that along the $[\bar{1}12]$ zone axis, every Bragg diffraction spot from the germanium has a corresponding gold spot with the identical orientation. The germanium pattern consists of spots, due to its single crystal nature, arising from diffraction from the $(\bar{1}1\bar{1})$, (220) and $(13\bar{1})$ planes; gold shows diffraction from these same planes. Other features of note include the alignment of the {112} family of crystallographic planes of both the germanium substrate and the gold overlayer. The gold $(\bar{1}1\bar{1})$ and (220) planes are parallel to the germanium $(\bar{1}1\bar{1})$ and (220) planes, respectively: Au$(\bar{1}1\bar{1})$//Ge$(\bar{1}1\bar{1})$ and Au(110)//Ge(110). Hence, the nanobeam diffraction patterns from gold film on germanium substrate are strongly indicative of the Au(111)$[\bar{1}12]$//Ge(111)$[\bar{1}12]$ in-plane epitaxial relationship, which agrees with the epitaxial relationship observed from the XRD pole figure (*vide supra*, Figures 4.9c and 4.9d).

The phenomenon of heteroepitaxial crystallization involves the epitaxial growth of one layer (an epilayer) with a chemical composition and, typically, structural parameters different from those of the substrate.[49] Lattice mismatch or misfit (the disregistry of the interfacial atomic arrangement of the substrate and the overgrown epilayer) is known to have a significant effect on epitaxy.[49] Au(111) and Ge(111) with interplanar d spacings of 2.355 Å and 3.266 Å, respectively, have about a 27.9% lattice mismatch. By considering the coincident site lattice interface (CSL), however, in which three germanium lattices match with four gold lattices, $4\text{x}d_{\text{Au}(111)}$ = 9.42 Å and $3\text{x}d_{\text{Ge}(111)}$ = 9.80 Å, the lattice mismatch is only 3.8% which is also the explanation for the heteroepitaxial growth of gold on germanium (Figure 4.13). A CSL interface is most likely present for the epitaxial growth of galvanically displaced gold,[29] and electron-beam evaporated gold[50] and silver[51] on Si(111) surfaces.

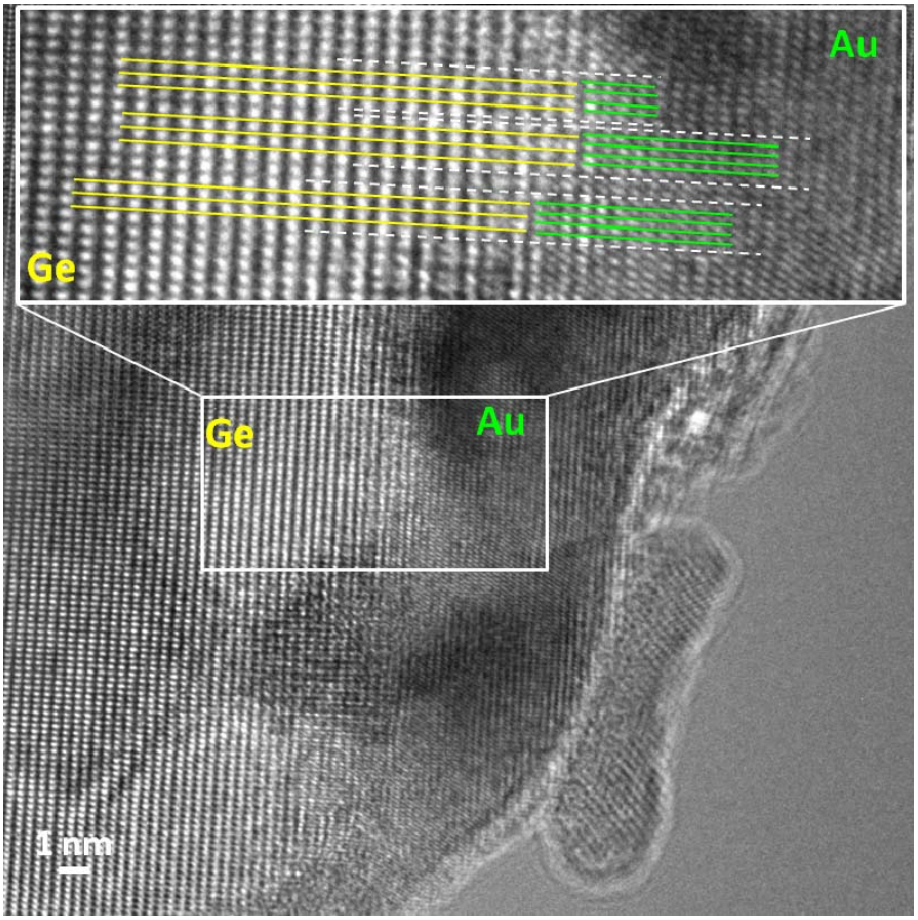

Figure 4.13. *Cross-sectional HRTEM images, for gold-germanium interface, taken close to the [110] zone axis. The yellow and green lines show the coincident site lattice interfaces for the germanium and gold planes, respectively. The white lines show the alignment and the parallel nature of the gold epilayer to the underlying germanium substrate.*[19]

The effect of immersion time on the structure and the orientation of the grown gold deposits can be revealed from the out-of-plane analyses (XRD 2D frames and θ-2θ scans). Figures 4.14 and 4.15 show the XRD 2D frames and the corresponding θ-2θ scans, respectively, for gold films grown after 30 min from deposition baths containing 0.1 mM $KAuCl_4$ (aq) and different HF (aq) concentrations, ranging from 0.1-20%. The effect of the HF concentration on the Au(111) Debye diffraction ring can be seen in Figure 4.14. Increasing the HF concentrations results in shrinking the diffraction patterns, along the chi scale, from rings to spots, indicating more ordered Au(111) planes. This phenomenon is similar to what was observed for gold films prepared after immersion of germanium shards for 20 min in the deposition solutions (Figure 4.3). The difference is that diffraction from Au(200) planes still acquired under the condition of the existence of HF concentrations up to 1% (Figure 4.14 b-e).

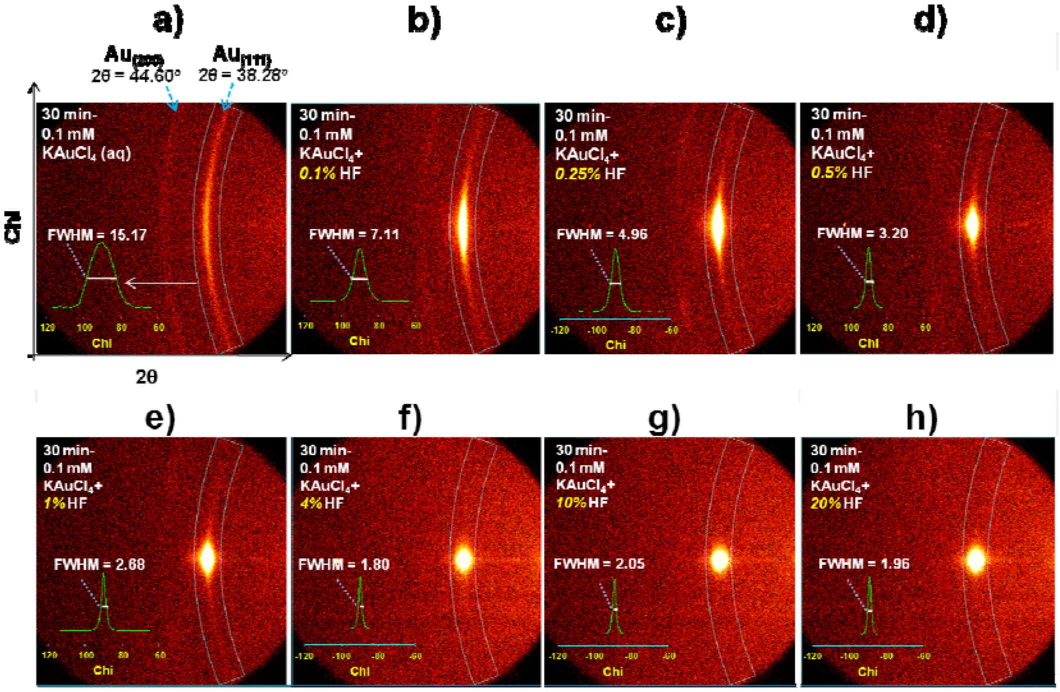

Figure 4.14. *XRD 2D frames obtained for gold galvanically displaced on germanium surfaces. The gold films are formed after a 30 min immersion of Ge(111) shards in 0.1 mM* $KAuCl_4$ *(aq) + x% of HF (aq): (a) x = 0, (b) x = 0.1, (c) x = 0.25, (d) x = 0.5, (e) x = 1, (f) x = 4, (g) x = 10, , and (h) x = 20. The inset green peaks show the (I-χ) plots, representing the diffraction intensities at* $2\theta = 38.28^o$*, Au(111), along with χ.*

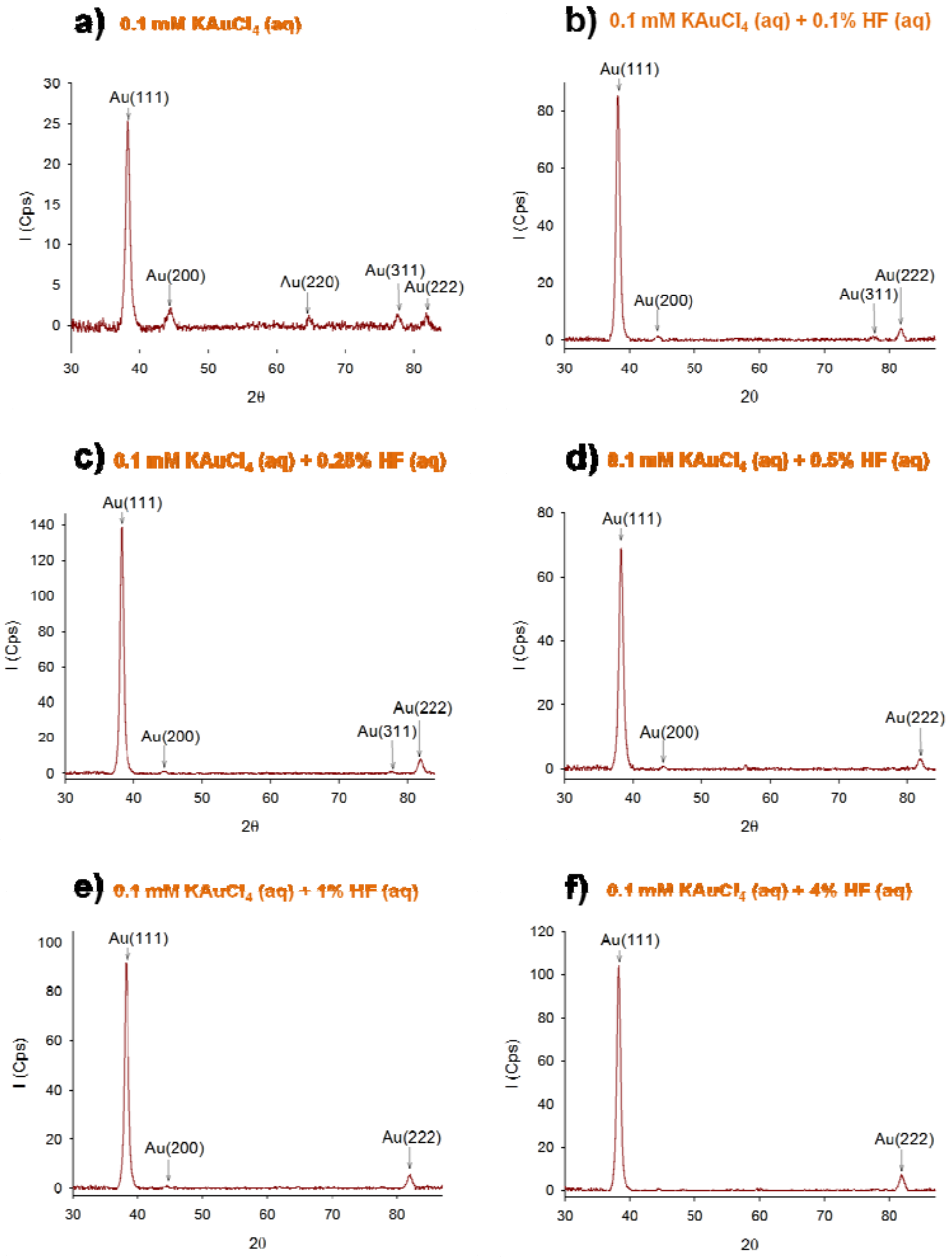

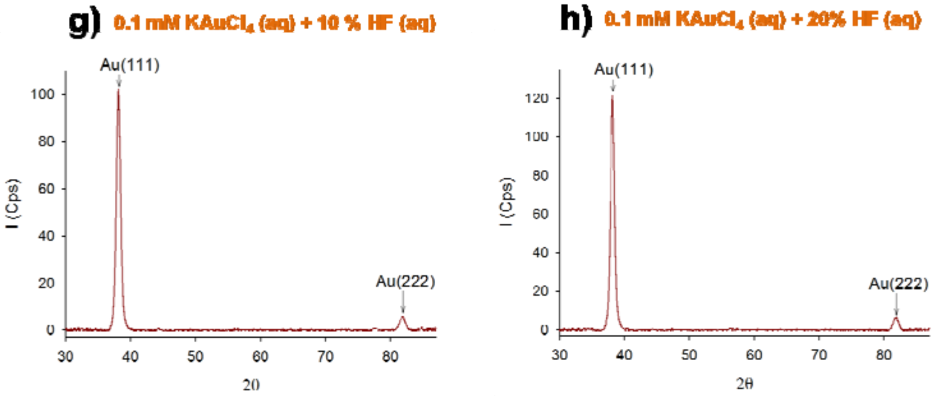

g) 0.1 mM $KAuCl_4$ (aq) + 10 % HF (aq)

h) 0.1 mM $KAuCl_4$ (aq) + 20% HF (aq)

Figure 4.15. *XRD θ–2θ scan probing the out-of-plane orientation of gold films on Ge(111). The gold films were prepared after a 30 min immersion of the germanium substrate in a mixture of 0.1 mM* $KAuCl_4$ *(aq) + x% of HF (aq): (a) x = 0, (b) x = 0.1, (c) x = 0.25, (d) x = 0.5, (e) x = 1, (f) x = 4, (g) x = 10, and (h) x = 20.*

Figures 4.16 and 4.17 show the XRD 2D diffraction frames and the corresponding θ-2θ scans, respectively, for gold films grown after 40 min from deposition baths containing 0.1 mM $KAuCl_4$ (aq) and different HF (aq) concentrations, ranging from 0.1-20%. The effect of HF on producing more ordered Au(111) planes is obvious from the shrinking of the diffraction patterns, at 2θ = 38.28°, from rings to spots with increasing the HF content in the deposition solutions (Figure 4.16b-h). However, diffraction from Au(200) and Au(311) are still acquired even in the presence of 20% HF (aq) in the reaction mixture as seen in Figures 4.16h and 4.17h. Au(200) and Au(311) planes parallel to the substrate surface were not observed at shorter immersion times, at higher HF concentrations, (*vide supra*). Hence, one can conclude that prolonged gold deposition and corrosion of germanium surfaces can result in a degree of disorientation or non preferential growth of the gold deposits.

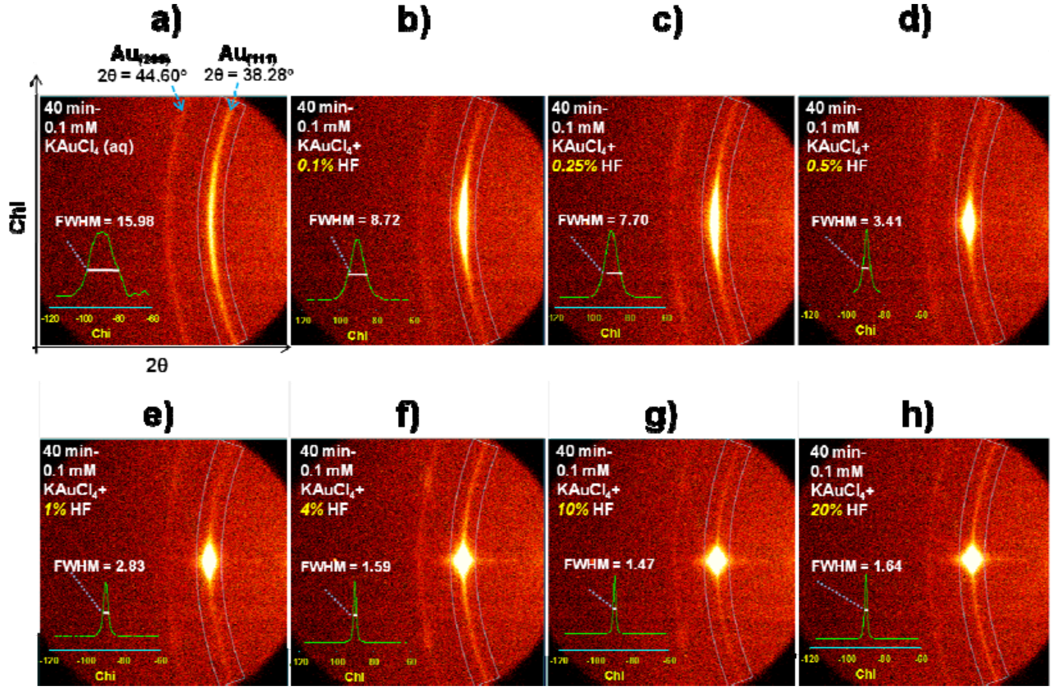

Figure 4.16. *XRD 2D frames obtained for gold galvanically displaced on germanium surfaces. The gold films are formed after a 40 min immersion of Ge(111) shards in 0.1 mM* $KAuCl_4$ *(aq) + x% of HF (aq): (a) x = 0, (b) x = 0.1, (c) x = 0.25, (d) x = 0.5, (e) x = 1, (f) x = 4, (g) x = 10, , and (h) x = 20. The inset green peaks show the (I-χ) plots, representing the diffraction intensities at* $2\theta = 38.28^o$*, Au(111), along with χ.*

a) 0.1 mM $KAuCl_4$ (aq)

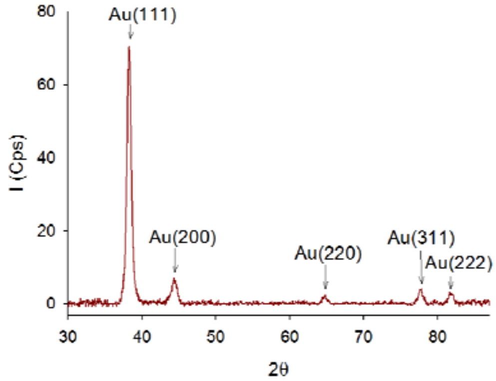

b) 0.1 mM $KAuCl_4$ (aq) + 0.1% HF (aq)

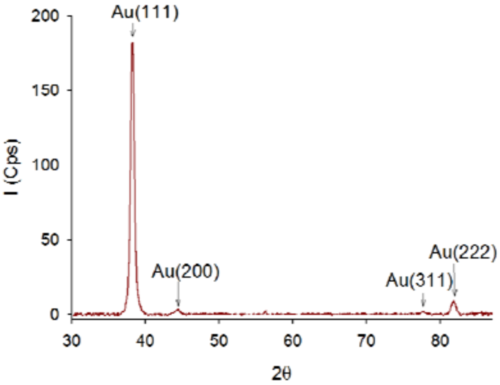

c) 0.1 mM $KAuCl_4$ (aq) + 0.25% HF (aq)

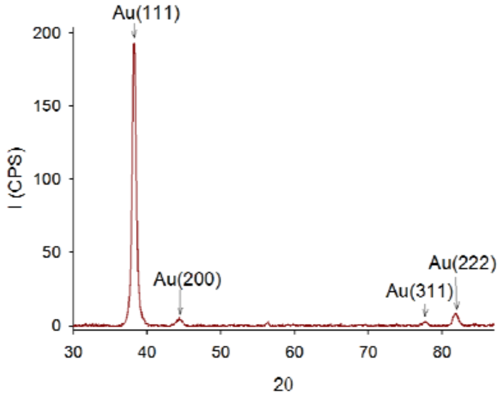

d) 0.1 mM $KAuCl_4$ (aq) + 0.5% HF (aq)

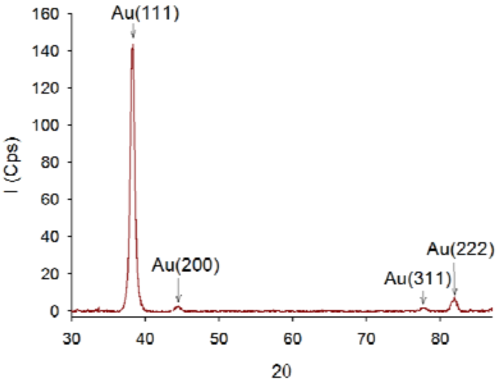

e) 0.1 mM $KAuCl_4$ (aq) + 1% HF (aq)

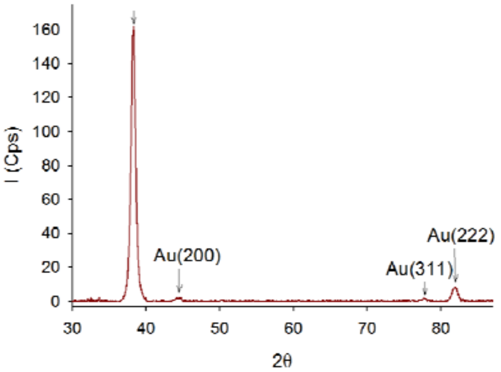

f) 0.1 mM $KAuCl_4$ (aq) + 4% HF (aq)

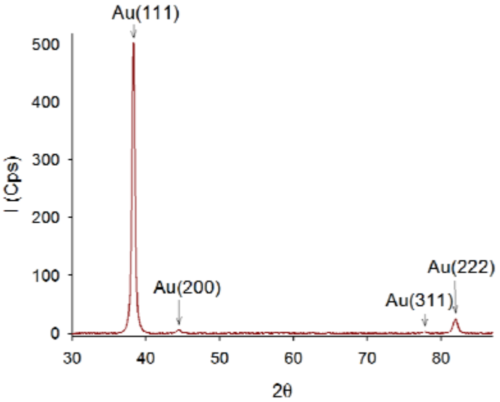

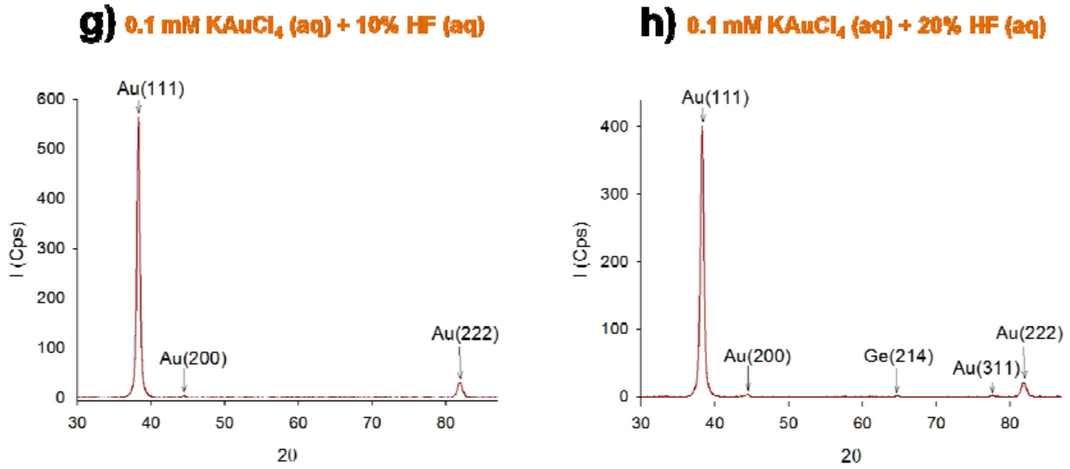

Figure 4.17. *XRD θ–2θ scan probing the out-of-plane orientation of gold films on Ge(111). The gold films were prepared after a 40 min immersion of the germanium substrate in a mixture of 0.1 mM* $KAuCl_4$ *(aq) + x% of HF (aq): (a) x = 0, (b) x = 0.1, (c) x = 0.25, (d) x = 0.5, (e) x = 1, (f) x = 4, (g) x = 10, and (h) x = 20.*

4.3. Conclusions

Galvanic displacement of germanium surfaces from aqueous solutions of gold salts resulted in oriented (fiber textured) gold films. The addition of higher concentrations of HF (aq) to the reaction mixture resulted in gold films with more ordered in-plane orientations that can be described as epitaxial in nature. The epitaxial behavior was further proved by cross-sectional TEM investigation involving nanobeam diffraction analyses. The epitaxial relationship observed from the pole figure analyses agrees with what was observed from the nanobeam diffraction pattern; Au(111)[$\bar{1}12$]//Ge(111)[$\bar{1}12$].

4.4. Experimental Section

Generalities: Unless otherwise noted, all experiments were performed under ambient laboratory conditions. Ge(111) (p-type, Ga-doped, ρ = 0.24-0.33 $\Omega\cdot$cm, 500 µm thickness) wafers were purchased from MTI Corporation. $KAuCl_4 \cdot xH_2O$ were purchased from Strem Chemicals.

Pretreatment of Germanium Substrates: All wafers were diced into 0.8 cm^2 pieces with a diamond scriber. Germanium shards were degreased in a methanol ultrasonic bath for 15 min, in boiling dichloromethane for 10 min, and then a methanol ultrasound bath for 10 min. The oxide layer was removed with a solution of NH_4OH:H_2O (1:4) for 5 min.[14, 15] After the oxide etching step, the wafers were rinsed with DI water and dried with a stream of nitrogen.

Metal Deposition: Germanium shards were immersed in either the desired aqueous gold salt solutions or the metallic salt and different concentrations of hydrofluoric acid in a Teflon beaker. After metal deposition, the sample was thoroughly rinsed with water and dried under a nitrogen stream.

Surface Characterization: The gold nanostructures on the germanium surfaces were characterized by scanning electron microscopy (SEM), transmission electron microscopy (TEM) and X-ray diffraction (XRD). SEM (Hitachi S-4800 FE-SEM) images of metallic nanostructures were typically performed with an electron energy of 20 keV. High resolution TEM (HRTEM) images and nanobeam diffraction (NBD) patterns (with a probe of ~5 nm) were recorded on a Shottky-emission 200 kV JEOL 2200FS TEM/STEM microscope with in-column energy filter equipped with a high tilt cryo-polepiece, and a cold-field-emission 300 kV Hitachi HF3300 TEM/STEM microscope with a post-column energy filter. The crystalline nature of the metallic upper layer was analyzed by X-ray diffraction (XRD). The out of plane orientation, the theta (θ)-2theta (2θ) scan, was investigated using a Bruker D8 Discover diffractometer equipped with a 1/4 Eulerian cradle, Cu X-ray tube, a 1 mm collimator, and a 2D Hi-Star proportional detector. The detector was placed 15 cm from the sample. The texture of the films and the in plane orientation were investigated using XRD pole figure analyses. To capture the whole (111) pole figure intensity distribution, the sample was tilted at different psi "ψ" angles: 90^{o}, 60^{o}, 19.5^{o}; chi "χ" = $90^{o} - \psi$ (Figure 1). At each tilting angle the sample was rotated azimuthally from phi (Φ) = 0^{o} to 360° with a 5^{o} scan step (72 frames for each ψ, Figure 2). The out of plane mosaicity was evaluated from rocking curves by fixing the detector position at the required 2θ and rocking the sample along the omega "ω" axis (Figure 2). The rocking curves were measured using scintillation counter detector.

TEM Sample Preparation on FIB: Cross-sectional TEM samples of Au/Ge(111) were prepared on a Hitachi NB5000 Focused Ion & Electron Beam System. A 40 keV Ga ion beam was used to produce a thin section about 200 nm thick, and Ar ion milling was then used for final thinning and cleaning of the surface. Ion milling was done at low temperature (with LN2 cooling) at a 6° milling angle, and with a two-step process: voltage/current of 1 kV/3 mA for thinning and 0.5 kV/3 mA for final polishing.

4.5. References

(1) Chao, Y. L.; Scholz, R.; Reiche, M.; Gosele, U.; Woo, J. C. S. *Japanese Journal of Applied Physics Part 1-Regular Papers Brief Communications & Review Papers* **2006**, *45*, 8565-8570.

(2) Nayfeh, A.; Chui, C. O.; Saraswat, K. C.; Yonehara, T. *Applied Physics Letters* **2004**, *85*, 2815-2817.

(3) Greytak, A. B.; Lauhon, L. J.; Gudiksen, M. S.; Lieber, C. M. *Applied Physics Letters* **2004**, *84*, 4176-4178.

(4) Sze, S. M. *Physics of Semiconductor Devices* Wiley: New York, 1981.

(5) Bojarczuk, N. A.; Copel, M.; Guha, S.; Narayanan, V.; Preisler, E. J.; Ross, F. M.; Shang, H. *Applied Physics Letters* **2003**, *83*, 5443-5445.

(6) Lee, K. Y.; Han, S. W.; Choi, H. C. *Bulletin of the Korean Chemical Society* **2009**, *30*, 3113-3116.

(7) Bravo-Vasquez, J.-P.; Fenniri, H. *J. Phys. Chem. C* **2009**, *113*, 12897-12900.

(8) Brejna, P. R.; Griffiths, P. R.; Yang, J. *Applied Spectroscopy* **2009**, *63*, 396-400.

(9) Magagnin, L.; Maboudian, R.; Carraro, C. *Journal of Physical Chemistry B* **2002**, *106*, 401-407.

(10) Leung, S.; Milnes, A. G.; Chung, D. D. L. *Thin Solid Films* **1983**, *104*, 109-131.

(11) Murthy, M. K.; Hill, H. *Journal of the American Ceramic Society* **1965**, *48*, 109-&.

(12) Vekhov, V. A.; Vitukhnovskaya, B. S.; Doronkina, R. F. *Izvestiya Vysshikh Uchebnykh Zavedenii, Khimiya i Khimicheskaya Tekhnologiya* **1964**, *7*, 1018-1019.

(13) Park, K.; Lee, Y.; Lee, J.; Lim, S. *Applied Surface Science* **2008**, *254*, 4828-4832.

(14) Okumura, H.; Akane, T.; Matsumoto, S. *Applied Surface Science* **1998**, *125*, 125-128.

(15) Akane, T.; Tanaka, J.; Okumura, H.; Matsumoto, S. *Applied Surface Science* **1997**, *108*, 303-305.

(16) Rivillon, S.; Chabal, Y. J.; Amy, F.; Kahn, A. *Applied Physics Letters* **2005**, *87*, 253101.

(17) Benoit, R. L.; Place, J. *Canadian Journal of Chemistry-Revue Canadienne De Chimie* **1963**, *41*, 1170-&.

(18) Sun, S. Y.; Sun, Y.; Liu, Z.; Lee, D. I.; Peterson, S.; Pianetta, P. *Applied Physics Letters* **2006**, *88*.

(19) Sayed, S. Y.; Buriak, J. M. *ACS Applied Materials & Interfaces* **2010**, *2 (12)*, 3515–3524.

(20) Aizawa, M.; Cooper, A. M.; Malac, M.; Buriak, J. M. *Nano Letters* **2005**, *5*, 815-819.

(21) Aizawa, M.; Buriak, J. M. *Journal of the American Chemical Society* **2005**, *127*, 8932-8933.

(22) Porter, L. A.; Choi, H. C.; Schmeltzer, J. M.; Ribbe, A. E.; Elliott, L. C. C.; Buriak, J. M. *Nano Letters* **2002**, *2*, 1369-1372.

(23) Porter, L. A.; Choi, H. C.; Ribbe, A. E.; Buriak, J. M. *Nano Letters* **2002**, *2*, 1067-1071.

(24) Zhang, J. G.; Gao, Y.; Hanrath, T.; Korgel, B. A.; Buriak, J. M. *Chemical Communications* **2007**, 1438-1440.

(25) Johnson, M.; Kelly, J. A.; Henderson, E. J.; Veinot, J. G. C. *IOP Conference Series: Materials Science and Engineering* **2009**, *6*, 012031/012031-012031/012035.

(26) Jim, S. R.; Taschuk, M. T.; Morlock, G. E.; Bezuidenhout, L. W.; Schwack, W.; Brett, M. J. *Analytical Chemistry* **2010**, *82*, 5349-5356.

(27) Sayed, S. Y.; Daly, B.; Buriak, J. M. *Journal of Physical Chemistry C* **2008**, *112*, 12291-12298.

(28) Liu, C.; Shields, P. A.; Denchitcharoen, S.; Stepanov, S.; Gott, A.; Wang, W. N. *Journal of Crystal Growth* **2007**, *300*, 104-109.

(29) Sayed, S. Y.; Wang, F.; Mallac, M.; Meldrum, A.; Egerton, R. F.; Buriak, J. M. *ACS Nano* **2009**, *3*, 2809-2817.

(30) McClure, S. A.; Worfolk, B. J.; Rider, D. A.; Tucker, R. T.; Fordyce, J. A. M.; Fleischauer, M. D.; Harris, K. D.; Brett, M. J.; Buriak, J. M. *ACS Applied Materials & Interfaces* **2010**, *2*, 219-229.

(31) Mizuno, H.; Buriak, J. M. *ACS Applied Materials & Interfaces* **2009**, *1*, 2711-2720.

(32) Krause, K. M.; Taschuk, M. T.; Harris, K. D.; Rider, D. A.; Wakefield, N. G.; Sit, J. C.; Buriak, J. M.; Thommes, M.; Brett, M. J. *Langmuir* **2010**, *26*, 4368-4376.

(33) Brett, M. J.; Hawkeye, M. M. *Science* **2008**, *319*, 1192-1193.

(34) Hawkeye, M. M.; Brett, M. J. *Journal of Vacuum Science & Technology A* **2007**, *25*, 1317-1335.

(35) Teki, R.; Parker, T. C.; Li, H. F.; Koratkar, N.; Lu, T. M.; Lee, S. *Thin Solid Films* **2008**, *516*, 4993-4996.

(36) Brundle, C. R.; Charles k Evans, J.; Wilson, S. *Encyclopedia of Materials Characterization: Surfaces, Interfaces, Thin Films*; Butxetworch-Heinemann: Stoneham, 1992.

(37) Birkholz, M. *Thin Film Analysis by X-Ray Scattering*; WILEY-VCH Verlag Gmbh & Co. KGaA, Weinheim, 2006.

(38) Van Hest, M.; Leenheer, A. J.; Perkins, J. D.; Teplin, C. W.; Ginley, D. S. In *Conference Record of the 2006 IEEE 4th World Conference on Photovoltaic Energy Conversion, Vols 1 and 2*, 2006, pp 1368-1371.

(39) *Bruker Axs Inc., Bruker Advanced X-Ray Solutions: General Area Detector Diffraction Systems (GAADS)*; GAADS User's Manual: Madison.

(40) Liew, S. L.; Balakrisnan, B.; Ho, C. S.; Thomas, O.; Chi, D. Z. *Journal of the Electrochemical Society* **2007**, *154*, H9-H12.

(41)

(42) Tang, F.; Parker, T.; Wang, G. C.; Lu, T. M. *Journal of Physics D-Applied Physics* **2007**, *40*, R427-R439.

(43) Detavernier, C.; Ozcan, A. S.; Jordan-Sweet, J.; Stach, E. A.; Tersoff, J.; Ross, F. M.; Lavoie, C. *Nature* **2003**, *426*, 641-645.

(44) Filoti, D. I.; Brown, A. M.; Carlson, D.; Harper, J. M. E. *Journal of Vacuum Science & Technology B* **2009**, *27*, 585-589.

(45) Tachibana, T.; Yokota, Y.; Kobashi, K.; Shintani, Y. *Journal of Applied Physics* **1997**, *82*, 4327-4330.

(46) Limmer, S. J.; Kulp, E. A.; Switzer, J. A. *Langmuir* **2006**, *22*, 10535-10539.

(47) Park, K. H.; Smith, G. A.; Rajan, K.; Wang, G. C. *Metallurgical Transactions A-Physical Metallurgy and Materials Science* **1990**, *21*, 2323-2332.

(48) Jiang, H.; Klemmer, T. J.; Barnard, J. A.; Doyle, W. D.; Payzant, E. A. *Thin Solid Films* **1998**, *315*, 13-16.

(49) Herman, M. A., Richter, W. & Sitter, H. *Epitaxy; Physical Principles and Technical Implementation*; Springer 2004.

(50) Yokota, Y.; Hashimoto, H.; Saito, N.; Endoh, H. *Japanese Journal of Applied Physics Part 2-Letters* **1986**, *25*, L168-L170.

(51) Li, B. Q.; Zuo, J. M. *Surface Science* **2002**, *520*, 7-17.

Chapter 5

Conclusions

This chapter summarizes the results and achievements, observed from each case studied in each chapter, and addresses some future work directions.

5.1. Summary

This thesis was dedicated to the synthesis and interfacial characterization of nanoscale metal-semiconductor contacts. An efficient and versatile approach for the synthesis of metallic nanostructures on a variety of semiconductor surfaces, including GaAs, InP, silicon [Si(111), Si(100) and Si nanowires], and germanium is galvanic displacement – a spontaneous electrochemical reaction that is a member of the electroless deposition family. In this class of reactions, sufficiently oxidizing metal ions, with a redox potential more positive than that of the substrate, are reduced by electrons derived from the bonding electrons of the substrate lattice valence band; the reaction is accompanied by substrate dissolution and occurs in the absence of an external source of electric current or chemical reducing agents. The result is metallic nanoparticles and films interfaced directly with the substrate surface.

Interfacial characterization was performed to identify the nature and composition of the metal-semiconductor interface. X-ray photoelectron spectroscopy (XPS) depth profile analysis was used to analyse and identify the chemical species that exist between the deposited metal and the underlying semiconductor surface. In the case of the Au/GaAs and Au/InP systems, we discovered a multilayer structure with more Ga and In rich gold intermetallic alloys at the interface with GaAs and InP, respectively, topped by a more gold rich intermetallic, which is covered by the deposited metallic gold. The existence of intermetallics at the interfaces was also established for other systems such as Au/Si(111), Au/Si(100), and Au/Si nanowires (NWs) based on nanobeam (20 nm) diffraction analyses using transmission electron microscopy (TEM). As a result of the intermetallic nature of metal-semiconductor contacts prepared by galvanic displacement, these systems can allow the conduction of current, opening the door for further electronic applications.

The room temperature galvanic displacement of gold on silicon surfaces (Si(111), Si (110) and Si NWs) resulted in heteroepitaxial growth of single crystalline gold with 0.2% lattice mismatch as a result of matching the spacing of four gold atoms with three silicon atoms. These results were proven by high resolution TEM and selected area electron diffraction analyses. In the case of Au/Ge, we were also able to tune the texture nature of the gold overlayer by changing the composition of the deposition bath. Pole figure and θ-2θ X-ray diffraction analyses showed that fiber texture and epitaxial gold layers were grown on Ge surfaces using gold salt solution in the absence and in the presence of hydrofluoric acid, respectively.

During galvanic displacement of gold on silicon nanowires, which extend from the substrate along the <112> growth direction, Au nanoparticles showed preferential deposition on Si(110) faces rather than on the Si(111) faces. This phenomenon was attributed to the high surface energy of the Si(110) faces compared to that of the Si(111) faces. Moreover, we were able to answer a fundamental question: does metal diffuse into to the substrate, do substrate atoms diffuse into the gold, or do both processes occur simultaneously? Scanning Auger electron spectroscopy suggests little diffusion of the metals into the semiconductor lattice.

5.2. Proposed Research Directions

These studies complement our studies in understanding the nature of metal-semiconductor contacts prepared by galvanic displacement.

5.2.1. Comparative Current-Voltage Investigations for Gold-Silicon Contacts Prepared by Galvanic Displacement and Evaporation Procedures

Gold-silicon contacts are of great interest in current research studies as a result of their versatile use in various synthetic processes such as the growth of semiconductor nanowires,[1, 2] the formation of Schottky diodes,[3, 4] the integration of microelectromechanical systems,[5] and others.[6] This thesis has described a detailed characterization of the Au-Si contacts prepared *via* galvanic displacement. Interfacial analyses have shown the room temperature formation of gold-silicon intermetallics, and heteroepitaxy. On the contrary, evaporated and sputtered films require annealing at higher temperatures, under ultra high vacuum conditions, to achieve the epitaxial alignment of gold on silicon.[7] Hence, it is imperative to investigate the difference between gold films prepared by chemical (galvanic displacement) and physical (sputtering or evaporation) methods in regards to the electrical properties of these contacts. Scanning tunneling microscopy (STM) can provide the required direct electrical information without encountering the tip convolution problems encountered by the conductive atomic force microscopy when scanning in a contact mode.

With regards to the preparation of Au-Si samples for STM studies, one of the possible routes is to have a silicon sample patterned with two gold areas. One gold area is prepared by galvanic displacement, while the second area is prepared by evaporation of gold, so that both areas can be tested under the same conditions. The proposed sample can be prepared through photolithographic procedures shown in Figure 5.1. Firstly, we will pattern an area of 1 cm^2 of H-Si with thin gold deposits by galvanic displacement procedures. Secondly, on the same wafer but on a different H-Si area, we will evaporate gold. Finally, through using STM, the difference in the electrical properties of gold deposits grown by evaporation and by galvanic displacement methods would be investigated.

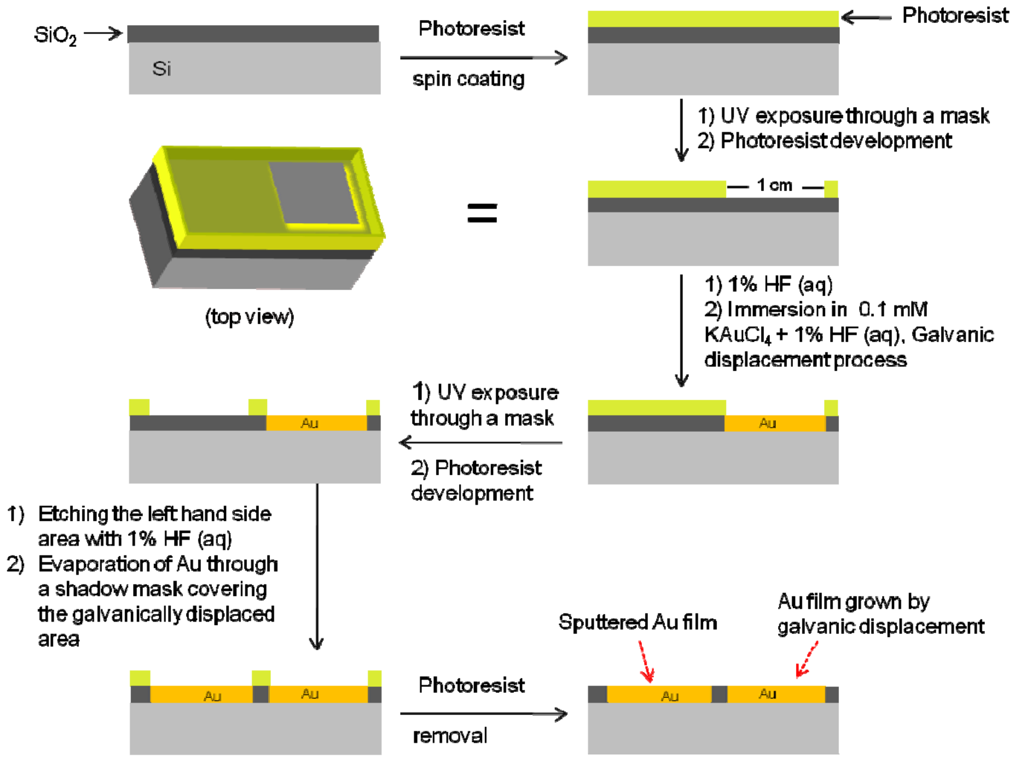

Figure 5.1. *Schematic diagram showing the synthetic procedures for the preparation of a Au-Si sample with two gold areas – one of which is prepared by galvanic displacement, while the other is prepared by evaporation of gold.*

5.2.2. Gold – Germanium Interface and Alloy Formation

In chapter 4, we studied the growth of a gold layer by galvanic displacement on germanium surfaces. The detailed analyses showed the formation of gold films of different textures depending on the HF concentrations. For example, in the presence of high HF content (20%), epitaxial gold film of direct contact with the underlying germanium substrate was observed. Cross-sectional TEM investigation, involving nanobeam (~5 nm probe size) diffraction analyses did not show any evidence for intermetallic formation. To the best of our knowledge, with the lack of information such as the binding energies of different gold-germanium alloys and their crystallographic properties,[8] one study has referred to the possible existence of such interfacial intermetallics for an Au-Ge sample prepared by galvanic displacement.[9] Carraro *et al*. have studied the X-ray photoemission spectra of the valence band region of Au films formed at increasing immersion times in a gold salt solution, as shown in Figure 5.2. The evidence for germanide formation was substantiated from the deconvolution of the experimental gold peak into metallic peak and an unknown peak of binding energy higher than that of metallic gold by 0.5 eV.

In the case of gold on silicon (Chapter 3), we surmised that the interface is most likely composed of regions of heteroepitaxial gold-on-silicon, and separate domains containing an intermetallic sandwiched between the gold and silicon layers. Taking into consideration the 5 nm investigated area for the cross-sectional TEM image shown in chapter 4 for Au-on-Ge, one possibility is that the investigated area is the heteroepitaxial region. Hence, detailed TEM investigations for several Au-Ge cross-sectional samples, prepared under various conditions such as HF content in the reaction mixture, are required. Moreover, annealing at higher temperature is one of the important factors that would need to be considered in this study.

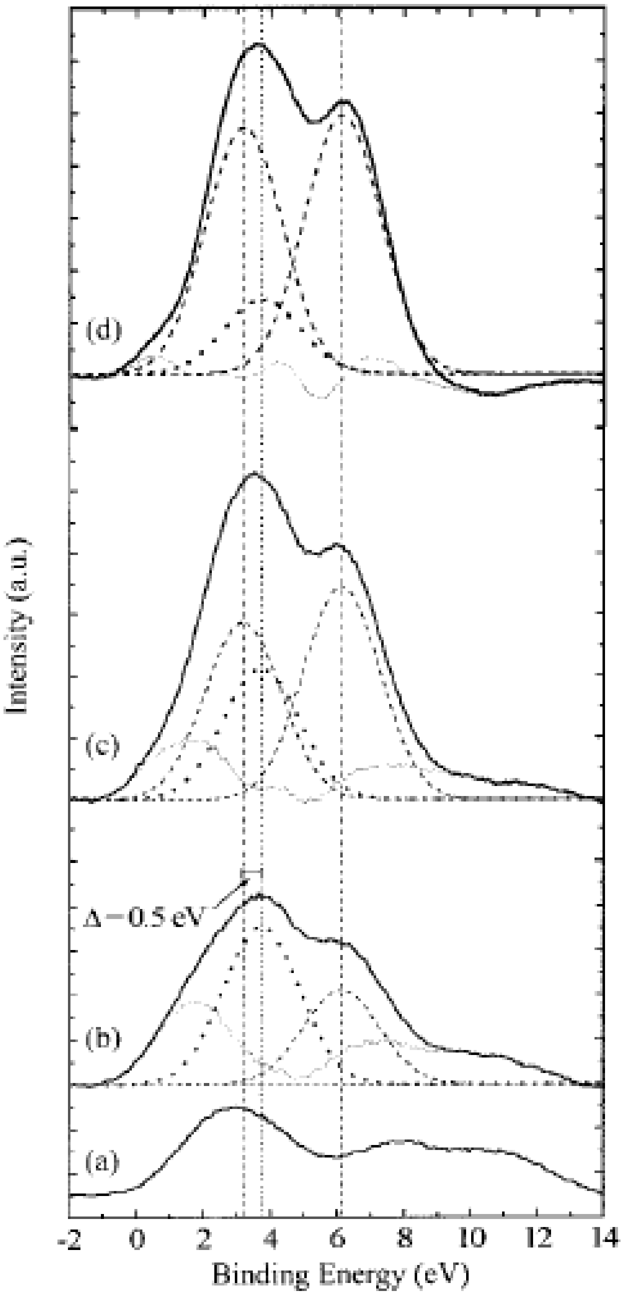

Figure 5.2. *X-ray photoemission spectra of the valence band region of Au formed on a Ge surface after 0 s (a) 5 s (b), 60 s (c), and 600 s (d). Thick solid line: data. Copyright (c) 2002 American Chemical Society. Reproduced with permission from ref.*[9]

5.2.3. Epitaxial Growth of Semiconductor Nanowires Catalyzed by Galvanically Displaced Gold on Germanium Surfaces

During the past decade, semiconductor nanowires (NWs) have been used in a wide range of novel devices having applications in optoelectronics, nanoelectronics, and sensors.[10-17] Different semiconductor nanowires have been synthesized, with the greatest focus on Si and Ge NWs. Vapor-liquid-solid synthesis (VLS) is one of the most commonly used growth mechanisms for growing semiconductor nanowires on semiconductor substrates of different composition.[18] In VLS, metallic nanocrystals catalyze the growth of semiconductor nanowires under high temperature conditions with controlled flow of the semiconductor gaseous precursors.[18]

Recently, it has been observed that intimate contact between the metal catalyst and the underlying substrate is essential to achieve epitaxial semiconductor nanowires with a defect free substrate-nanowire interface.[1, 2] There are several methods for interfacing metal catalysts with semiconductor substrates, including galvanic displacement. In the case of silicon, galvanic displacement (GD) resulted in interfacing silicon substrates with epitaxial gold deposits,[19, 20] leading to a subsequent growth of epitaxial semiconductor nanowires.[1, 2] The key point was the rule of HF in the reaction mixture used for the growth of the gold deposits on the silicon substrates. HF ensures the direct contact of the gold deposit with the underlying substrate as a result of the etching of the silicon oxide layer formed during galvanic displacement process. In chapter four, we highlighted the importance of HF in the synthesis of gold deposits of direct contact (epitaxial interface) with the underlying germanium substrate. Hence, it will be a great opportunity to replace the evaporation and sputtering methods used for the deposition of gold catalyst on germanium substrates with an inexpensive method such as galvanic displacement. We did a preliminary trial to grow silicon nanowires from gold nanocrystals grown by galvanic displacement on a germanium substrate by using VLS technique as shown in Figure 5.3. However, more effort is required for controlling the length of the observed nanowires to be characterized for their epitaxial nature by surface techniques such as X-ray diffraction.

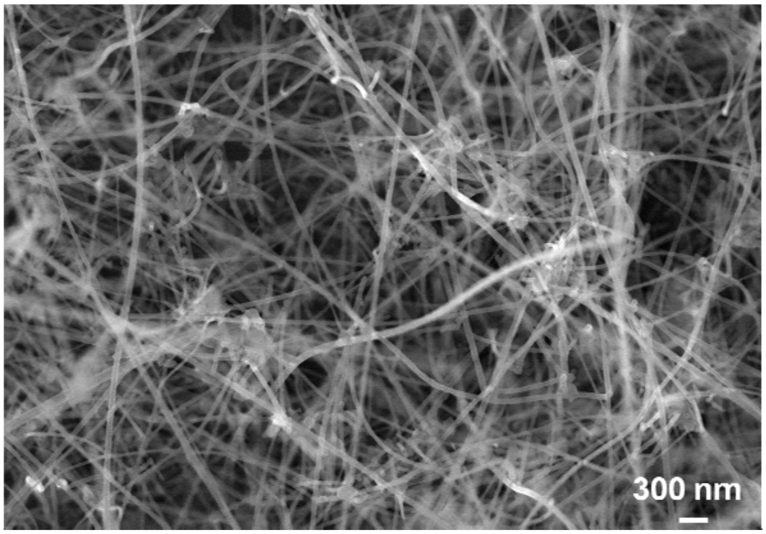

Figure 5.3. *SEM micrograph for silicon nanowires grown by VLS on a Ge(111) substrate. The gold catalyst used in the synthetic process was deposited on the germanium substrate via the immersion of a Ge shard in a solution containing 0.1 mM* $KAuCl_4$ *(aq) and 20% HF (aq) for 2 min. The nanowires were grown for 10 min at 525* ^oC *and 100 torr from a silane (*SiH_4*) gas.*

5.2.4. Heteroepitaxial Formation of Gold Films on GaAs Substrates

Galvanic displacement has been used for interfacing gold films with germanium and gallium arsenide substrates.[21-25] For the most part, deposition solutions only contained a gold salt solution. Taking into account the investigations done in Chapter 4 for the effect of adding HF to metal salt solutions on the texture of gold films on germanium substrates and the slight water solubility[26] of Ga_2O_3 and As_2O_3 (solubility of $As_2O_3>Ga_2O_3$),[27, 28] one can imagine a similar scenario for the growth of epitaxial gold films on GaAs from H-containing solutions. This kind of investigation will require characterization of the texture of the grown gold films on GaAs substrates in the presence of different concentrations of HF (aq) by using both in- and out-of-plane XRD surface analysis methods.

5.3. References

(1) Shimizu, T.; Xie, T.; Nishikawa, J.; Shingubara, S.; Senz, S.; Gosele, U. *Advanced Materials* **2007**, *19*, 917-920.

(2) Shimizu, T.; Senz, S.; Shingubara, S.; Gosele, U. *Applied Physics A-Materials Science & Processing* **2007**, *87*, 607-610.

(3) Oskam, G.; van Heerden, D.; Searson, P. C. *Applied Physics Letters* **1998**, *73*, 3241-3243.

(4) Shiue, J.; Kuo, P. C. *Scripta Materialia* **2010**, *62*, 82-84.

(5) Fujita, T.; Nakamichi, S.; Ioku, S.; Maenaka, K.; Takayama, Y. In *MEMS 2006: 19th IEEE International Conference on Micro Electro Mechanical Systems, Technical Digest*, 2006, pp 290-293.

(6) Miyake, H.; Ye, S.; Osawa, M. *Electrochemistry Communications* **2002**, *4*, 973-977.

(7) Yokota, Y.; Hashimoto, H.; Saito, N.; Endoh, H. *Japanese Journal of Applied Physics Part 2-Letters* **1986**, *25*, L168-L170.

(8) http://srdata.nist.gov/xps/ElmComposition.aspx.

(9) Magagnin, L.; Maboudian, R.; Carraro, C. *Journal of Physical Chemistry B* **2002**, *106*, 401-407.

(10) Haraguchi, K.; Katsuyama, T.; Hiruma, K.; Ogawa, K. *Applied Physics Letters* **1992**, *60*, 745-747.

(11) Duan, X. F.; Huang, Y.; Cui, Y.; Wang, J. F.; Lieber, C. M. *Nature* **2001**, *409*, 66-69.

(12) Cui, Y.; Lieber, C. M. *Science* **2001**, *291*, 851-853.

(13) Huang, Y.; Duan, X. F.; Cui, Y.; Lauhon, L. J.; Kim, K. H.; Lieber, C. M. *Science* **2001**, *294*, 1313-1317.

(14) Wang, J. F.; Gudiksen, M. S.; Duan, X. F.; Cui, Y.; Lieber, C. M. *Science* **2001**, *293*, 1455-1457.

(15) Bjork, M. T.; Ohlsson, B. J.; Thelander, C.; Persson, A. I.; Deppert, K.; Wallenberg, L. R.; Samuelson, L. *Applied Physics Letters* **2002**, *81*, 4458-4460.

(16) De Franceschi, S.; van Dam, J. A.; Bakkers, E.; Feiner, L. F.; Gurevich, L.; Kouwenhoven, L. P. *Applied Physics Letters* **2003**, *83*, 344-346.

(17) Islam, M. S.; Sharma, S.; Kamins, T. I.; Williams, R. S. *Nanotechnology* **2004**, *15*, L5-L8.

(18) McIntyre, P. C.; Adhikari, H.; Goldthorpe, I. A.; Hu, S.; Leu, P. W.; Marshall, A. F.; Chidsey, C. E. D. *Semiconductor Science and Technology* **2010**, *25*.

(19) Sayed, S. Y.; Wang, F.; Mallac, M.; Meldrum, A.; Egerton, R. F.; Buriak, J. M. *ACS Nano* **2009**, *3*, 2809-2817.

(20) Warren, S.; Reitzle, A.; Kazimirov, A.; Ziegler, J. C.; Bunk, O.; Cao, L. X.; Renner, F. U.; Kolb, D. M.; Bedzyk, M. J.; Zegenhagen, J. *Surface Science* **2002**, *496*, 287-298.

(21) Porter, L. A.; Choi, H. C.; Schmeltzer, J. M.; Ribbe, A. E.; Elliott, L. C. C.; Buriak, J. M. *Nano Letters* **2002**, *2*, 1369-1372.

(22) Porter, L. A.; Choi, H. C.; Ribbe, A. E.; Buriak, J. M. *Nano Letters* **2002**, *2*, 1067-1071.

(23) Aizawa, M.; Cooper, A. M.; Malac, M.; Buriak, J. M. *Nano Letters* **2005**, *5*, 815-819.

(24) Nezhad, M. R. H.; Aizawa, M.; Porter, L. A.; Ribbe, A. E.; Buriak, J. M. *Small* **2005**, *1*, 1076-1081.

(25) Sayed, S. Y.; Daly, B.; Buriak, J. M. *Journal of Physical Chemistry C* **2008**, *112*, 12291-12298.

(26) Hou, T.; Greenlief, M.; Keller, S. W.; Nelen, L.; Kauffman, J. F. *Chemistry of Materials* **1997**, *9*, 3181-3186.

(27) Kirchner, C.; George, M.; Stein, B.; Parak, W. J.; Gaub, H. E.; Seitz, M. *Advanced Functional Materials* **2002**, *12*, 266-276.

(28) Traub, M. C.; Biteen, J. S.; Brunschwig, B. S.; Lewis, N. S. *Journal of the American Chemical Society* **2008**, *130*, 955-964.